

An Engineered Approach to Specialty Chemicals Purification

A DISSERTATION
SUBMITTED TO THE FACULTY OF
UNIVERSITY OF MINNESOTA
BY

Nathan T. Morgan

IN PARTIAL FULFILLMENT OF THE REQUIREMENTS
FOR THE DEGREE OF
DOCTOR OF PHILOSOPHY

Russell J. Holmes and E. L. Cussler, Advisers

August 2016

© Nathan T. Morgan 2016

Acknowledgements

First, I would like to acknowledge my advisers, Russell Holmes and Ed Cussler, who provided the opportunity, encouragement, and support that made this work possible. I would also like to thank the members of the Holmes research group, past and present, for their thoughtful discussion and technical support. Finally, I would like to thank the CEMS community, especially the 2011 graduate class, for their continual moral support, without which I surely would not have made it this far.

Funding was provided by the L.E. and D.H. Scriven Fellowship and The Dow Chemical Company under Dow Agreement Number 224249AR, Enhanced Methods for Specialty Chemicals Purification. RJH is a member of The Dow Chemical Company Technical Advisory Board.

Dedication

To my family, who got me here
And to my wife, who got me through

Abstract

High purity is a near-universal requirement throughout the specialty chemicals industry, essential for many of the applications we take for granted in our daily life. The purification process is often a significant portion of the manufacturing cost for many specialty chemicals, including organic semiconductors and pharmaceuticals. Reducing this manufacturing cost is a key step in the effort to efficiently produce the necessary materials for our modern world.

This dissertation examines two key purification processes, thermal gradient sublimation and crystallization, in order to offer potential routes for process improvement. Thermal gradient sublimation is examined through the lens of organic semiconductors, which are often purified using this technique at the industrial scale. Interestingly, the sublimation process is limited by vapor phase transport and deposition, not solid phase mechanisms. A model for this process is developed, suggesting potential routes to efficient scale-up and separation improvements.

This dissertation also proposes a new method for crystallization control, pressure-swing. In this approach, rapid changes in pressure are used to control solubility during the crystallization process. A model describing the changes in solubility due to these pressure changes is developed, and several process validation experiments are performed using pharmaceutical molecules as model systems. While these tests show an enhanced control of solubility, attempts to replicate experimental results obtained using traditional crystallization control are only partially successful when using the pressure-swing technique.

Table of Contents

List of Tables	vii
List of Figures	viii
1. An Introduction to Specialty Chemicals Purification	1
1.1. Markets for Specialty Chemicals	1
1.1.1. Organic Semiconductors	2
1.1.2. Pharmaceuticals	4
1.2. Purity Requirements for Specialty Chemicals	4
1.3. Common Purification Techniques	5
1.3.1. Distillation	5
1.3.2. Extraction	6
1.3.3. Crystallization	7
1.3.4. Sublimation	11
1.4. Common Purification Challenges	12
2. Instrumentation and Methods	14
2.1. Thermal Gradient Sublimation	14
2.1.1. Equipment Design	14
2.1.2. Experimental Methodology	16
2.2. High Pressure Crystallization	17
2.2.1. Equipment Design	18
2.2.2. Experimental Methodology	20
2.3. Analytical Techniques	22
2.3.1. Optical Microscopy	22
2.3.2. Melting Point	24
2.3.3. Differential Scanning Calorimetry	25
2.3.4. High Performance Liquid Chromatography	26
2.3.5. X-Ray Diffraction	27
2.3.6. Liquid Density Measurements	28
2.3.7. Vapor Pressure Measurements	29
3. Rate-Limiting Steps in Thermal Gradient Sublimation	32
3.1. Potential Rate-Limiting Steps	33
3.1.1. Diffusion within Solid Particles	34
3.1.2. Diffusion within a Composite Solid or Ash	34
3.1.3. Surface Desorption	35
3.1.4. Diffusion Away from the Particle Surface	36
3.1.5. Mass Transfer Away from the Sample Boat	36

3.1.6. Mass Transfer from the Boat to the Collection Zone	37
3.2. Experimental Determination of Rate-Limiting Mechanisms.....	38
3.2.1. Sublimation Rate as a Function of Time	39
3.2.2. Sublimation Rate as a Function of Particle Size.....	40
3.2.3. Sublimation Rate as a Function of Initial Loading	41
3.2.4. Sublimation Rate as a Function of Boat Area.....	42
3.2.5. Sublimation Rate as a Function of Transport Length.....	43
3.2.6. Sublimation Rate as a Function of Tube Diameter.....	45
3.3. Rate-Limiting Mechanisms in Thermal Gradient Sublimation	45
4. Vapor Phase Transport and Separation in Thermal Gradient Sublimation	47
4.1. Theoretical Mechanisms for Low Pressure Vapor Transport.....	48
4.1.1. Ballistic Transport.....	48
4.1.2. Knudsen Diffusion and Diffusion.....	49
4.1.3. Viscous Flow	51
4.1.4. Slip Flow.....	52
4.2. Experimental Evidence Supporting Diffusion.....	53
4.3. Diffusion-Based Transport and Deposition Model.....	55
4.3.1. Diffusion Theory.....	55
4.3.2. Predicted Deposition Profile.....	59
4.3.3. Sublimation Rate Predictions.....	61
4.4. Separation	63
4.4.1. Fundamental Improvements in Purity.....	63
4.4.2. Impact of Temperature Gradient.....	65
4.5. Scale-Up.....	66
4.5.1. Diffusion Based Scale-Up	67
4.5.2. Alternate Transport Regimes at Elevated Pressure.....	68
4.5.3. Continuous Processing.....	70
4.6. Model Scope and Conclusions.....	71
5. The Effect of Rapid Pressurization on the Solubility of Small Organic Molecules	72
5.1. Temperature Changes Due to Pressurization.....	72
5.1.1. Experimental Temperature Changes Due to Pressurization	73
5.1.2. Theoretical Temperature Changes Due to Pressurization.....	74
5.2. Determination of Solubility at Elevated Pressure.....	76
5.2.1. Experimental Measurement of Solubility at Elevated Pressure.....	76
5.2.2. Theoretical Rationale	78
5.3. The Effect of Rapid Pressurization on Solubility	80
5.4. Conclusions.....	81
6. Applications for Pressure-Swing Crystallization.....	83

6.1. Advantages of Pressure-Swing Crystallization.....	83
6.2. Nucleation Control.....	84
6.3. Polymorph Generation.....	87
6.3.1. Nucleation at High Static Pressure	87
6.3.2. Nucleation at High Induced Supersaturation	88
6.3.2.1. Supersaturation Control using Temperature	89
6.3.2.2. Supersaturation Control using Pressure-Swing	90
6.4. Purification via Crystal Digestion.....	92
6.4.1. Digestion using Temperature Control.....	92
6.4.2. Digestion using Pressure-Swing	96
6.5. Conclusions.....	98
7. Conclusions and Future Research.....	100
7.1. Thermal Gradient Sublimation	100
7.1.1. Sublimation Research Summary.....	100
7.1.2. Impact of Material Bonding on Rate-Limiting Step.....	101
7.1.3. Impact of Elevated Temperature on Sublimation	102
7.1.4. Trade-off between High Temperature and Degradation.....	103
7.1.5. Detailed Transport Mechanism.....	104
7.2. Crystallization.....	106
7.2.1. Research Summary	106
7.2.2. Digestion Using Pressure-Swing Crystallization.....	108
7.2.3. Alternative Model Systems.....	109
7.3. Conclusions.....	110
8. References.....	111
9. Appendices.....	119
A. NPD Synthesis Details	119
B. Control Software for Pressure Crystallization System.....	122
C. Mass Spectrometry Data for NPD Impurities	140
D. Transport Velocity Simulation Code	142
E. List of Publications.....	147
F. List of Presentations	148
G. List of Patents.....	149
H. Copyright Permissions	150

List of Tables

Table 3.1: Key area and flux associated with each potential rate-limiting step for thermal gradient sublimation.....	38
Table 4.1: Geometric dependences of potential rate-limiting vapor transport mechanisms..	53
Table 4.2: Experimental and predicted values for the slope and intercept in Equation 4.18. The slope gives an indication of the impact of transport down the tube on sublimation rate. The intercept gives an indication of the impact of deposition.	62
Table 4.3: Purity of NPD before and after sublimation without a controlled temperature gradient. High purity was achieved even for impure starting material.....	65
Table 5.1: Thermodynamic quantities used for Equation 5.1.....	75
Table 5.2: Predicted values for the change in solubility with pressure from Equation 5.3 compared to experimental values obtained from nucleation temperature as shown in Figure 5.2b.	80
Table 6.1: The additional supersaturation generated using the pressure-swing technique is not large enough to induce nucleation of the metastable polymorph for piracetam or paracetamol.	91

List of Figures

Figure 1.1: Distinctions between different chemical businesses. Adapted from Ref. 1.	2
Figure 1.2: Schematic of a typical distillation column.	6
Figure 1.3: Schematic of a typical liquid-liquid extraction process.	7
Figure 1.4: Solubility profile during a typical cooling crystallization.	8
Figure 1.5: Adipic acid melting point decreases as cooling rate increases, indicating a decrease in crystal purity as a function of cooling rate.	10
Figure 1.6: Schematic of a typical cold finger sublimation purification process.	11
Figure 2.1: Schematic of typical thermal gradient sublimation system.	15
Figure 2.2: Photo of a typical collection tube after the thermal gradient sublimation of NPD.	15
Figure 2.3: (a) NPD Molecular Structure. (b) TCTA Molecular Structure.	17
Figure 2.4: Schematic of pressure-swing crystallization system.	19
Figure 2.5: Photographs of the (a) interior and (b) exterior of the pressure-swing crystallization system.	20
Figure 2.6: (Graph) Characteristic increase in temperature due to nucleation for piracetam in ethanol. (Inset) Piracetam molecular structure.	21
Figure 2.7: Schematic of traditional polarized light microscopy.	23
Figure 2.8: (a) Adipic acid DSC curve with melting point and heat of fusion. (b) Purity analysis of adipic acid DSC curve. The fraction melted is plotted as a function of temperature and fit according to Equation 2.3.	26
Figure 2.9: Comparison between the XRD spectra of two different polymorphs of piracetam.	28
Figure 2.10: Vapor pressure as a function of temperature for (a) NPD and (b) TCTA.	30
Figure 3.1: Potential rate-limiting steps for thermal gradient sublimation. Mechanisms 1-4 occur in the solid phase, mechanism 5 is mass transfer away from the sample boat, and mechanism 6 is vapor phase transport and deposition within the tube.	33

Figure 3.2: Temperature profile during a typical sublimation experiment involving NPD...	39
Figure 3.3: Mass sublimed is linear as a function of time. Sublimation rate does not change as a function of time.	40
Figure 3.4: (a) Pressed pellets of NPD powder before sublimation. (b) Pellets after six hours of sublimation.	41
Figure 3.5: Mass sublimed is constant as a function of initial loading.	42
Figure 3.6: Mass sublimed divided by boat surface area is not constant. Mass sublimed is not linear as a function of boat surface area.	42
Figure 3.7: NPD sublimation rate decreases as the distance to the collection zone or the transport length increases.	43
Figure 3.8: The sublimation rate is inversely proportional to the transport length for both NPD and TCTA, suggesting that vapor transport is limiting. The non-zero intercept is attributed to vapor deposition, as discussed in Chapter 4.	44
Figure 3.9: The sublimation rate is proportional to the tube diameter squared for both NPD and TCTA.	45
Figure 4.1: Schematic of a vapor transport and deposition limited thermal gradient sublimation process.	47
Figure 4.2: Dependence of sublimation rate on tube diameter. (a) The sublimation rate is proportional to d^2 for both NPD and TCTA, indicating that the dominant transport mechanism is diffusion. (b) The same data shown on a logarithmic scale.	54
Figure 4.3: The sublimation rate is inversely proportional to the transport length for both NPD and TCTA, consistent with diffusion or flow. The non-zero intercept is attributed to vapor deposition.	54
Figure 4.4: (a) The NPD deposition rate exponentially decays as a function of deposition length for a variety of process conditions. Note the different scale for 290 °C deposition. The onset is not perfectly sharp because the mass was measured in 1 cm increments. (b) The normalized mass of NPD deposited shows the same exponential decay for the variety of experimental conditions.	59

Figure 4.5: Dependence of the inverse transport velocity on transport length, allowing the separation of resistances due to transport and deposition. As the transport length approaches zero, the vertical-intercept results from resistance due to deposition. The non-zero intercept and positive slope show that both transport and deposition are important in the sublimation process.	61
Figure 4.6: (a) Molecular structure for NPD and (b, c) Primary impurities.	64
Figure 4.7: (a) Temperature profiles for the purification of NPD-TCTA mixtures. (b) NPD and TCTA deposition profile for a relatively steep temperature profile (1). Both compounds show an exponential decay, but significant overlap was present. (c) NPD and TCTA deposition profile for a relatively shallow temperature profile (2). Two clear exponential decays are present and significant amounts of each pure component were recovered.	66
Figure 4.8: Transport velocity calculated as a function of pressure within the sublimation system for TCTA. At low pressure the transport is dominated by Knudsen diffusion and the velocity is independent of pressure. At high pressure the transport is dominated by flow and the velocity is proportional to pressure. At moderate pressure the transport is dominated by intermolecular diffusion and the velocity is inversely proportional to pressure.	69
Figure 5.1: (a) Change in temperature as a function of pressure for methanol. The change in temperature is nonlinear due to heat transfer and changes in material properties with increased pressure. (b) The experimental increase in temperature upon compression to 10,000 psig compared to predictions from Equation 5.1 for a variety of solvents. Equation 5.1 overestimates the temperature due to heat transfer and varying material properties.	74
Figure 5.2: (a) The nucleation temperature increases as a function of pressure and mole fraction X for paracetamol in water. (b) Solubility decrease with pressure for paracetamol in water plotted according to Equation 5.3.	78
Figure 5.3: (a) Predicted decrease in solubility upon pressurization for paracetamol in water. (b) Predicted increase in solubility upon pressurization for piracetam in ethanol.	81
Figure 6.1: (a) Nucleation of piracetam in ethanol after slowly cooling in the pressure crystallizer. Inset shows piracetam molecular structure. (b) Nucleation of piracetam after a rapid drop in pressure.	85
Figure 6.2: (a) Rapidly cooling piracetam induces nucleation at high supersaturation, yielding metastable Form II. (b) Slowly cooling piracetam induces nucleation at low supersaturation, yielding stable Form III.	89

Figure 6.3: (a) Metacetamol is incorporated into paracetamol as an impurity. Two crystal phases exist below 85 wt. %. (b) Paracetamol molecular structure. (c) Metacetamol molecular structure.....	93
Figure 6.4: (a) Temperature profile during typical digestion experiment. (b) Solubility and crystal mass predicted from solubility, ignoring growth kinetics.	94
Figure 6.5: (a) Digestion experiments conducted on the benchtop show that digested crystals are more pure than undigested crystals. The run to run variation is due to fluctuations in the cooling rate. (b) Results from a similar experiment conducted in the pressure crystallization system using similar temperature control also show an increase in purity.	95
Figure 6.6: (a) Temperature and pressure profile for a typical pressure-swing digestion experiment. (b) Solubility and crystal mass predicted from solubility of pure paracetamol, ignoring growth kinetics.....	96
Figure 6.7: Purity does not noticeably increase for pressure-swing digestion.	97
Figure 6.8: (a) Temperature and pressure profiles for pressure-swing experiments as a function of the starting temperature for the pressure-swing, effectively varying the percentage of crystal mass dissolved during the digestion step. (b) Purity of digested crystals is not a function of the percentage of crystal mass digested. When the pressure-swing was initiated at 33°C, the crystals were completely dissolved during the digestion step.	98
Figure 7.1: (a) TCTA sublimation rate increases exponentially with pressure. (b) TCTA sublimation rate appears to increase linearly with vapor pressure, but analysis is limited due to limited vapor pressure resolution.	102

1. An Introduction to Specialty Chemicals

Purification

At a very fundamental level, almost everything that we encounter on a daily basis can be labeled as a chemical. From plastics to gasoline to pharmaceuticals, chemicals are an inherent part of our daily lives. The majority of commodity chemicals, like plastics or acetic acid, are manufactured on a large scale with production exceeding thousands or millions of tons per year. This large scale and production capacity naturally leads to a large degree of process optimization and cost savings. In contrast to this, the fine and specialty chemicals markets operate on a much smaller scale and produce more expensive, specialized products. While some of this cost increase can be simply attributed to the scale of production, a significant portion of the cost increase is due to the difficulty of manufacturing specialized products with stringent specifications. This dissertation will focus on an important single step of the production process: purification.

1.1. Markets for Specialty Chemicals

The definition of a specialty chemical varies throughout the industry, but a generally agreed upon requirement is that a specialty chemical must be sold based on its performance, not its molecular structure.¹ A classic example of this is paracetamol, produced not for its chemical structure, but due to its ability to cure headaches associated with excessive alcohol consumption. This distinction is more clearly illustrated in Figure 1.1. In general, this means that a wide range of products fall under the umbrella of

specialty chemicals. This includes additives, biocides, electronic chemicals, flavors, fragrances, household and personal care products, pharmaceuticals, specialty polymers, and agrochemicals. Altogether,

Commodities	Specialty Chemicals	Fine Chemicals
single pure chemical	mixtures or pure chemical	single pure chemical
produced in dedicated plants	formulated	produced in multi-purpose plants
high volume / low cost	low volume / high cost	low volume / high cost
many applications	few applications	few applications
sold on molecular structure	sold on performance	sold on molecular structure

Figure 1.1: Distinctions between different chemical businesses. Adapted from Ref. 1.

specialty chemicals account for approximately half of the global chemical market or \$800 billion/yr at the start of this project in 2011.² Of this, the largest market shares are the agrochemical and pharmaceutical industries.

The sheer scale and diversity of this product portfolio provide a variety of interesting technical challenges. Of these, purification of the final chemical product is one of the more expensive steps in the production process. While this is often true throughout the chemical industry, it is especially true in the fine and specialty chemicals markets where process optimization is often limited due to the wide array of products. This dissertation will explore purification through the lens of two model systems, organic semiconductors and pharmaceuticals, in order to offer some insight for future process design.

1.1.1 Organic Semiconductors

Organic semiconductors are, as their name implies, organic compounds that possess semiconducting properties. This usually arises due to a chemical bonding

scheme of alternating single and double bonds known as conjugation. Conjugated molecules may have overlapping π -bonds, resulting in an array of available molecular energy levels.³ Electronic transport may occur within these energy levels analogous to transport in traditional semiconductors.⁴

Organic semiconductors have several key advantages when compared to traditional semiconductors, most notably that the electronic properties can be tuned by adjusting the chemical structure.⁵ In this way, a near-infinite array of electronic configurations can be achieved. Additional advantages include the ability to manufacture electronic devices on flexible substrates,⁶ potential amenability towards low-cost roll-to-roll processing,⁷ and extremely thin active layers (<100 nm).⁸ Organic semiconductors can be integrated into a variety of electronic devices such as field effect transistors,^{3,9,10} solar cells,^{8,11,12} and light-emitting diodes,^{13,14} similar to inorganic semiconductors. Commercially, OLED displays account for the majority of the organic semiconductor market, with significant penetration into the mobile handheld and television display markets.

While organic semiconductors may have a variety of chemical structures, the majority of commercial devices are created with so called “small molecules” which are defined as having molecular weights in the range of <1000 g/mol.^{8,12} These molecules are usually processed by sublimation or evaporation and comprise the majority of the industrial production of organic semiconducting materials. This dissertation will use small molecule organic semiconductors as a model system for the industrial purification of specialty chemicals via sublimation.

1.1.2 Pharmaceuticals

The lifespan of the average human has steadily increased over the last 100 years, partially due to the modern pharmaceutical industry. Pharmaceutically active molecules are some of the most synthetically complex chemicals regularly produced and require many years of research and development before commercial deployment. As such, they are also some of the most expensive specialty chemicals to produce. This is represented by the size of the pharmaceutical market; in 2005 total sales produced over \$600 billion of revenue.¹⁵

Pharmaceutically active molecules have a wide variety of structures, but typically are organic compounds with molecular weights between 100-1000 g/mol.¹⁶ This dissertation will not focus specifically on the production of pharmaceutical molecules, but will instead use them as model systems for purification via crystallization, a common process throughout the specialty chemicals industry.

1.2. Purity Requirements for Specialty Chemicals

Specialty chemicals are defined based on their performance, not molecular structure. When compared to standard commodity or fine chemicals, this means that the specification is not strictly related to the chemical purity. However, in many cases, high purity is a strong indicator of performance or simply a fundamental requirement. For example, in organic semiconductors, the purity of starting materials has been directly linked to both electronic properties¹⁷ and device lifetime.¹⁸ Similarly, high purity is required for pharmaceuticals due to potential toxicity and undesired interactions.¹⁹

While it is clear that purity plays a key role in materials performance, the exact requirements vary dramatically by application. For most specialty chemicals, purity requirements of >99% are common and requirements >99.99% are not uncommon.^{18,19} The focus of this dissertation will be on common purification techniques used to obtain these high purities and possible routes towards process improvement. As such, the lessons learned here not limited only to specialty chemicals, but are also applicable throughout the chemical industry, especially where high value, high purity products are required.

1.3. Common Purification Techniques

There are a variety of techniques available for obtaining high purity materials. This section will summarize a few of the most common techniques and highlight the scenarios where they are most appropriate. Of these techniques, distillation and extraction are well studied and are routine throughout the chemical business; crystallization is routinely practiced at the industrial scale but is not as well understood; and sublimation is practiced in limited cases and is not well understood. For the purpose of this work, crystallization and sublimation will be studied in detail because they provide the most room for improvement and are most appropriate for solid chemical products, such as organic semiconductors and pharmaceuticals.

1.3.1. Distillation

Distillation is perhaps the most common purification technique practiced within the chemical industry today. Distillation is typically used to separate a liquid or vapor mixture by exploiting differences in vapor pressure between the components of interest.

A classic example of this is the enrichment of ethanol in ethanol-water mixtures to produce liquor from beer. Figure 1.2 shows a schematic of this process. In this case a liquid or vapor feed is introduced to the column somewhere in the middle. Liquid flows down the column and equilibrates with rising vapor on each stage. Typically, some of the vapor at the top and some of the liquid at the bottom of the column is recycled using a reboiler and condenser. The separation is controlled by varying the

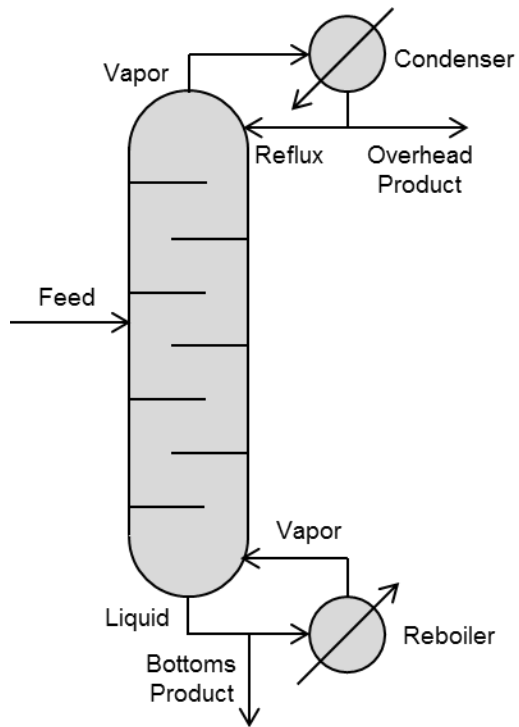


Figure 1.2: Schematic of a typical distillation column.

temperature and flow rate of the feed and recycle streams from the condenser and reboiler. The quality of separation that can be reasonably expected for a given mixture can be estimated from equilibrium data using the traditional McCabe-Thiele approach and is the focus of almost every undergraduate separations course.²⁰

For many specialty chemicals, distillation is not a suitable purification technique because the target product exists as a solid at standard operating conditions. For distillation to be effective, a vapor-liquid equilibrium must be established. Attempts to melt the target material are often unsuccessful and result in unwanted degradation of the product. For this reason, this dissertation will not discuss distillation in detail.

1.3.2. Extraction

Extraction is another common unit operation within the chemical industry used to remove non-volatile components from liquid streams. In extraction operations, two immiscible liquid streams are flown countercurrent to one another in a packed tower. This is illustrated schematically in Figure 1.3. Typically, extraction liquids are chosen such that the target chemical has a large solubility within one liquid phase and any impurities have a large solubility in the other liquid phase. The two liquid phases are allowed to equilibrate within the packed tower, separating the target chemical from the impurities. The product and impurities are later recovered via crystallization or evaporation of the extraction solvents.

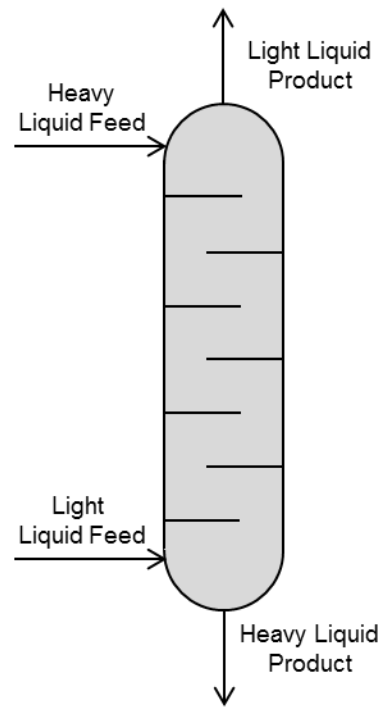


Figure 1.3: Schematic of a typical liquid-liquid extraction process.

This type of separation can be used for specialty chemicals so long as appropriate extraction liquids are available. Often, limited solubility differences exist between the chemical of interest and any potential impurities making effective extraction impossible. As such, extraction is more often used when a non-volatile component must be removed from a liquid stream, such as toxic metal ions from a waste stream.²⁰

1.3.3. Crystallization

Crystallization is the most common purification step used when the product chemical is a solid, like many specialty chemicals. The starting feed for a crystallizer is typically a solution of the target chemical in a liquid

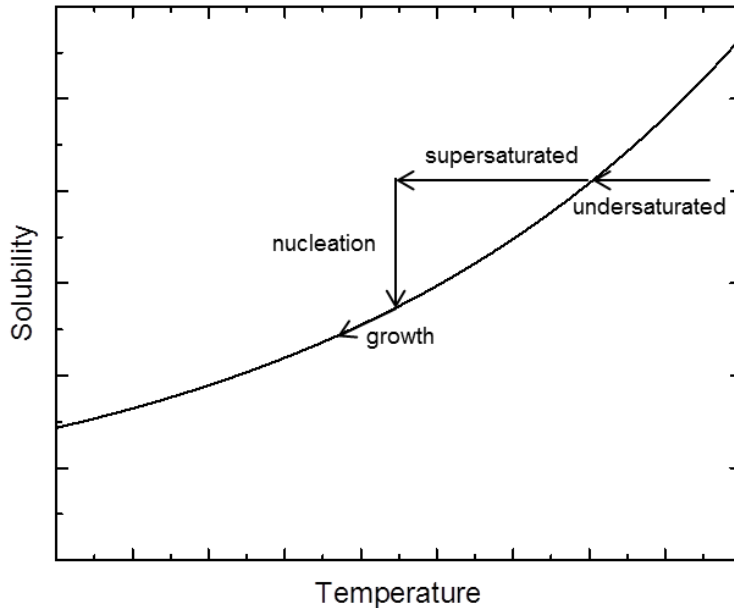


Figure 1.4: Solubility profile during a typical cooling crystallization.

solvent. At its most basic level, crystallization occurs when the amount of the target chemical exceeds its solubility within the solvent. This can occur for a variety of reasons including a change in temperature or pressure, addition of another chemical or “anti-solvent,” or simply an addition of more of the target material via reaction. Once the solubility has been exceeded, the solution becomes thermodynamically unstable and there is a driving force for the solute to leave the solution. This is illustrated schematically in Figure 1.4 for a typical cooling crystallization. This transition from solution typically takes the form of a liquid-solid phase transition, known as nucleation.

Nucleation does not occur immediately after saturation; instead some additional driving force, known as supersaturation, is required to overcome the thermodynamic penalty associated with forming a liquid-solid interface, the interfacial energy γ . This penalty is balanced by the volumetric change in Gibbs free energy ΔG_v associated with

the phase transition. Since this balance contains both a surface and volume energy, it is preferable to form large solid particles with a high volume to surface area ratio. This leads to a well-known stability criteria for the formation of nuclei, where the critical size for is given by

$$r_c = -\frac{2\gamma}{\Delta G_v} \quad (1.1)$$

where r_c is the critical nucleus radius and ΔG_v is a negative value.²¹ If this condition is not met, the nucleus dissolves and the molecules are incorporated into other nuclei. As the supersaturation increases, the driving force or ΔG_v increases and the critical radius decreases. This results in an increased rate of nucleation as a function of supersaturation.

Based on the rate of nucleation, the product solid may range anywhere from many small amorphous particles to a single large crystal. For example, a simple solution of sugar in water forms many small clumps when cooled rapidly, but if left to cool slowly, forms large single crystals often referred to as “rock candy.” In the first case, commonly referred to as precipitation, the phase transition occurs so rapidly that the product molecules do not have time to arrange into a thermodynamically stable form and simply “crash” out of solution. This occurs most frequently during fast chemical reactions or when a solution is cooled extremely rapidly. In the second case, known as crystallization, molecules first arrange into small, ordered nuclei. If the nuclei reach the critical size defined by Equation 1.1, they become thermodynamically stable and begin to grow. The number and size of crystals formed is then determined by a balance between the rate of nuclei formation and the growth of existing nuclei.

As the nuclei grow, the molecules arrange themselves into an ordered crystal structure. Crystals are strictly defined as having long range order characterized by a small repeating unit known as the unit cell. Depending on the crystallization

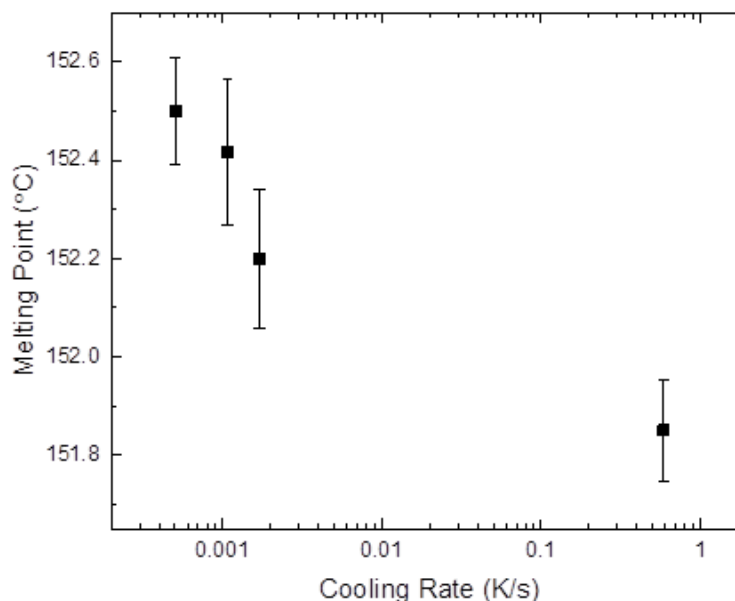


Figure 1.5: Adipic acid melting point decreases as cooling rate increases, indicating a decrease in crystal purity as a function of cooling rate.

conditions, the preferred orientation of molecules may vary, resulting in differing product crystal structures, known as polymorphs. This is of particular importance for specialty chemicals because different polymorphs can have vastly different properties. For example, the bioavailability of some pharmaceutical molecules varies based on the crystal structure. This is often the difference between “instant action” and “extended release” drugs.²²

For the sake of purity, it is generally preferable to grow well defined crystals instead of a rapidly formed precipitate. Because crystals exhibit preferential long range order, it is often thermodynamically unfavorable for impurities to be incorporated within the crystalline lattice. However, rapid, uncontrolled growth can lead to impurities becoming trapped within the crystalline lattice. For this reason, many purifications

involving crystallization are performed slowly, in order to minimize impurity incorporation. Figure 1.5 shows an example of this, where the melting point of adipic acid decreases as cooling rate increases, demonstrating that product purity increases as the solution is cooled slowly. Chapters 5 and 6 explore a novel crystallization technique, pressure-swing crystallization, which may yield similar purity improvements without the corresponding increase in overall crystallization time.

1.3.4. Sublimation

Sublimation is not a commonly practiced separation technique because it typically requires unfavorable operating conditions, most notably high vacuum. In this technique, the solid-vapor transition is exploited to obtain a separation. The starting material is typically a powder containing the target material along with a variety of impurities. This powder is heated under vacuum until the target material sublimates. The vapor is then

collected some distance away in a colder zone. In general, larger impurity molecules do not sublime and smaller impurity molecules do not condense and remain in the vapor phase. The most basic form of this technique is sometimes referred to as “cold finger” purification. Figure 1.6 shows a schematic of a cold finger sublimation apparatus. The target material is placed in a heating mantle and sublimed under vacuum. The vapor condenses on a cooled tube known as a cold finger. In more

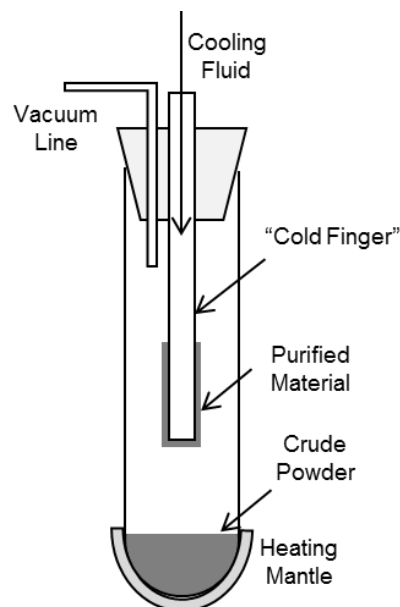


Figure 1.6: Schematic of a typical cold finger sublimation purification process.

complicated systems, a temperature gradient is applied within the collection zone such that each component of the vapor phase deposits in a spatially independent region. This technique is known as thermal gradient sublimation and was developed to purify large organic molecules in the 1970s and is still practiced in chemistry labs today.²³

Due to the costs associated with operating at high vacuum, purification via sublimation is usually reserved for molecules that are not amenable to purification via other techniques. This is often true for organic semiconductors due to their limited solubility in common solvents and relatively large molecular weight. Thermal gradient sublimation has been rapidly deployed at the industrial scale due to the recent increase in demand for organic semiconducting materials, driven mostly by the consumer display market. Although successfully practiced at the industrial scale, many questions surrounding this purification technique remain. Chapters 3 and 4 aim to explain both the fundamental mechanisms underlying this technique and offer some insights for potential process improvements.

1.4. Common Purification Challenges

In general, purification is an essential step in any chemical production process. Nowhere is this more important than within the specialty chemicals industry, where high value, high purity products are standard. The production of a wide variety of unique and complex chemicals necessitates a varied portfolio of purification techniques. This has resulted in a wide variety of technical challenges associated with specialty chemicals purification. A few of these challenges will be summarized here, in preface to the remainder of this dissertation.

One such issue is that the staple separation techniques of distillation and extraction are often unsuitable for specialty chemicals. These techniques require liquid-vapor or liquid-liquid equilibrium to be established. This is often not possible for specialty chemicals, whose large molecular structures degrade at high temperature and often provide limited solubility. For this reason, alternative, expensive purification techniques are often required.

Another common issue encountered during production is simply measuring the purity of the product material. The purity required to meet the desired performance characteristics is sometimes above that which is measurable using standard analytical chemistry techniques, making quality control difficult. This is especially apparent in organic semiconductors, where even small amounts of impurities can have a drastic impact on electrical performance.

Finally, due to the complexities involved in chemical synthesis, many of the impurities commonly encountered have similar molecular structures to the target molecule. This often causes complex separation challenges because these similar molecules often have similar solubility, thermodynamic properties, and potentially can integrate into the crystal structure of the target molecule. Together, these issues combine to make the purification of specialty chemicals an interesting and technically challenging field.

2. Instrumentation and Methods

A variety of experimental and analytical techniques were employed to study two purification processes, thermal gradient sublimation and crystallization. These processes are critical to the production of many specialty chemicals and provide unique technical challenges. The following sections describe these purification processes in detail, along with the equipment and analytical techniques used to study them.

2.1. Thermal Gradient Sublimation

As described briefly in the previous chapter, thermal gradient sublimation exploits the solid-vapor phase transition to affect a separation. As in distillation, a temperature gradient is used to manipulate the solid-vapor equilibrium between the target material and any impurities. This technique is practiced both at the laboratory and industrial scale, and is the primary purification technique used during the production of small molecule organic semiconductors.²⁴⁻²⁷ Due to the cost associated with operating at high vacuum, the use of this technique is often limited to those materials which are not amenable to purification using other techniques.

2.1.1. Equipment Design

In thermal gradient sublimation, impure material is placed in a quartz sample boat at the sealed end of a long, quartz tube. A high vacuum is applied to the open end (10^{-3} - 10^{-4} Pa) and the tube is placed in a multi-zone furnace. The sample boat is heated, causing the target material to sublime and travel down the tube. A temperature gradient is applied along the tube so that the components are separated according to their vapor pressures. Figure 2.1 shows a schematic of this process. Heavy impurities tend to remain

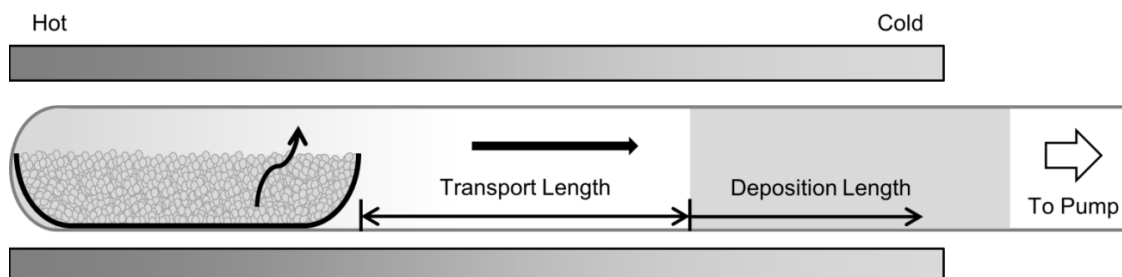


Figure 2.1: Schematic of typical thermal gradient sublimation system.

in the sample boat or deposit early in hot region of the tube, while light impurities travel farther down the tube prior to deposition. To facilitate material collection, the sublimation tube is typically lined with short quartz sleeves to prevent material deposition directly on the tube wall. These sleeves are removed after sublimation and the product material is collected by manually scraping it from the tube walls.

One issue that is often encountered during thermal gradient sublimation is that materials tend to deposit in a semi-continuous band throughout the deposition region. In cases where multiple impurities are present, it can be difficult to distinguish which material to collect. This is illustrated more clearly in Figure 2.2 which is a photo of the deposition region following thermal gradient sublimation of NPD. Traditionally, the product material is selected by optical characteristics and tested later for purity. This major issue for product yield and quality will be discussed in more detail in Chapter 4.

All experiments within this dissertation were conducted using a home-built



Figure 2.2: Photo of a typical collection tube after the thermal gradient sublimation of NPD.

sublimation system with an inner tube diameter of 3.5 cm and a heated length of 61 cm.^{24,27} The furnace used had three independently controlled temperature zones. The first zone was used solely to heat the sample boat while the second and third zones were used to control the temperature gradient of the deposition region. The diameter of collection sleeves was typically 3 cm, but was also varied in order to determine the effect of tube diameter on sublimation rate as discussed in Chapters 3-4. The sample boats used had a constant width of 3 cm with a length varying from 3.8 to 25 cm. This system represents a typical laboratory setup used to purify batches on the 0.1-10 gram scale.²³⁻²⁵ For industrial production on the kilogram scale, systems with a tube diameter of 30 cm or larger are often employed.²⁴

2.1.2. Experimental Methodology

The sublimation procedures employed were similar to those common within the field. In order to minimize contamination, all glassware used during experimentation was thoroughly cleaned using a 3:1 sulfuric acid and 30% hydrogen peroxide etch followed by a 500°C bake under vacuum. All glassware was weighed carefully before and after loading each sample. After loading, the system was allowed to pump down to a base pressure of 10^{-5} Pa at 120°C in order to remove any residual solvents from the sample or the glassware. The total rate of sublimation was calculated by measuring the mass lost from the boat over the experimental time. To measure the mass deposited as a function of position within the tube, the tube was lined with 1 cm wide quartz rings weighed before and after sublimation.

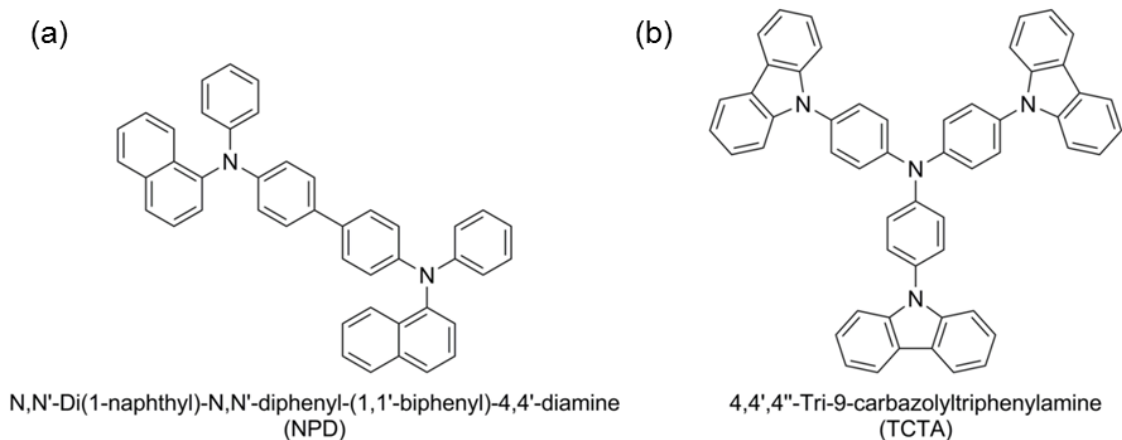


Figure 2.3: (a) NPD Molecular Structure. (b) TCTA Molecular Structure.

For experiments where only transport, and not separation data were obtained, the temperature within the furnace was maintained at a constant operating temperature. In this case, the temperature profile was uniform throughout the furnace and dropped linearly to room temperature at the exit of the furnace due to conduction. In cases where separation was studied, desired temperature gradients were obtained by independently adjusting the power output from each furnace zone. In all cases, the operating temperatures were measured at the outside surface of the tube wall.

Two common hole transporting materials shown in Figure 2.3, *N,N'*-di-[(1-naphthyl)-*N,N'*-diphenyl]-1,1'-biphenyl)-4,4'-diamine (NPD) and 4,4',4''-tris(carbazol-9-yl) triphenylamine (TCTA), were used as model compounds. The NPD and TCTA powder used for sublimation experiments was synthesized by the Dow Chemical Company. A brief discussion of the synthetic details for NPD is provided in Appendix A. TCTA was synthesized according to literature procedures.²⁸ For experiments containing mixtures of TCTA and NPD, the powders were mixed with a spatula prior to sublimation.

2.2. High Pressure Crystallization

Crystallization is an essential process throughout the chemical business. Crystallization is the focus of a considerable amount of research, but significant questions still remain, particularly surrounding nucleation.²⁹ The focus of this dissertation will be the development of a novel crystallization technique: pressure-swing crystallization. As the name states, pressure-swing crystallization utilizes swings in pressure to control crystallization. This approach is orthogonal to traditional crystallization techniques which involve modifying temperature or solvent to control crystallization. While still a novel research area, pressure-swing crystallization has a variety of potential applications, which are discussed in more detail in Chapter 6.

2.2.1. Equipment Design

Due to the novel nature of the pressure-swing technique, a custom high pressure crystallizer was designed and constructed. The crystallization vessel itself is a custom high pressure reactor fabricated by the High Pressure Equipment Company. The reactor consists of a piston and cylinder design as depicted in Figure 2.4. Pressure, applied on one side of the piston using a Teledyne ISCO 100DX high pressure syringe pump with water as the working fluid, is measured using a transducer integrated into the pump. Samples are loaded on the opposite side of the piston and can be observed visually through quartz windows. The sample solution is stirred using a magnetic stir bar and external magnetic stirrer. Temperature is measured using a thermocouple directly in contact with the sample solution through a high pressure thermocouple port. External heating is provided using heat tape connected to a standard external PID temperature controller. Active cooling is achieved by manually regulating the flow of cooling water

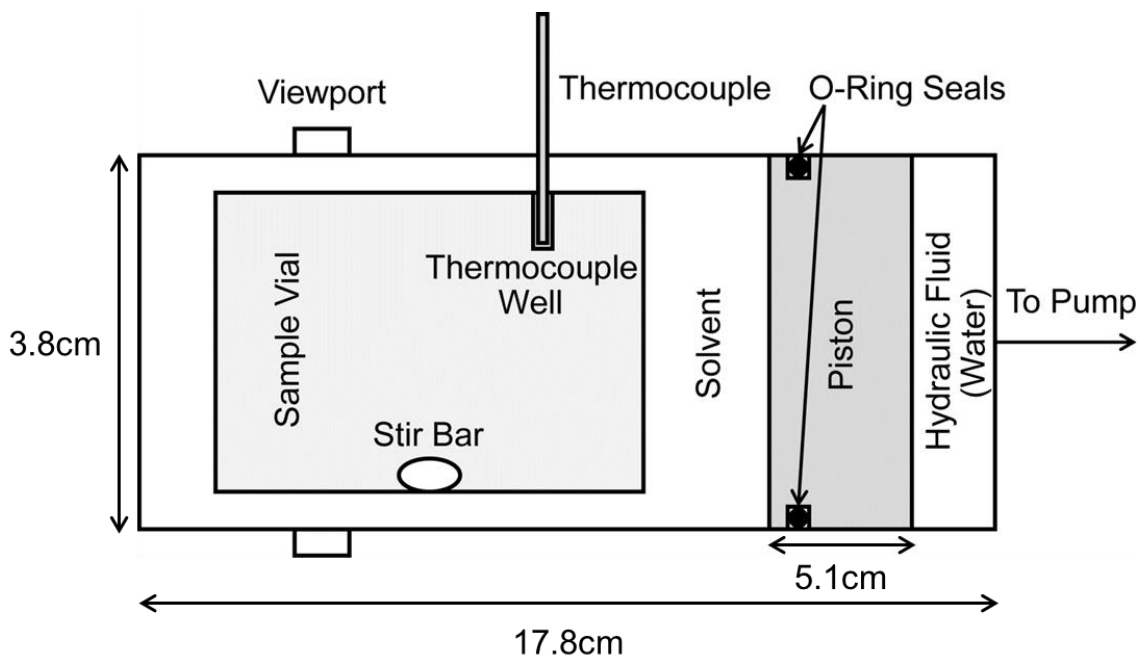


Figure 2.4: Schematic of pressure-swing crystallization system.

through a custom copper heat exchanger in contact with the outside of the pressure reactor. Figure 2.5 shows a photo of this entire apparatus. Experimental control and data acquisition are managed using a PC with the LabVIEW data acquisition software package. A copy of this control software is available in Appendix B.

As configured, the crystallization system has a maximum sample volume of 150 mL and can operate at pressures up to 10,000 psig. The maximum operating temperature is limited to 100°C due to the use of water as the hydraulic operating fluid. Due to the thermal mass of the high pressure crystallizer, the overall heating and cooling rates of the reactor are limited to approximately 0.7°C/min. and 0.4°C/min. respectively. During pressure swing operations, the maximum pressurization rate is approximately 500-1000 psi/second, depending on the sample volume and solvent.

In addition to experiments using the pressure crystallization system, a significant number of benchtop crystallization experiments were conducted for screening and

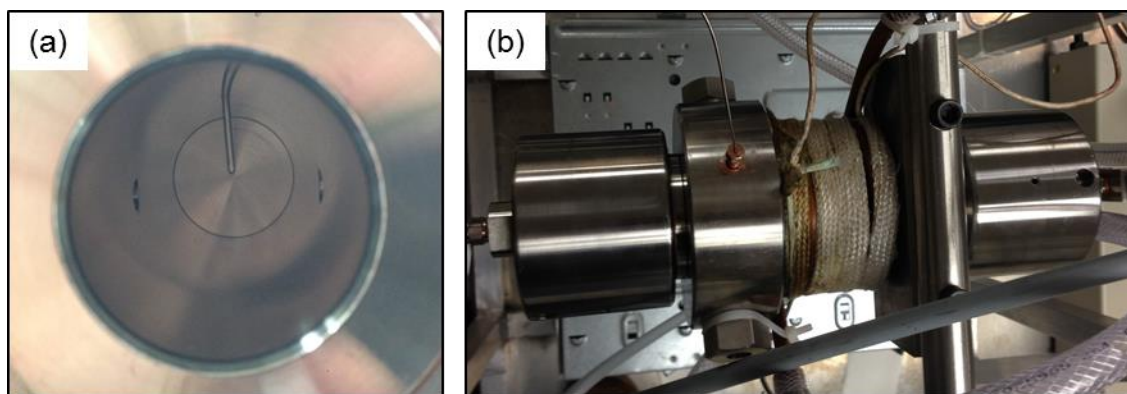


Figure 2.5: Photographs of the (a) interior and (b) exterior of the pressure-swing crystallization system.

validation purposes. In these cases, an OMEGA stirring hot plate equipped with an aluminum heating block and feedback temperature control was used. Samples were prepared in 20 mL glass scintillation vials. This allowed for significantly increased throughput compared to the pressure crystallizer.

2.2.2. Experimental Methodology

Samples were prepared by mixing a known mass of a target solute with a known mass of the desired solvent. Solubility data were taken both from the literature and experiment as described in Chapter 5. Preparation was conducted both directly inside the pressure crystallization system and outside the crystallizer in a separate 30 mL polyethylene vial, which was later loaded into the system. In the case where an external vial was employed, accurate temperature measurements were obtained by fitting the thermocouple through the reactor wall into a thin aluminum thermocouple port in the sample vial wall. During sample preparation, significant care was taken to minimize the amount of air incorporated into the sample. Before beginning experiments, samples were heated to 10°C above the saturation temperature with stirring for more than two hours to completely dissolve the solute.

For experiments involving nucleation, the nucleation temperature was recorded accurately by noting the characteristic spike in temperature due to the heat of crystallization. As an example, this temperature increase is shown in Figure 2.6 for

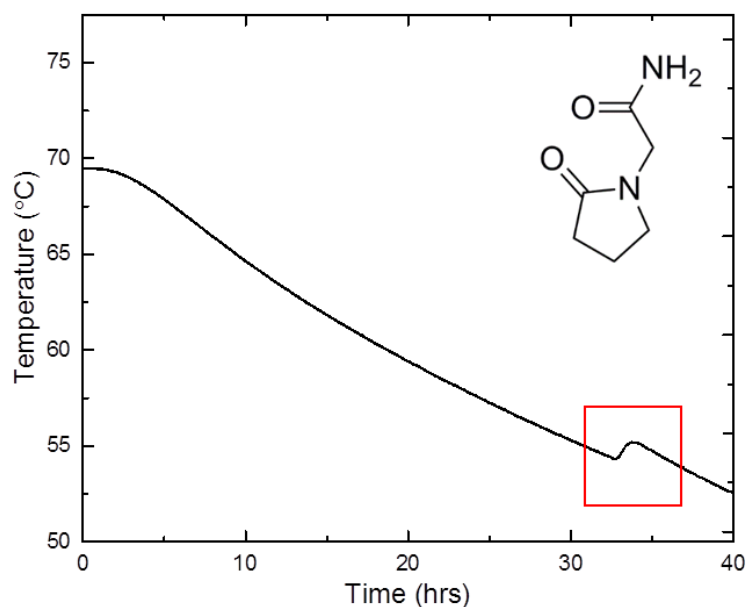


Figure 2.6: (Graph) Characteristic increase in temperature due to nucleation for piracetam in ethanol. (Inset) Piracetam molecular structure.

the crystallization of piracetam in ethanol. Due to the rapid onset of crystal growth during nucleation, the energy associated with the liquid-solid phase transition results in a noticeable increase in the overall solution temperature. The temperature change due to crystallization can be estimated if the heat of crystallization is known, according to²¹

$$\Delta T = \frac{\Delta H^C m^C}{m C_P} \quad (2.1)$$

where ΔT is the change in temperature, C_P is the heat capacity of the solution, m is the mass of the solution, ΔH^C is the heat of crystallization, and m^C is the mass of crystals formed. In addition to temperature measurements, nucleation was also confirmed by visual observation using the quartz viewing windows.

After crystallization, product crystals were collected via vacuum filtration. In all cases, the resulting slurry was filtered using a Büchner funnel attached to an aspirator.

The product crystals were not washed after filtration to avoid product loss and minimize experimental error. The filtrate was allowed to dry on the filter before transfer to a glass sample vial for later analysis, typically within 24 hours. For experiments using water as a solvent, an additional drying step was added, where the product crystals were heated overnight at 50°C to ensure complete solvent evaporation. Dried crystals were stored at room temperature until analysis shortly after experiment.

2.3. Analytical Techniques

A variety of analytical techniques were employed in order to determine the quality of product materials. In general, products were assessed for chemical purity, but for some experiments, crystal size, morphology, and structure were also analyzed. This section provides a brief overview of the techniques used to conduct this analysis and describes a custom technique used to measure the liquid density of high melting organic materials.

2.3.1 Optical Microscopy

Optical microscopy provides a simple, yet powerful tool for analyzing product crystals. The product from both crystallization and thermal gradient sublimation is typically a polycrystalline powder. Optical microscopy provides a detailed picture of the product crystals using a white light source coupled to specialized lenses and a digital camera. Detailed coverage of the design and operation of an optical microscope can be found elsewhere.³⁰ For this dissertation, optical microscopy was used only to roughly compare crystal size and morphology. Experimentally, a Nikon Eclipse CI-L microscope equipped with polarizing filters and an Infinity CMOS camera was used for all optical

microscopy work in this dissertation. Detailed statistical analysis of crystal size did not yield additional insights, but when employed, was conducted using the Image J software package.³¹

In addition to determining crystal size and morphology, optical microscopy was also used to assess crystallinity through the use of polarized light. In polarized light microscopy, pictured in Figure 2.7, the normal white light source is passed through a polarizer before interacting with a sample. Because many organic crystals exhibit birefringence, the incident polarized light exits the sample with an orientation dictated by the crystallinity of the sample. A second, adjustable polarizer is placed after the sample and blocks all light that is not rotated by the sample. This provides a simple test to determine whether the product solid is crystalline or not. It also provides for some qualitative measure of the polycrystallinity of the sample because crystal domains often become clearly visible under polarized light.

In some cases, optical microscopy can also be used to determine crystal structure. Based on nucleation and growth conditions, molecules may arrange themselves into a variety of thermodynamically or kinetically favored states. In some cases, this molecular ordering can result in macroscopic changes in

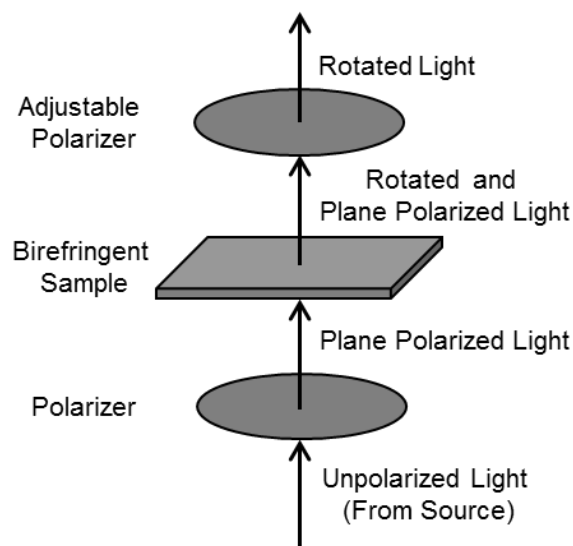


Figure 2.7: Schematic of traditional polarized light microscopy.

crystal shape. This is most clearly demonstrated by 5-Methyl-2-[(2-nitrophenyl)amino]-3-thiophenecarbonitrile (ROY) which has at least nine known distinct polymorphic forms, each with a unique optical appearance.³² While crystal shape does not provide a definitive measure of crystal structure, it often provides a simple tool for screening product crystals.

2.3.2 Melting Point

Like optical microscopy, measurement of melting points provides a quick and convenient tool for assessing purity. The technique uses the thermodynamic principle of melting point depression to provide a relative measure of material purity. Simply put, this principle states that the more impurities present in a material, the lower the melting point. Melting point depression is a colligative property, such that regardless of the identity of the impurity, the decrease in melting point is given by³³

$$\Delta T = K_f b \tag{2.2}$$

where ΔT is the decrease in melting point, K_f is the cryoscopic constant of the target material, and b is the molality of the impurity. In theory, this technique can provide a quantitative measure of the sample purity, but requires significant external calibration.

Experimentally, the melting point of a material can be measured using a straightforward approach. A few milligrams of the material of interest, in powder form, are packed into the bottom of a capillary tube. The tube end is generally sealed to minimize evaporation or sublimation. The capillary is then heated slowly until the powder liquefies. The melting point is typically determined optically, either from image analysis or by eye. The melting point analysis conducted in this dissertation used a

MPA100 automated melting point system from Stanford Research Systems with a heating rate of 1°C/min. The melting point was taken to be the clear point as determined by optical image analysis.

2.3.3 Differential Scanning Calorimetry

While melting point is a useful technique for roughly comparing the purity between two samples, it does not typically provide a quantitative measure of purity. Differential scanning calorimetry (DSC) is a more advanced technique that relies on the same principle of melting point depression to quantify material purity. In DSC, a small amount of the target material is heated slowly while both the sample temperature and heat flow into the sample are measured. The data are compared directly to that of an empty control cell, allowing measurement of the heat flow due to both heating and phase transformations associated with the sample. Unlike the traditional melting point technique, DSC allows for a direct measurement of the heat of fusion of the sample in addition to the melting point. Figure 2.8a shows as an example the heat flow curve during the melting of adipic acid. Quantitative purity analysis can be conducted using the van't Hoff Equation³⁴

$$T_s = T_0 - \frac{RT_0^2 \chi}{\Delta H_F F} \quad (2.3)$$

where T_s is the sample temperature, T_0 is the pure melting temperature, χ is the mole fraction of impurity, ΔH_F is the heat of fusion, and F is the fraction of the sample melted. To use this equation, the onset slope of the melting curve is fit according to Equation 2.3 to determine the mole fraction of impurity. This analysis is shown for adipic acid in Figure 2.8b.

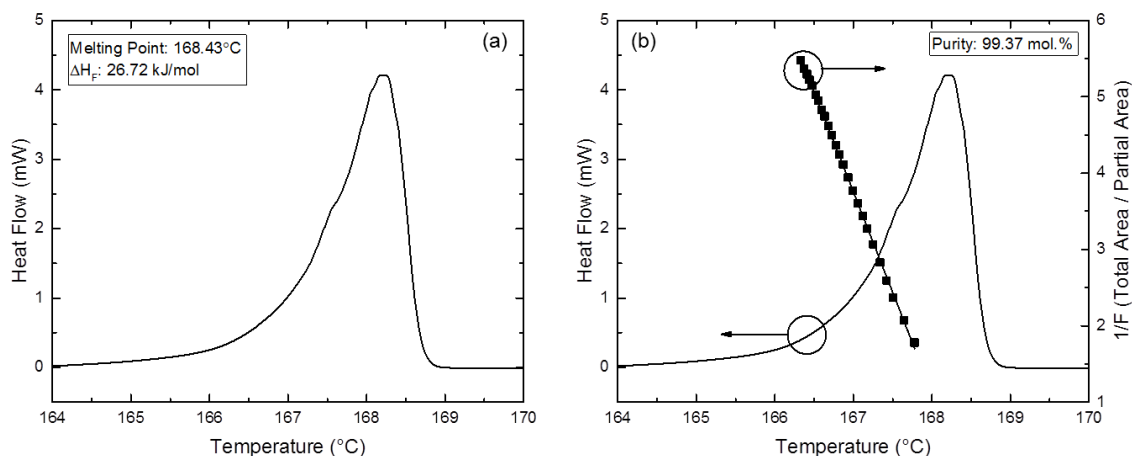


Figure 2.8: (a) Adipic acid DSC curve with melting point and heat of fusion. (b) Purity analysis of adipic acid DSC curve. The fraction melted is plotted as a function of temperature and fit according to Equation 2.3.

Quantitative DSC purity analysis was used to determine the purity of crystalline samples produced during pressure-swing crystallization experiments, specifically those related to crystal digestion discussed in Chapter 6. In all cases, a TA Instruments Q1000 DSC was used with a liquid nitrogen cooling system and a helium purge flow. All experiments were conducted according to ASTM Standard E928-08.³⁴ Data analysis was conducted using the TA Universal Analysis software package.

2.3.4 High Performance Liquid Chromatography

High performance liquid chromatography (HPLC) is a common analytical technique used to separate and analyze complex organic mixtures. In this technique, the sample of interest is dissolved in a solvent or mobile phase. The sample is injected at high pressure into a packed column of absorbent material. A flow of the mobile phase forces the sample through the column and individual components are separated based on their adsorption to the column packing. An analyzer measures the relative amount of each component as they exit the column, providing a quantitative measure of purity. Due

to the separate nature of the column and analyzer, multiple analytical techniques can be employed, including ultraviolet–visible (UV/Vis) spectroscopy and mass spectrometry.³⁵

HPLC was used to obtain the purity of organic electronic materials purified via thermal gradient sublimation. HPLC analysis was conducted by The Dow Chemical Company using an Agilent 1200SL binary gradient liquid chromatograph coupled to an Agilent 6520 QToF, quadrupole-time of flight mass spectroscopy (MS) system via a dual spray electrospray interface operating in the positive ion mode. Solutions were typically prepared in tetrahydrofuran. For structure determination, the time of flight mass spectrometer was scanned from 50 to 1700 amu at a rate of 3 scans per second, alternating between the MS and MS/MS modes. Nitrogen gas with a collision energy of 65V was employed in the MS/MS mode. The purity of the materials was determined by area percent assay of the summed UV response from 210 to 600 nm.

2.3.5 X-Ray Diffraction

X-ray diffraction (XRD) is typically used to determine the molecular structure of crystalline materials. In XRD, a beam of x-rays is aimed at the sample surface while the intensity and angle of the diffracted beam is measured. Each molecular structure produces a unique set of emissions, or diffraction pattern. This pattern can be used to distinguish between similar polymorphic structures or to determine the structure of unknown materials using Bragg's Law.³⁶ Typically, XRD spectra are presented as diffraction intensity vs two times the incident angle, or 2θ . These plots can be compared directly to reference spectra for known molecular structures. Figure 2.9 shows an example of this type of analysis, where the XRD spectra for piracetam crystallized under

two different experimental conditions are compared to reference spectra.³⁷ It is immediately obvious from the plot that piracetam crystallized rapidly exists as the polymorphic Form II, while piracetam that is

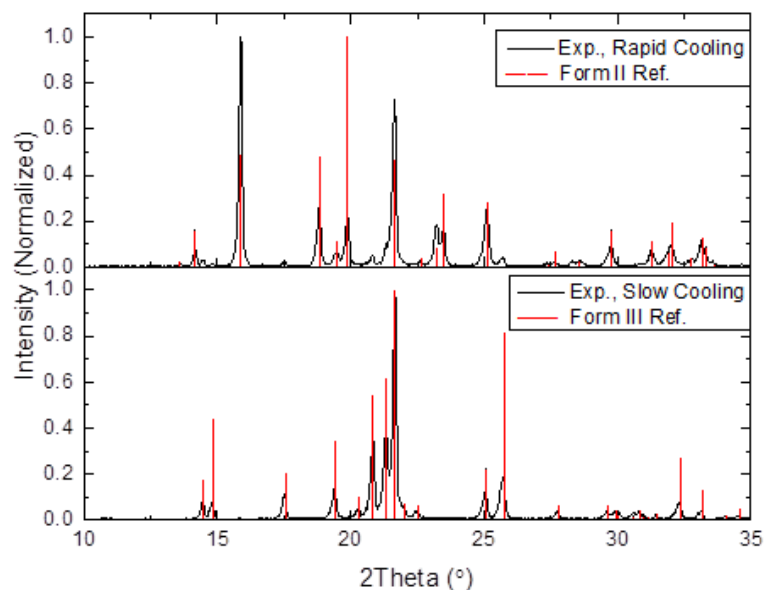


Figure 2.9: Comparison between the XRD spectra of two different polymorphs of piracetam.

crystallized slowly exists as polymorphic Form III. This behavior will be discussed in more detail in Chapter 6.

XRD was primarily used to identify various polymorphic forms of organic crystals produced using pressure-swing crystallization. To that end, powder XRD diffraction spectra were obtained using a Bruker-AXS D5005 Diffractometer with 2.2 kW sealed Cu source. All spectra were taken with a 2Θ resolution of 0.02° and a dwell time of one second. Data analysis was conducted using the JADE 8.0 software package.

2.3.6 Liquid Density Measurements

The liquid density of both paracetamol and piracetam is required to validate the thermodynamic solubility theory developed in Chapter 5. The high melting point of both compounds makes them hard to study with commercial instruments, so a home-built setup was constructed. The setup consists of a graduated cylinder housed in a custom

aluminum heating block. The heating block is mounted on a standard laboratory hot plate with feedback temperature control. The temperature of the block is measured near the surface of the graduated cylinder using a thermocouple inserted into a dedicated port. A small slit cut into the side of the heating block allows for volumetric readings to be taken without significantly reducing the temperature of the cylinder.

Experimentally, a known mass of solid powder was packed into the graduated cylinder and sealed tightly with a cork. The cylinder was loaded into the heating block and the entire assembly was heated to the melting point of the target material. Once the solid had melted, the liquid volume was simply read from the graduated cylinder. Using this technique, the liquid densities of paracetamol and piracetam were measured to be 1.13 ± 0.02 g/mL and 1.14 ± 0.01 g/mL, respectively. This approach can be used to measure the liquid density of any solid that does not degrade before melting.

2.3.7. Vapor Pressure Measurements

As discussed in more detail in Chapters 3 and 4, the vapor pressure of organic semiconducting molecules is the driving force for vapor transport in thermal gradient sublimation. In order to model this process effectively, the vapor pressure of the two model compounds studied, NPD and TCTA was measured using an isothermal thermogravimetric effusion method by The Dow Chemical Company.³⁸ In this technique, the material to be measured is held at constant temperature in an evacuated sample container. Heated material is allowed to escape from the container through a small hole of known diameter and is collected on the pan of sensitive balance. When the

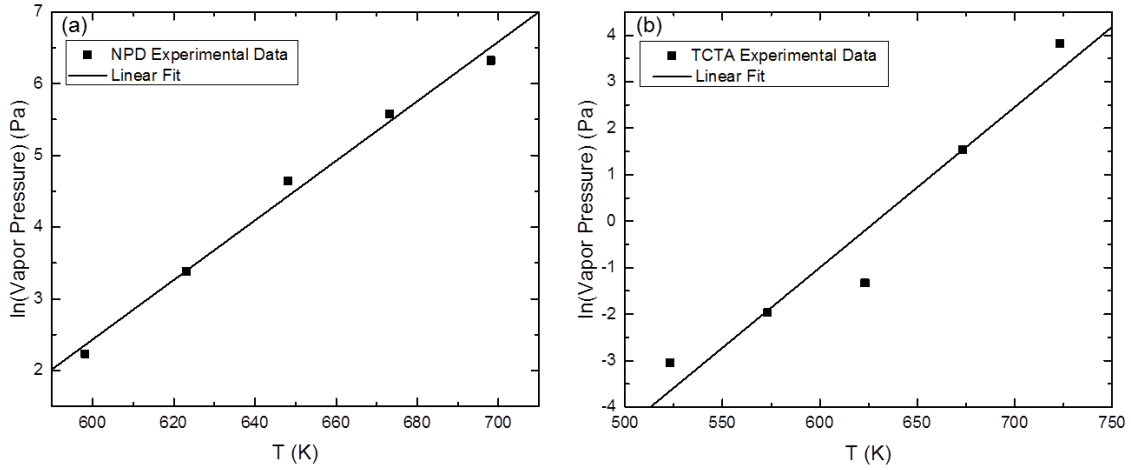


Figure 2.10: Vapor pressure as a function of temperature for (a) NPD and (b) TCTA.

material in the sample container is at equilibrium, the rate of material leaving through the hole can be related to the vapor pressure using the Hertz-Knudsen equation:³⁹

$$P^{vap} = G \sqrt{\frac{2\pi RT}{m}} \quad (2.4)$$

In this equation, P^{vap} is the vapor pressure, G is the flux of material through the sample container hole, R is the gas constant, T is the temperature, and m is the molar mass.

This technique was used to measure the vapor pressure for both NPD and TCTA as shown in Figure 2.10. Due to the limited nature of the data, simple exponential fits were used to extend the experimental data to the temperature ranges employed in the sublimation experiments. These fits, shown below for NPD and TCTA respectively, were used in the calculations described in Chapters 3 and 4.

$$\ln(P_{NPD}^{vap}(Pa)) = (0.0415 \pm 0.0024) \times T(K) - (22.5 \pm 1.5) \quad (2.5)$$

$$\ln(P_{TCTA}^{vap}(Pa)) = (0.0345 \pm 0.0051) \times T(K) - (21.7 \pm 3.2) \quad (2.6)$$

This data provides an experimental basis for calculating the rate of sublimation. However, extending the experimental data in this way likely introduces a significant error into our calculations, as discussed in more detail in Chapter 4.

3. Rate-Limiting Steps in Thermal Gradient Sublimation

Organic semiconductors continue to receive substantial attention for use in next generation display and lighting applications.^{40,41} The performance and device lifetime of organic light-emitting devices (OLEDs) based on these materials depends, in part, on the purity of the starting material.^{17,42-49} For low molecular weight materials, the primary method for purification is thermal gradient sublimation.²³ The experimental details of this technique are covered in detail in Chapter 2. While widespread in its use, the fundamental science underlying this technique is underexplored, leading to an often empirically optimized and qualitative practice in industry. The limited understanding of the underlying material transport mechanisms in this system may have compromised and retarded the improvement of material yield and ultimate scale-up for industrial applications.

Thermal gradient sublimation is well studied with regards to producing large crystals.⁵⁰⁻⁵² However, limited literature is available characterizing the relevant separation mechanism. Earlier work has shown how adding baffles within the sublimation tube can be used to increase the separation by artificially reducing the slope of the temperature gradient.^{25,26} The work in this dissertation aims to better quantify the transport mechanisms involved in thermal gradient sublimation and examine approaches to increase separation and throughput. Towards this aim, this chapter will focus on determining the characteristic rate-limiting step within the sublimation process while

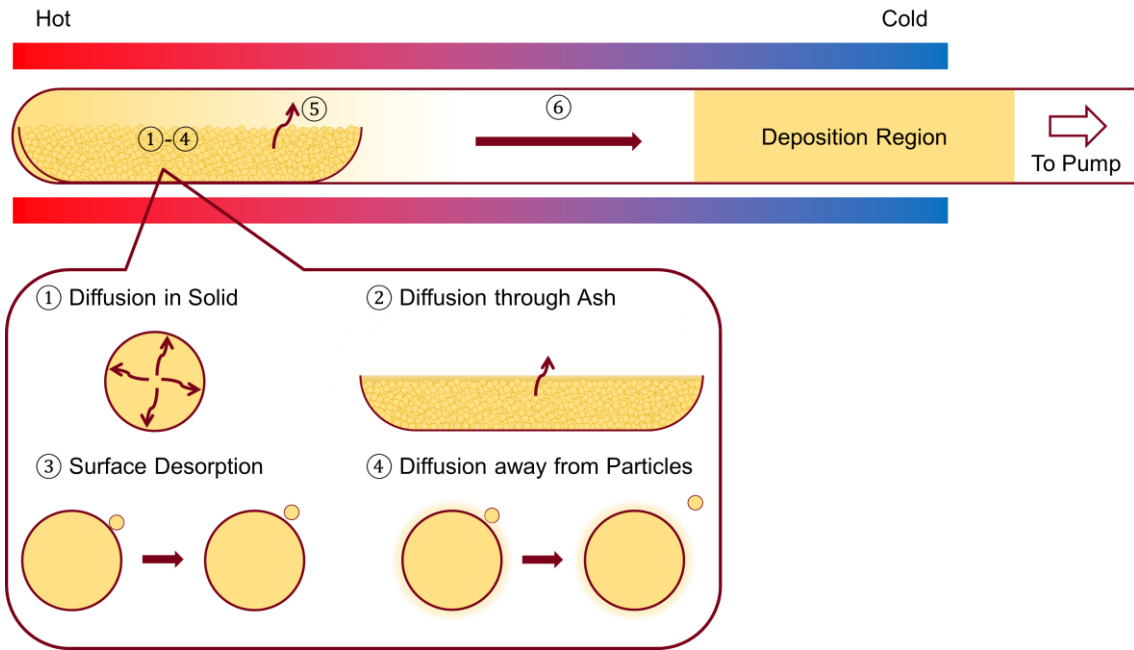


Figure 3.1: Potential rate-limiting steps for thermal gradient sublimation. Mechanisms 1-4 occur in the solid phase, mechanism 5 is mass transfer away from the sample boat, and mechanism 6 is vapor phase transport and deposition within the tube.

Chapter 4 will focus on developing a detailed transport model to guide scale-up and separation.

3.1. Potential Rate-Limiting Steps

The controlling rate in the sublimation process can be thought of as the product of the key surface area involved and the flux, that is, the amount sublimed per area per time. This product, integrated over time, is the yield of the process. To estimate the yield, we first consider possible rate controlling mechanisms, shown schematically in Figure 3.1. Here, six possible mechanisms are analyzed in significant detail, listed in order according to Figure 3.1: diffusion within solid particles, diffusion within a composite solid, surface desorption, diffusion away from the particle surface, mass transfer away from the boat containing the feed material, and mass transfer from the boat to the collection zone. The

last case can be further distinguished by identifying the mechanism of mass transfer as ballistic transport, Knudsen diffusion, intermolecular diffusion, or viscous flow. A key surface area and flux will be derived for each of these mechanisms, such that the theoretical dependence on experimental conditions can be compared directly to specific experiments involving NPD and TCTA. However, these estimates are general, and could be applied to a variety of sublimation processes.

3.1.1. Diffusion within Solid Particles

This case is expected to apply most often to very impure feeds, especially those where the desired product forms particles of a solid solution or a co-crystal with an impurity. In this case, the key area is the total area of the particles A , given by

$$A = \frac{\text{total mass}}{\text{density}} \frac{\text{particle area}}{\text{particle volume}} = \frac{3M}{\rho r} \quad (3.1)$$

where M is the total mass, ρ is the particle density, and r is the particle size, expressed as an average radius. At short times t , the flux j_1 of the target species out of each particle is:²⁰

$$j_1 = \sqrt{\frac{D^{Solid}}{\pi t}} c_1^{Solid} \quad (3.2)$$

where D^{Solid} is the diffusion coefficient of the target species in the solid, and c_1^{Solid} is its initial concentration.

3.1.2. Diffusion within a Composite Solid or Ash

In this mechanism, which applies to very impure feeds, the target species evaporates quickly from small particles assembled in a composite solid. After the evaporation, a porous ash layer of less volatile impurity remains. Evaporation continues from the “shrinking core” of unsublimed target material within the ash-coated solid. The

area in this case will be that given by Equation 3.1 for dispersed particles, but equal to the boat area if the particles are assembled as a packed bed. Only the packed bed case will be considered here. A mass balance on a differential volume in this packed bed gives:²⁰

$$\frac{d}{dt} [c_1^{Solid} l] = \frac{D^{Vapor}}{l} c_1^{Vapor} \quad (3.3)$$

where c_1^{Vapor} is the concentration of the target species in the vapor, D^{Vapor} is the diffusion coefficient in the vapor; and l is the thickness of the ash layer. Since this thickness is initially zero, Equation 3.3 can be integrated over time to give:

$$l = \sqrt{\frac{2D^{Vapor} c_1^{Vapor} t}{c_1^{Solid}}} \quad (3.4)$$

The flux out of the packed bed is thus

$$j_1 = \frac{D^{Vapor} c_1^{Vapor}}{l} = \sqrt{\frac{D^{Vapor} c_1^{Vapor} c_1^{Solid}}{2t}} \quad (3.5)$$

Now, the flux increases with the square root of c_1^{Vapor} , unlike the linear relationship shown by the other proposed mechanisms.

3.1.3. Surface Desorption

In this limit, which applies to nearly pure particles, the key area is that of the particles themselves, as given by Equation 3.1. The particle size changes as sublimation continues, as shown by the mass balance:²⁰

$$\frac{d}{dt} \left[\frac{4}{3} \pi r^3 c_1^{Solid} \right] = -k 4 \pi r^2 c_1^{Solid} \quad (3.6)$$

where k is a first order rate constant describing the rate of molecular detachment from the solid surface. If the initial particle radius is r_0 , Equation 3.6 is easily integrated to yield $r = r_0 - kt$. This mechanism has been observed for the sublimation of many ammonium

halides.^{53,54} The sublimation flux in this case is then just $j_1 = kc_1^{Solid}$. Taking into account the varying radius, the area given in Equation 3.1 can be combined with the flux, and when integrated over particle area and time, gives the mass sublimed.

3.1.4. Diffusion Away from the Particle Surface

Another case, closely related to the previous one, concerns small, nearly pure dispersed particles whose sublimation is controlled not by surface desorption but by diffusion from the particle surface into the surroundings. The mass balance on one particle is closely related to that in Equation 3.6:

$$\frac{d}{dt} \left[\frac{4}{3} \pi r^3 c_1^{Solid} \right] = - \left[\frac{D^{Vapor}}{r} \right] (4\pi r^2) c_1^{Vapor} \quad (3.7)$$

which can be compared to Equation 3.6 where the rate constant k has been replaced by the diffusion coefficient divided by the particle radius.²⁰ If the initial radius is r_0 , the integration of Equation 3.7 gives:

$$r^2 = r_0^2 - \frac{2Dc_1^{Vapor}t}{c_1^{Solid}} \quad (3.8)$$

and the flux is:

$$j_1 = \frac{2D}{r} c_1^{Vapor} \quad (3.9)$$

The mass sublimed is found from combining the last two equations and integrating over particle area and time. This case, which occurs in the sublimation of both iodine and aluminum oxide, was first analyzed by Langmuir.^{55,56}

3.1.5. Mass Transfer Away from the Sample Boat

In situations where mass transfer of a nearly pure vapor controls the sublimation, the vapor between the particles now reaches saturation. There are two cases which are

important: when sublimation is limited by mass transfer out of the boat, and when it is controlled by mass transfer along the tube. When mass transfer out of the boat is the slow step, the rate depends not on particle area, but on boat area. The flux is given by $j_1 = kc_1^{Vapor}$, where k is now a mass transfer coefficient for the product molecule in the vapor. The mass sublimed is obtained by integrating the flux over boat area and time.

3.1.6. Mass Transfer from the Boat to the Collection Zone

In this case, which turns out to be the most important one, low pressure vapor transport can occur via several different mechanisms dictated by the system geometry and the experimental conditions, most notably the operating pressure. At the conditions typically encountered during thermal gradient sublimation, four primary mechanisms are worth noting: ballistic transport, Knudsen diffusion, diffusion, and laminar flow. The detailed mathematics corresponding to each of these mechanisms will be discussed in detail in Chapter 4. However, for the sake of determining the rate-limiting step, it is clear that in each of these cases that the key area for each of these mechanisms is the cross sectional area of the tube $A = \frac{\pi d^2}{4}$, where d is the diameter of the sublimation tube. Additionally, the corresponding flux in each case is simply the vapor concentration multiplied by a characteristic velocity v

$$j_1 = c_1^{Vapor} v \quad (3.10)$$

In all cases except for ballistic transport, this velocity is inversely proportional to the transport length l , or in this case the distance from the boat to the deposition region. For example, in the case of diffusion, the characteristic velocity is²⁰

$$v^{Diff} = \frac{D^{Vapor}}{l} \quad (3.11)$$

where v^{Diff} is the characteristic velocity associated with diffusion, also known as a mass transfer coefficient. The characteristic velocity may also vary with the tube diameter, as is the case for Knudsen diffusion and laminar flow. This distinction is discussed in detail in Chapter 4. Together, this suggests that when vapor transport is the rate-limiting step, the sublimation rate should vary with the tube diameter and transport length. This prediction will be compared to experiment in Section 3.3.

3.2. Experimental Determination of Rate-Limiting Mechanisms

In Section 3.1, a key area and a flux were derived for each potential rate-limiting mechanism. The rate of sublimation is simply the product of the flux times that key area and the mass sublimed is the integral of the sublimation rate over the sublimation time. The results of these derivations are summarized in Table 3.1. This section will systematically probe these potential rate-limiting mechanisms by measuring the sublimation rate and total mass sublimed as a function of experimental conditions for two

Table 3.1: Key area and flux associated with each potential rate-limiting step for thermal gradient sublimation.

	Rate-Limiting Step	Key Area	Flux
1.	Diffusion within Solid Particles	Particles	$\sqrt{\frac{D^{Solid}}{\pi t}} c_1^{Solid}$
2.	Diffusion within a Composite Solid or Ash	Particles or Boat	$\sqrt{\frac{D^{Vapor} c_1^{Vapor} c_1^{Solid}}{2t}}$
3.	Surface Desorption	Particles	$k c_1^{Solid}$
4.	Diffusion Away from the Particle Surface	Particles	$\frac{2D}{r} c_1^{Vapor}$
5.	Mass Transfer Away from the Sample Boat	Boat	$k c_1^{Vapor}$
6.	Mass Transfer from the Boat to the Collection Zone	Tube	$c_1^{Vapor} v$

common hole-transporting organic semiconductors, NPD and TCTA. The detailed procedures for these experiments are provided in Chapter 2, but also summarized briefly here.

To measure

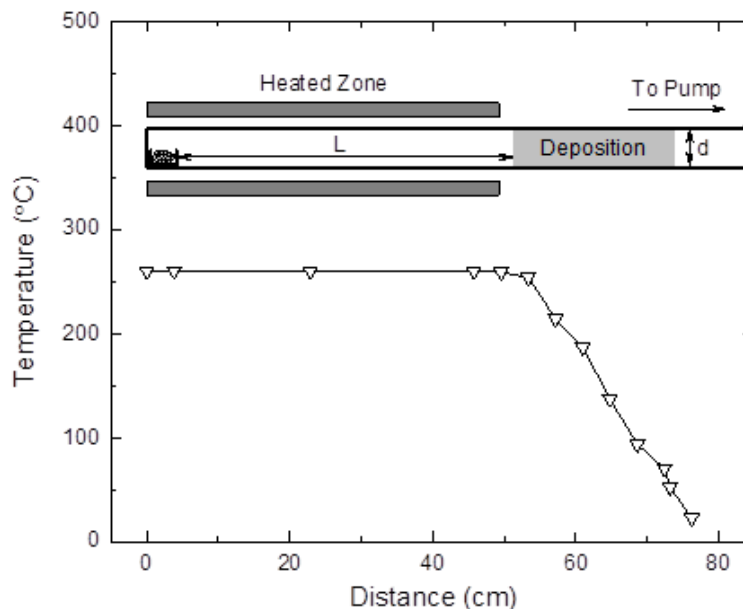


Figure 3.2: Temperature profile during a typical sublimation experiment involving NPD.

sublimation rate, a known amount of NPD or TCTA powder is loaded into the sublimation system. A constant temperature profile, an example of which is shown in Figure 3.2, is applied to the sublimation system. After a fixed time, the system is rapidly cooled and the amount of material remaining in the source boat is measured. The difference between the initial charge and the amount remaining is taken to be the amount sublimed. This value is used instead of the amount of product collected to limit experimental error associated with manual collection, but the deviation between the two values is typically less than five percent. This is attributed to the purity of the starting material, which is typically greater than 99%. The sublimation rate is simply the amount sublimed divided by the experimental time.

3.2.1. Sublimation Rate as a Function of Time

In order to determine whether the sublimation rate changes as a function of time, the mass of NPD sublimed was measured as a function of time using two different size sample boats. As shown in

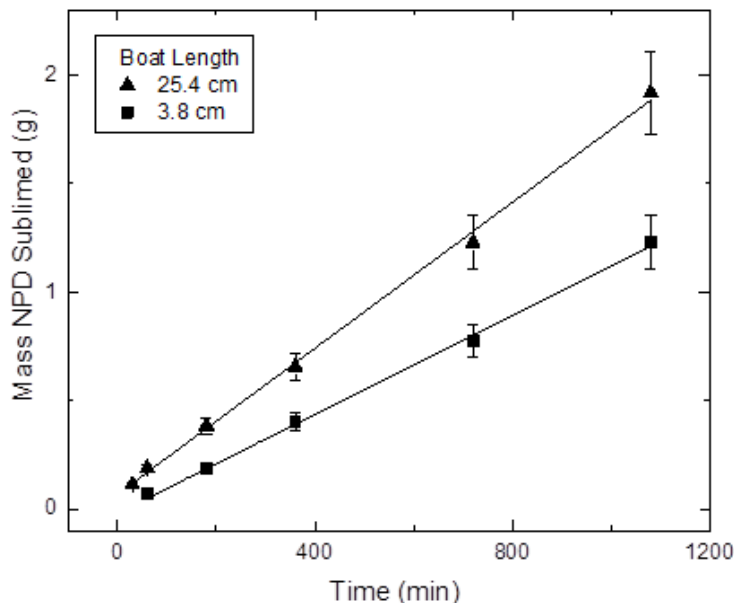


Figure 3.3: Mass sublimed is linear as a function of time. Sublimation rate does not change as a function of time.

sublimed is linear as a function of time for a given boat size, so the sublimation rate is not a function of time. The dependence on sample boat size will be discussed in more detail in Section 3.2.4. This result is clearly inconsistent with the flux expected for the first two mechanisms presented in Table 3.1, which are expected to vary with time. More subtly, mechanisms which include a dependence on the particle surface area may also exhibit a dependence on time because the total particle surface area is expected to change as material sublimes. Typically, the overall surface area should decrease as material sublimes, but may also increase if subliming material leaves behind a porous surface. In general, the result in Figure 3.3 demonstrates that sublimation of NPD is not controlled by diffusion within solid particles or within a composite solid. It also suggests that surface desorption and diffusion away from the particle surface are not rate-limiting.

3.2.2. Sublimation Rate as a Function of Particle Size

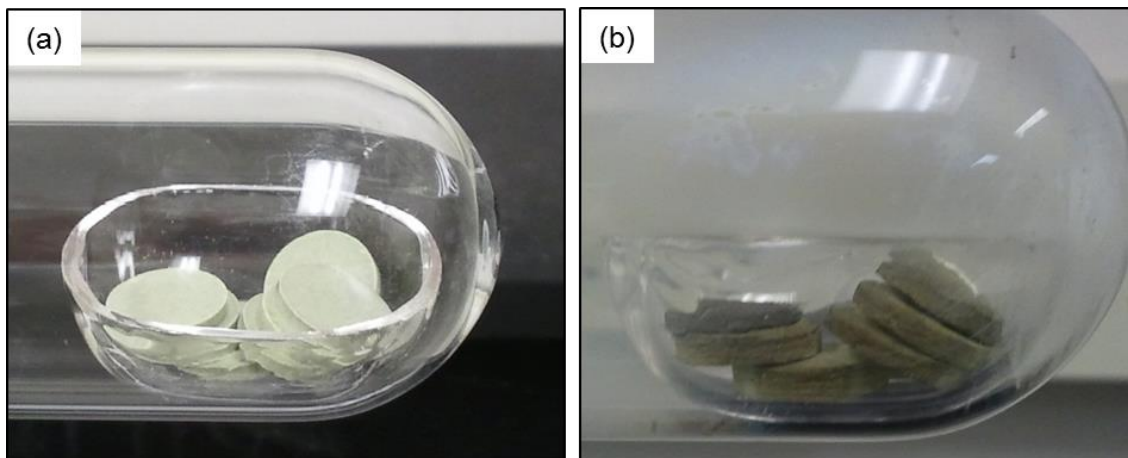


Figure 3.4: (a) Pressed pellets of NPD powder before sublimation. (b) Pellets after six hours of sublimation.

To support the suggestive sublimation rate vs. time data, the amount sublimed was directly measured as a function of particle size. This was accomplished by compressing the NPD powder typically used in experiments, which has average particle size on the order of $10\ \mu\text{m}$, using a 10 ton press to make pellets 1 cm in diameter and 2-3 mm in height. A photo of these pellets can be seen in Figure 3.4a. Starting with the same initial mass, the NPD pellets were found to sublime at the same rate as the loose powder. Sublimation was observed to occur only from the pellet surface, leaving behind a smaller, solid pellet, not a porous solid. This can be clearly seen in Figure 3.4b. These tightly pressed pellets show that even in an extreme case, sublimation rate does not depend on particle surface area.

3.2.3. Sublimation Rate as a Function of Initial Loading

In the same sense as particle size, the depth or initial loading of particles also governs the total particle surface area. To measure the impact of initial loading, various charges of NPD powder were sublimed over a six hour period. Figure 3.5 shows the mass sublimed plotted as a function of the initial mass loaded into the 3.8 cm long boat.

While the initial mass varies by a factor of four, the sublimation rate varies by about $\pm 10\%$, which is within the experimental error. Again these results show that the sublimation of NPD is not limited by the first four mechanisms in Table 3.1.

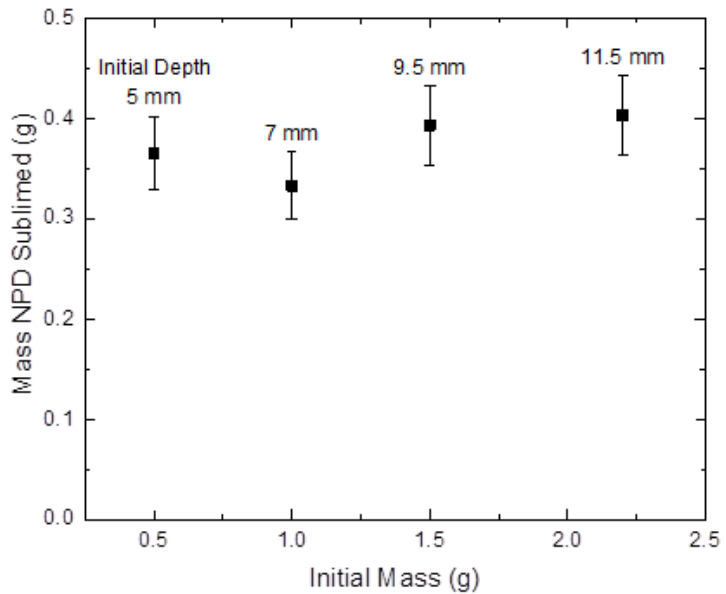


Figure 3.5: Mass sublimed is constant as a function of initial loading.

3.2.4. Sublimation Rate as a Function of Boat Area

The effect of boat area can be inferred from the data in Figure 3.3. In particular, the mass sublimed for the 25 cm boat is systematically greater than that for the 3.8 cm boat. This suggests that the boat area impacts the sublimation

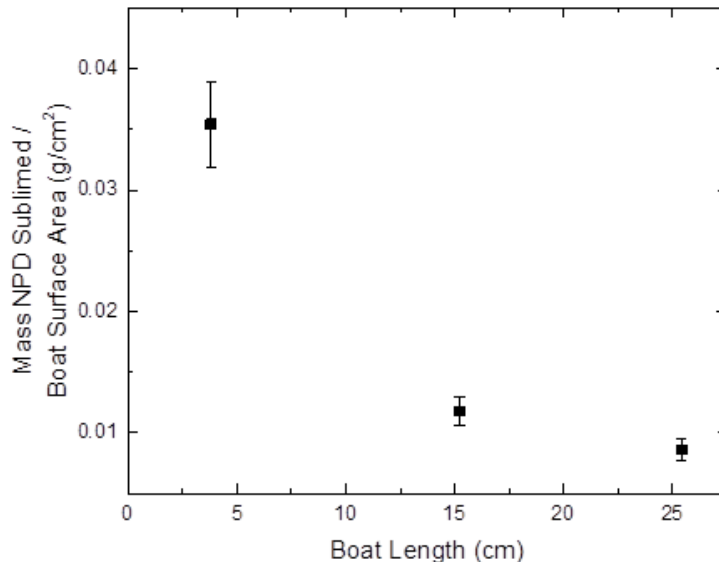


Figure 3.6: Mass sublimed divided by boat surface area is not constant. Mass sublimed is not linear as a function of boat surface area.

rate. However, if diffusion through an ash layer or mass transfer away from the sample boat are limiting, the sublimation rate should depend linearly on the boat surface area. That is, the mass sublimed divided by the boat surface area should be constant.

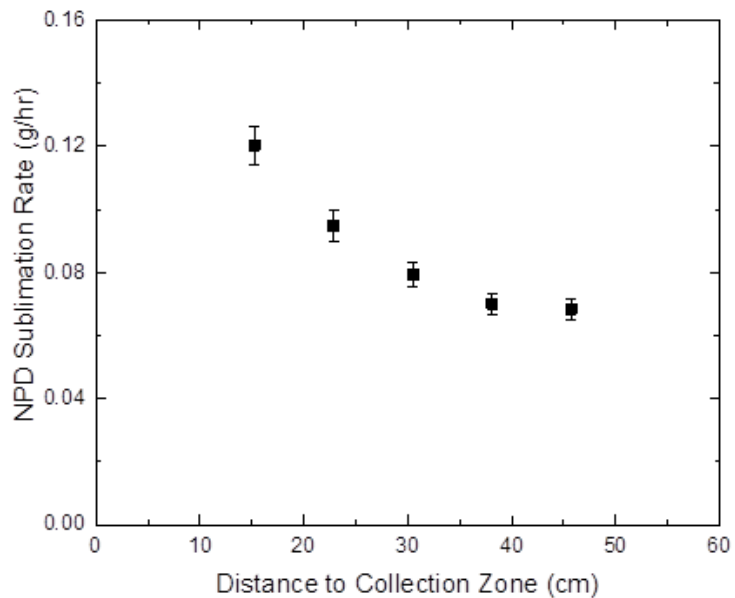


Figure 3.7: NPD sublimation rate decreases as the distance to the collection zone or the transport length increases.

To ascertain whether these

mechanisms are rate-limiting, the sublimation rate was measured as a function of boat area. As shown in Figure 3.6, although the sublimation rate depends on boat surface area, it is clearly not a linear relationship. This dependence is actually an artifact due to minor differences in experimental geometry. Since the boats are always placed at the extreme of the hot end of the collection tube, the center of the largest boat is implicitly placed closer to the cold end than the center of the smallest boat. Thus vapor sublimed from the bigger boat travels a shorter distance to reach the collection zone. This causes the systematic difference shown in Figure 3.3 and is explored in more detail in the following section.

3.2.5. Sublimation Rate as a Function of Transport Length

To examine the effect of transport length more directly, NPD sublimation rates were measured for the 3.8 cm boat placed at different distances from the collection zone. The

results, shown in Figure 3.7, show that larger sublimation rates occur at smaller distances. This

dependence on transport length is predicted by all cases where vapor transport is limiting except for ballistic transport. However, reducing the distance sublimated by a factor of two increases the sublimation rate by only a factor of 1.4, less than the factor of two predicted. Interestingly, when the inverse of the sublimation rate is plotted as a function of transport length, a linear dependence is observed, as predicted by a vapor transport limited process. After correcting for differences in vapor pressure, this is observed for both NPD and TCTA as shown in Figure 3.8. Although the linear dependence is predicted by vapor transport, the non-zero intercept suggests that there is an additional rate-limiting step. This additional resistance has been linked to the deposition process and is discussed in more detail in Chapter 4.

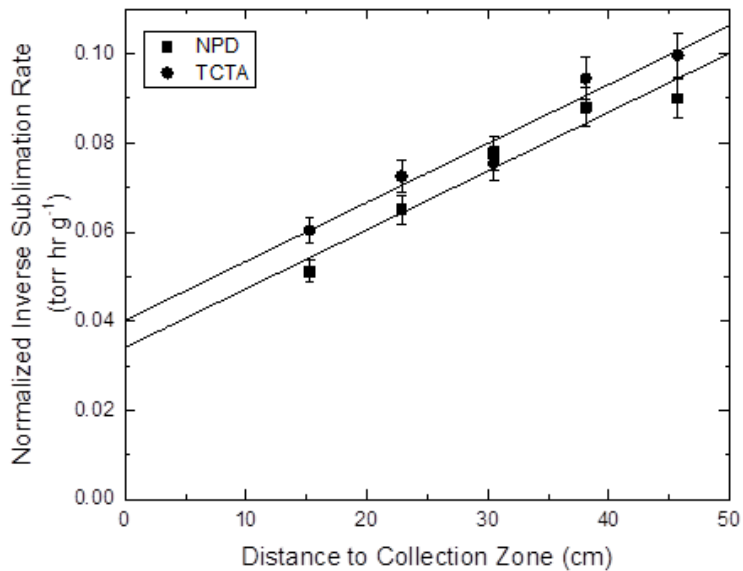


Figure 3.8: The sublimation rate is inversely proportional to the transport length for both NPD and TCTA, suggesting that vapor transport is limiting. The non-zero intercept is attributed to vapor deposition, as discussed in Chapter 4.

3.2.6. Sublimation Rate as a Function of Tube Diameter

While suggestive of a vapor transport limited process, the dependence on transport length is not conclusive evidence. The results for sublimation with

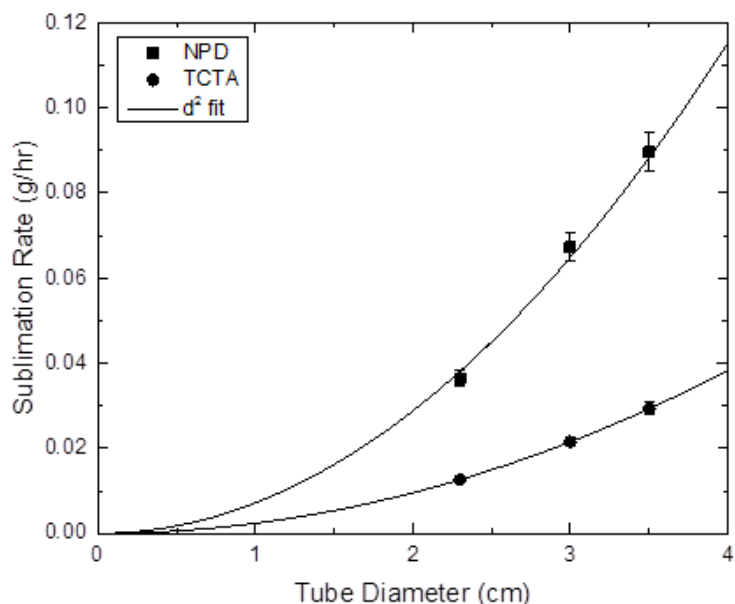


Figure 3.9: The sublimation rate is proportional to the tube diameter squared for both NPD and TCTA.

different collection tube diameters, shown for NPD and TCTA in Figure 3.9, are much more definitive. They indicate that the sublimation rate varies with the square of the collection tube diameter. This is consistent with a dependence on the cross sectional area of the tube, as discussed in Section 3.1.6. Together with the transport length experiment, this is strong evidence that thermal gradient sublimation is limited by vapor phase transport.

3.3. Rate-Limiting Mechanisms in Thermal Gradient Sublimation

While the results clearly show that mass transfer down the tube is the rate-limiting step for sublimation, the exact mechanism is less clear, as discussed in more detail in Chapter 4. Regardless of the vapor transport mechanism, this set of experiments provides some important insights into the thermal gradient sublimation of organic semiconductors. First, unlike many inorganic materials and covalently bonded organic crystals,

sublimation is not controlled by the solid phase.⁵³⁻⁵⁶ Instead, a saturated organic vapor exists above the sample boat, and the process is limited by vapor transport down the length of the tube followed by deposition. This is contrary to previous intuition within the field and may be partially explained by the weak van der Waals bonding observed within organic semiconductors. This theory is discussed in more detail in Chapter 7.

Additionally, because vapor transport and deposition is limiting the process, several simple conclusions regarding scale-up can be made. First, the driving force for vapor transport is the vapor pressure of the organic material. Since vapor pressure increases strongly with temperature, operating at elevated temperature should increase the sublimation rate. Additionally, the rate should increase with the size of the sublimation tube, and will decrease with increasing transport distance. These conclusions will be discussed in more detail in Chapter 4.

4. Vapor Phase Transport and Separation in Thermal Gradient Sublimation

In the previous chapter, we systematically investigated whether solid phase transport mechanisms or the solid-vapor phase transition controlled the purification process. In the case where these mechanisms are rate-limiting, the sublimation rate depends on the particle size, total particle surface area, or boat surface area. We found that the sublimation rate is independent of the particle size, total particle surface area, and boat surface area. Furthermore, the sublimation rate was found to be constant as a function of process time, which would not be the case if the process were limited by the formation of a char layer. These observations suggest that processes within the source boat, including the solid-vapor phase transition, are not limiting. Instead, the sublimation rate was found to depend only on vapor phase transport and deposition. A schematic of this process is shown in Figure 4.1.

This chapter develops a complete theory for the vapor phase transport and deposition process, which can be used to guide experimental design and scale-up. First, potential vapor transport mechanisms are described in Section 4.1 and then compared to

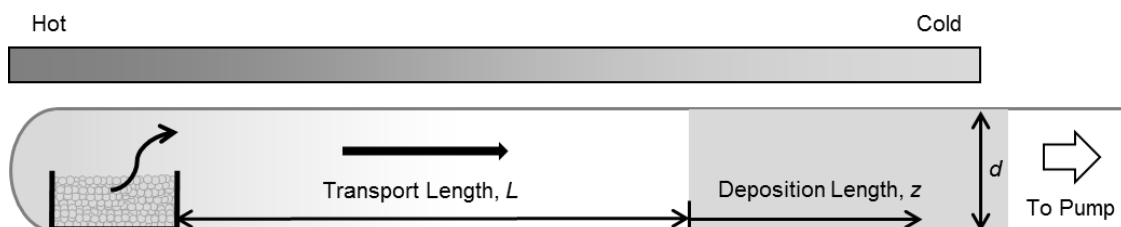


Figure 4.1: Schematic of a vapor transport and deposition limited thermal gradient sublimation process.

experimental observations in Section 4.2 to determine the dominant transport mechanism. Using that mechanism, a complete model for transport and deposition is proposed in Section 4.3. Sections 4.4 and 4.5 employ the proposed model to suggest improvements to separation and process scale-up, respectively.

4.1. Theoretical Mechanisms for Low Pressure Vapor Transport

Low pressure vapor transport can occur via several different mechanisms dictated by the system geometry and the experimental conditions, most notably the operating pressure. The five mechanisms relevant to thermal gradient sublimation are ballistic transport, Knudsen diffusion, diffusion, laminar flow, and slip flow. In order to differentiate between these mechanisms, simple expressions are developed for each case and then compared with experiment to determine the applicable conditions for each mechanism.

In order to determine the exact mechanism for mass transport down the tube, it is important to note that the total mass sublimed per unit time is constant between the sample boat and the start of the collection zone. The mass flux, which is a product of the concentration c_I and the velocity v_I , is also constant. In each case, the mass flux multiplied by the cross sectional area of the tube yields the sublimation rate.

4.1.1. Ballistic Transport

Ballistic transport represents the simplest expression for the movement of vapor within a tube. In this case, each molecule moves down the tube without interacting with other molecules or the tube wall. Because vapor transport is rate-limiting, the concentration above the boat is assumed equal to the saturation concentration of organic

vapor c_1 . Assuming no other interactions are present, the velocity v_1 is simply the molecular velocity u according to kinetic theory.⁵⁷ The flux is simply

$$j_1 = c_1 u = c_1 \sqrt{\frac{8k_B T}{\pi m}} \quad (4.1)$$

where k_B is Boltzmann's constant, T is the temperature, and m is the molecular mass. The sublimation rate is then

$$\dot{m} = j_1 A = c_1 \sqrt{\frac{8k_B T}{\pi m}} \left(\frac{\pi d^2}{4} \right) \quad (4.2)$$

where \dot{m} is the sublimation rate, A is the cross sectional area of the tube, and d is the tube diameter. In this case, the sublimation rate is proportional to d^2 and independent of the transport length L . This first mechanism represents an important limiting case for vapor phase transport.

4.1.2. Knudsen Diffusion and Diffusion

Diffusion is characterized by random molecular motion producing a net flux of material due to a concentration or pressure gradient. For a single, almost pure component vapor at low pressure, which is the case in the majority of thermal gradient sublimation systems, a diffusion-like behavior is observed even though the physical process may be better described as a type of self-diffusion or the free expansion of a molecular gas.⁵⁸⁻⁶⁰ In order to maintain a simple theory, this diffusion-like behavior will be modeled using standard diffusion equations, and then specialized to specific cases.

Fick's law provides a simple equation for the flux of a steady-state diffusive process. At low pressures, the diffusion coefficient D can be estimated using kinetic theory developed for hard spheres.⁵⁷ While this approximation represents a significant

approximation for structurally complex organic semiconductors, it offers a straightforward starting point. Combining the kinetic theory expression for D with Fick's law provides a simple expression for the flux due to diffusion j_D down the tube:^{57,61}

$$j_D = D \frac{(c_{10}-c_{1L})}{L} = \frac{ul}{3} \frac{(c_{10}-c_{1L})}{L} = \sqrt{\frac{8k_B T}{\pi m}} \frac{l}{3} \frac{(c_{10}-c_{1L})}{L} \quad (4.3)$$

where c_{10} is the vapor concentration of the target material above the sample boat, c_{1L} is the concentration at the start of deposition, L is the distance between the boat and deposition, also called the “transport length”, and l is the characteristic distance between collisions.

There are two types of collisions possible within the system, collisions with the tube wall and intermolecular collisions. At low pressures, collisions with the wall are more prevalent and l equals the tube diameter, d .^{57,61} This mechanism is known as Knudsen diffusion.³⁹ In this case, the flux due to diffusion is

$$j_D = \sqrt{\frac{8k_B T}{\pi m}} \frac{d}{3} \frac{(c_{10}-c_{1L})}{L} \quad (4.4)$$

and the sublimation rate is

$$\dot{m} = \sqrt{\frac{2\pi k_B T}{m}} \frac{d^3}{6} \frac{(c_{10}-c_{1L})}{L} \quad (4.5)$$

This yields a sublimation rate that is proportional to d^3 and inversely proportional to the transport length.

As the pressure increases, intermolecular collisions dominate and l from Equation 4.3 becomes the distance between collisions, or the mean free path λ .⁵⁷ The flux for this third mechanism is simply

$$j_D = \frac{\sqrt{\frac{8k_B T}{\pi m}} \lambda}{3} \frac{(c_{10} - c_{1L})}{L} = \frac{2}{3} \frac{(k_B T)^{\frac{3}{2}}}{\sigma^2 \pi^{\frac{3}{2}} P \sqrt{m}} \frac{(c_{10} - c_{1L})}{L} \quad (4.4)$$

where σ is the collision diameter and P is the total pressure. The sublimation rate is

$$\dot{m} = \frac{1}{6} \frac{d^2 (k_B T)^{\frac{3}{2}} (c_{10} - c_{1L})}{\sigma^2 P \sqrt{\pi m} L} \quad (4.5)$$

This yields a sublimation rate that is proportional to d^2 and inversely proportional to the transport length.

In general, these two diffusive mechanisms can occur together, with a mixture of intermolecular and wall collisions. This can be addressed by taking the collision distance as some average of the tube diameter and mean free path. The average is harmonic, because the smaller of the mean free path and the tube diameter will be the more important. This type of analysis is typically avoided by determining the dominant transport mechanism by comparing the relative length scales between the two collision mechanisms. This produces a dimensionless number, $Kn = \lambda/d$, known as the Knudsen number.³⁹ For large Knudsen numbers, Knudsen diffusion is dominant and at small Knudsen numbers, intermolecular diffusion dominates.

4.1.3. Viscous Flow

Flow through a pipe is a well-studied phenomenon characterized by the relative amount of inertial to viscous forces within the flow, the ratio of which is the Reynolds number (Re). When Re is small as in the low pressure vapor flows studied here, viscous forces dominate and the flow is laminar. Since the fluid is Newtonian, the general Navier-Stokes equations give to a good approximation, even for compressible flow, the flux due to flow j_F :^{61,62}

$$j_F = \frac{c_1 d^2 \Delta P}{32\mu L} = \left[\frac{P d^2}{32\mu} \right] \frac{\Delta c_1}{L} \quad (4.6)$$

where c_1 is the average concentration of the vapor phase, ΔP is the pressure drop from the sample boat to the start of deposition, and μ is the viscosity. Estimating the viscosity using the kinetic theory of hard spheres allows for the flux due to flow at low pressure to be expressed as:⁶¹

$$j_F = \left[\frac{P d^2}{32\mu} \right] \frac{\Delta c_1}{L} = \left[\frac{3 P d^2 \sigma^2 \pi^{3/2}}{64 \sqrt{m k_B T}} \right] \frac{(c_{10} - c_{1L})}{L} \quad (4.7)$$

where P is the average pressure in the transport region. This equation implicitly assumes that the pressure and concentration drop linearly over the transport length and that the density remains constant, an assumption justified in earlier studies.⁶²

If flow controls transport, the sublimation rate is the fourth mechanism considered here:

$$\dot{m} = \left[\frac{3 P d^4 \sigma^2 \pi^{5/2}}{256 \sqrt{m k_B T}} \right] \frac{(c_{10} - c_{1L})}{L} \quad (4.8)$$

This yields a sublimation rate that is proportional to d^4 and inversely proportional to L .

4.1.4. Slip Flow

Slip flow is a variation of traditional laminar flow often used to treat low pressure vapor flows where the vapor velocity at the tube wall is non-zero.^{63,64} Mathematically, this results in a relaxation of the standard no-slip boundary condition at the tube wall. Equation 4.6 then becomes⁶⁵

$$j_S = \left(\frac{d^2}{32\mu} + \frac{d}{4\beta} \right) P \frac{\Delta c_1}{L} \quad (4.9)$$

where β is the slip friction coefficient. This equation results in an overall flux that is higher than the standard viscous flow case, and which is inversely proportional to the

transport length L . The dependence on the tube diameter is between d^3 and d^4 , depending on how significant the slip is.

The slip friction coefficient can be estimated using kinetic theory such that Equation 4.9 becomes

$$j_s = \left(\frac{3d^2 \sigma^2 \pi^{3/2}}{64\sqrt{mk_B T}} + \frac{d(2-\xi)}{4P\xi} \sqrt{\frac{\pi k_B T}{2m}} \right) P \frac{(c_{10} - c_{1L})}{L} \quad (4.10)$$

where ξ is the coefficient of diffuse reflection or the fraction of molecule-wall collisions that are diffuse. This analysis predicts that as pressure decreases, the contribution due to slip flow will increase, dominating the flux.

4.2. Experimental Evidence Supporting Diffusion

In order to test the theory developed in Section 4.1 experimentally, the sublimation rate was measured as a function the diameter of the purification tube and of the length between the sample boat and deposition region. Conveniently, each vapor transport mechanism presented above has a unique dependence on experimental geometry, summarized in Table 4.1. For all mechanisms except ballistic transport, the sublimation rate is expected to decrease as a function of the transport length L . The

dependence on
the tube
diameter is
expected to be d^2
for ballistic
transport or

Table 4.1: Geometric dependences of potential rate-limiting vapor transport mechanisms.

Vapor Transport Mechanism	Geometric Dependence
1. Ballistic Transport	d^2
2. Knudsen Diffusion	d^3/L
3. Diffusion	d^2/L
4. Viscous Flow	d^4/L
5. Slip Flow	$d^3/L \leq x \leq d^4/L$

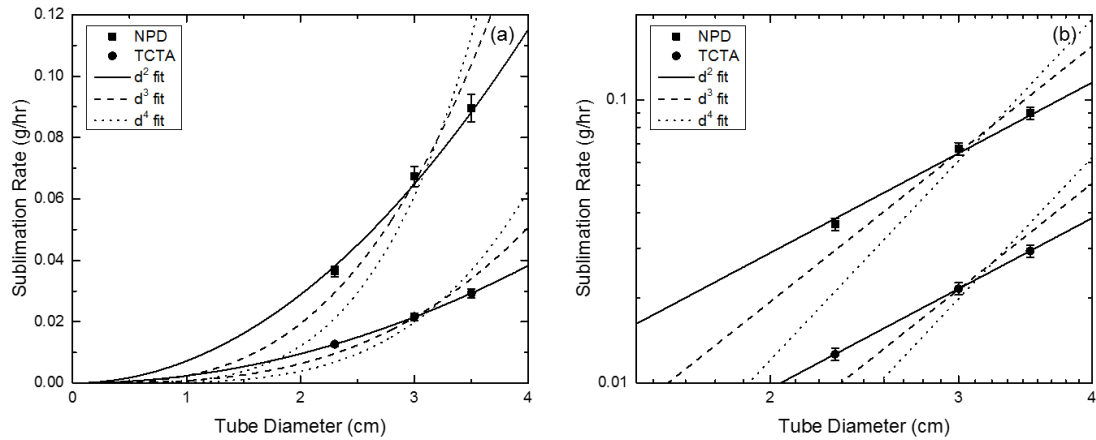


Figure 4.2: Dependence of sublimation rate on tube diameter. (a) The sublimation rate is proportional to d^2 for both NPD and TCTA, indicating that the dominant transport mechanism is diffusion. (b) The same data shown on a logarithmic scale.

diffusion, d^3 for Knudsen diffusion, d^4 for viscous flow, and between d^3 and d^4 for slip flow, depending on the degree of slip.

In our work, the sublimation rate varies with the square of the tube diameter for both materials studied, as shown in Figure 4.2. The theory presented in Section 4.1

predicts that the sublimation rate varies with d^2 if diffusion or ballistic transport is the dominant rate-limiting mechanism. Other mechanisms, like Knudsen diffusion and viscous or slip flow, predict variations with

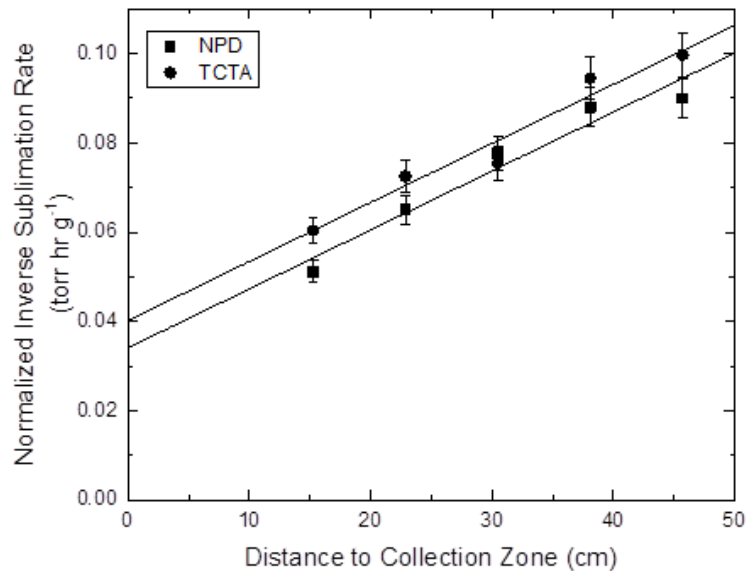


Figure 4.3: The sublimation rate is inversely proportional to the transport length for both NPD and TCTA, consistent with diffusion or flow. The non-zero intercept is attributed to vapor deposition.

tube diameter to the third or fourth power, respectively. In addition, as shown in Figure 4.3, the reciprocal of sublimation rate varies linearly with transport length, i.e. with the distance L from the source boat to the onset of deposition. This agrees with the dependence expected for diffusion or flow, but not for ballistic transport.

The non-zero intercept in Figure 4.3 appears to show that an additional resistance is present, namely a resistance due to molecular deposition on the tube wall. Section 4.3 develops a complete theory including resistances of transport and of deposition, taking intermolecular diffusion to be the dominant vapor transport mechanism.

4.3. Diffusion-Based Transport and Deposition Model

As material travels down the length of the tube, it begins to deposit on the cold tube wall when its pressure exceeds its vapor pressure. This deposition is not instantaneous so that the pressure does not immediately drop to zero once the vapor reaches the deposition zone. This provides an additional resistance to vapor transport that is not captured in Equations 4.4 and 4.5. To account for this, this section develops a diffusive model that treats deposition as a simple first order reaction at the tube wall. While simplistic, this provides a model that provides a reasonable model for experimental results as shown in Section 4.3.3.

4.3.1. Diffusion Theory

Vapor transport from the sample boat to the deposition region can be simply described by Equations 4.4 and 4.5. Once deposition begins, an additional term must be included in the transport equation to account for the loss of material to the tube wall. This can be modeled using straightforward reaction-diffusion equations, assuming that

once the saturation vapor pressure at the wall is reached, all material in the tube can potentially be removed by condensation. A mass balance on a cross section of tube after the onset of deposition yields

$$0 = D \frac{d^2 c_1}{dz^2} - \frac{4k c_1}{d} \quad (4.11)$$

$$z = 0, c_1 = c_{1L} \quad (4.12)$$

$$z = \infty, c_1 = 0 \quad (4.13)$$

where z describes the distance down the tube from the onset of deposition or the deposition length, as shown in Figure 4.1. The parameter k describes the rate at which the target molecule is deposited on the tube wall. The ratio of tube surface area to volume yields the $4/d$ term.²⁰ The first boundary condition in Equation 4.12 results from continuity with Equation 4.4, and the second boundary condition assumes that in the limit of a long tube, the concentration of target material in the vapor phase approaches zero at the end of the tube. This is a good assumption because the pressure near the pump is several orders of magnitude lower than the saturation vapor pressure of the target molecules, and a mass balance of the product collected shows low loss even with short tube lengths.

Integrating Equation 4.11 and applying the boundary conditions in Equations 4.12 and 4.13 yields an equation for the concentration of target material in the vapor phase as a function of deposition length z

$$c_1(z) = c_{1L} \exp\left(-\sqrt{\frac{4k}{Dd}} z\right) \quad (4.14)$$

This equation predicts an exponential decay in the target vapor concentration as a function of the deposition length. The mass of target material deposited on the tube wall at any given point is simply proportional to the concentration of the target material in the vapor phase, yielding an exponential decay in the mass deposited in time t with the deposition length z according to the mass balance

$$\frac{dm}{dz} = \pi dktc_1(z) = \pi dktc_{1L} \exp\left(-\sqrt{\frac{4k}{Dd}}z\right) \quad (4.15)$$

Equation 4.15 can be integrated to calculate the deposition rate of the target compound over any given section of the deposition region.

In order to calculate the total flux within the system, Equations 4.4 and 4.14 can be combined by assuming that the concentration is continuous at the onset of deposition, even though the concentration gradient is discontinuous. This provides a value for the concentration at the onset of deposition c_{1L} :

$$c_{1L} = \frac{c_{10}}{1+L\sqrt{\frac{4k}{Dd}}} \quad (4.16)$$

and the total flux j_1 :

$$j_1 = \frac{Dc_{10}}{L} \left(1 - \frac{1}{1+L\sqrt{\frac{4k}{Dd}}}\right) \quad (4.17)$$

Thus transport from the boat to the deposition region and the deposition process itself both add a resistance to the rate of sublimation. The relative impact of these two processes be determined by dividing the total flux in Equation 4.17 by the concentration above the boat and then taking the inverse of the flux

$$\frac{c_{10}}{j} = \frac{1}{D}L + \sqrt{\frac{d}{4kD}} \quad (4.18)$$

The relative magnitude of these two resistances can be determined by plotting Equation 4.18 versus transport length L . The y-intercept shows the effect of deposition and the slope shows the effect of transport. This explains the origin of the non-zero intercept in Figure 4.3. This and other experimental results are discussed in the following two sections.

While this analysis is successful, as discussed below, a more accurate expression for Equation 4.11 might be that deposition is proportional to $k(c_1 - c_1^*)$, where c_1^* is the saturation vapor pressure at the local temperature of the tube wall. This in turn is a function of axial position z , given by the applied temperature gradient and the measured vapor pressure as a function of temperature, as described in Chapter 2. Assuming that the temperature of the tube wall varies linearly in the deposition region, and that the vapor pressure increases exponentially as a function of temperature provides a function for the saturation vapor pressure c_1^*

$$c_1^* = \frac{P}{RT} = \frac{\exp(\gamma(\alpha z + \beta) + \delta)}{R(\alpha z + \beta)} \quad (4.19)$$

Where α and β are the slope and intercept of the temperature profile, respectively, and γ and δ are the fit parameters for the vapor pressure from Chapter 2. Inserting Equation 4.19 into Equation 4.11 provides a more complete analysis than the previous one:

$$0 = D \frac{d^2 c_1}{dz^2} - \frac{4k \left(c_1 - \frac{\exp(\gamma(\alpha z + \beta) + \delta)}{R(\alpha z + \beta)} \right)}{d} \quad (4.20)$$

Analytical evaluation of this differential equation is possible, but yields a significantly more complex exponential decay than that shown in Equation 4.14 and is better handled

numerically. This increased complexity is unnecessary, as demonstrated by the quality of predictions using the simple model in the section below.

4.3.2. Predicted Deposition Profile

The theoretical developments above provide a variety of predictions that can be checked experimentally. Those of interest here center on the amount of solid collected as a function of axial position z . We want to compare these predictions against our experimental measurements of the amount collected. To begin, we look at the simplest case of collection controlled by mass transfer in the bulk, summarized by Equation 4.11, and centering on the rate constant k .

To investigate this particular deposition mechanism, the mass deposited on the tube wall was measured as a function of the distance from the onset of deposition. The results for a single component feed, presented for NPD in Figure 4.4a, show an initial rise in the mass deposited followed by an exponential decay. The rise is too fast to be

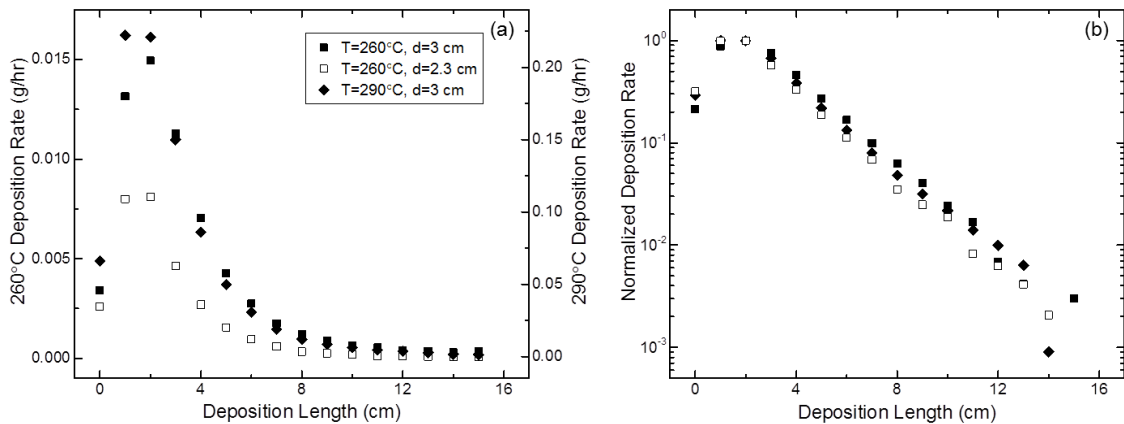


Figure 4.4: (a) The NPD deposition rate exponentially decays as a function of deposition length for a variety of process conditions. Note the different scale for 290 °C deposition. The onset is not perfectly sharp because the mass was measured in 1 cm increments. (b) The normalized mass of NPD deposited shows the same exponential decay for the variety of experimental conditions.

accurately measured with the current sampling technique, which collects samples every centimeter. The slope of the exponential decay, obtained from the semi-logarithmic plot of mass vs. position shown in Figure 4.4b, is a measure of both of transport down the tube and of vapor deposition on the wall as predicted by Equation 4.15. Although alternate transport models may yield an exponential decay profile, this apparent prediction of the experimental results strongly supports the proposed diffusive transport model.

In order to model the deposition profile, a lumped parameter reaction-diffusion model was used where transport was limited to diffusion down the length of the tube and a simple first order reaction at the surface was used to describe the deposition on the tube wall. The rate constant k , or deposition coefficient, presented in Equation 4.11 describes the ability of the target molecule to deposit on the tube wall. The deposition coefficient, which has units of velocity, includes two physical phenomena: it describes the resistance to the integration of a vapor molecule into the crystal surface, and it represents a transport resistance from the bulk vapor to the tube wall. In the case of integration, k may be molecule dependent. If mass transport limits deposition, k is a mass transfer coefficient which can be estimated from literature correlations as D/l where l is a characteristic transport length such as a boundary layer thickness.²⁰

We can evaluate the mass transfer case more completely than the integration case. Substituting this correlation into the exponential in Equation 4.15 cancels the diffusion coefficient and allows for a straightforward measurement of the characteristic transport length by fitting the exponential deposition profile. Normalizing and fitting the

experimental data in Figure 4.4 in this way yields a boundary layer thickness of 8 cm for NPD, which has no clear physical basis. A similar analysis for TCTA yields a boundary layer thickness of 6 cm, also clearly unphysical. This suggests that the deposition coefficient is not dominated by mass transport in the vapor phase, but instead is related to surface integration. However, because no other estimate for surface integration is available, this cannot be confirmed.

4.3.3. Sublimation Rate Predictions

Using the deposition coefficient obtained from experiment, Equation 4.18 can be used to predict the relative impact of transport and deposition on the sublimation rate.

Dividing the data in Figure 4.3 by the cross sectional area of the tube yields the inverse velocity for vapor transport as a function of transport length, as shown in Figure 4.5. The slope and intercept in Figure 4.5 are the same as those predicted by Equation 4.18. The results of this prediction are compared

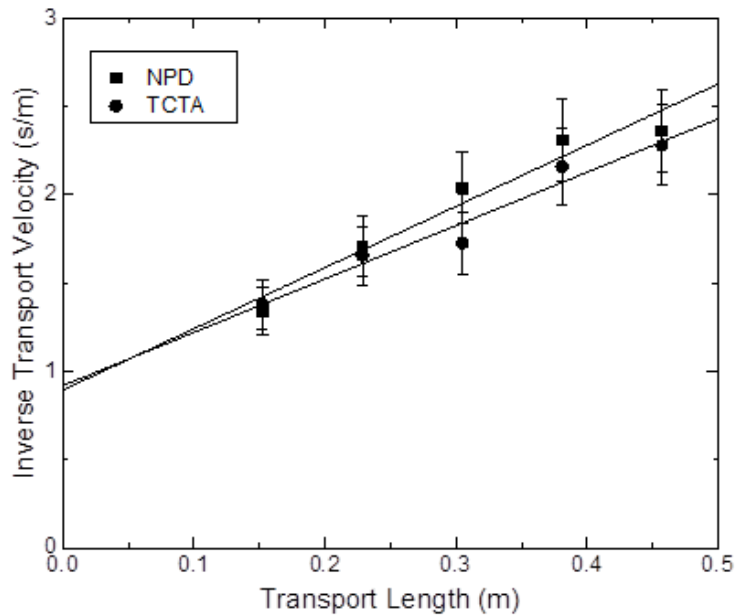


Figure 4.5: Dependence of the inverse transport velocity on transport length, allowing the separation of resistances due to transport and deposition. As the transport length approaches zero, the vertical-intercept results from resistance due to deposition. The non-zero intercept and positive slope show that both transport and deposition are important in the sublimation process.

to the experimental values in Table 4.2. The slopes in Equation 4.18, calculated using the kinetic theory of hard spheres as described in

Table 4.2: Experimental and predicted values for the slope and intercept in Equation 4.18. The slope gives an indication of the impact of transport down the tube on sublimation rate. The intercept gives an indication of the impact of deposition.

Material	Slope (s/m ²)		Intercept (s/m)	
	Calc.	Exp.	Calc.	Exp.
NPD	9	3.5±0.5	0.2	0.9±0.2
TCTA	3	3.0±0.4	0.06	0.9±0.1

Section 4.1, agree within a factor of three of the experimental values. The pressure was assumed to be the vapor pressure of the target material at the boat temperature, and the collision diameter was estimated to be 1 nm for both NPD and TCTA by assuming a spherical shape with a volume equal to the Connolly solvent excluded volume as calculated by ChemBio3D Ultra 13.0.^{66,67} The intercept in Eqn. 4.18 was estimated using the experimental deposition coefficient and the diffusion coefficient calculated from kinetic theory. The predictions are about an order of magnitude smaller than the experimental values, which is opposite the error expected from the assumption of rigid spheres in kinetic theory. While this is significant, it is not surprising due to the simplified theory. The overall sublimation rate can also be calculated by multiplying the flux obtained from Eqn. 4.17 by the cross sectional area of the tube. This yields a calculated sublimation rate of 0.015 g/hr at 260 °C for NPD and 0.005 g/hr at 310 °C for TCTA. These values are both within a factor of four from the experimental values of 0.068 and 0.022 g/hr respectively.

However, the agreement of the experimental data with a diffusion model does not mean that the sublimation mechanism involves intermolecular diffusion or even self-

diffusion. In intermolecular diffusion, there are two solutes;²⁰ here, there is one. In self-diffusion, there is one solute, but a portion of this solute can be separately identified; here, no such identification is possible. Moreover, diffusion is normally measured relative to a reference velocity, most often a volume average velocity. In many experiments, this velocity is zero; here, this velocity is not zero. At the same time, the results here match diffusion equations, as do turbulent dispersion,⁶¹ “collisionless diffusion”,⁶⁰ and Taylor-Aris dispersion.^{68,69} This apparent discrepancy will be discussed in more detail in Chapter 7.

4.4. Separation

When considering how to improve separation, we must consider not only the mechanism, but also the types of impurities present within the starting material. Impurities that have very different properties from the target material are often significantly easier to separate than impurities that are similar to the target. This section considers both cases for thermal gradient sublimation and uses the model developed in Section 4.3 to guide experimental design.

4.4.1. Fundamental Improvements in Purity

In general, impurities that differ significantly in molecular weight from the target material are readily removed. This is due to a large difference between the vapor pressure of the impurity and the target. In this case, the impurities either do not sublime and remain in the source boat, or are so volatile that they do not deposit on the tube wall. Similarly, inorganic materials such as residual catalysts, which have limited vapor pressures, are also easily removed. These separations do not rely on the temperature

gradient, but merely on the act of sublimation itself. While these separations can be accomplished using the thermal gradient sublimation technique, a simpler “cold finger” apparatus should be equally effective.

Although simple, this type of separation is the most commonly encountered type within organic semiconductors. For example, the primary impurities observed during the synthesis of NPD are significantly larger than NPD, as shown in Figure 4.6. The MS data for these impurities are available in Appendix C. These impurities, which account for

approximately 0.8% of the starting material, were readily removed using a single sublimation purification without an optimized temperature gradient, yielding a product >99.9% pure by HPLC. Even in the case of impure (77.5%) starting material, a product with over 99% NPD by HPLC was produced without optimizing the temperature gradient. These results are summarized in Table 4.3. Interestingly, when a feed that is

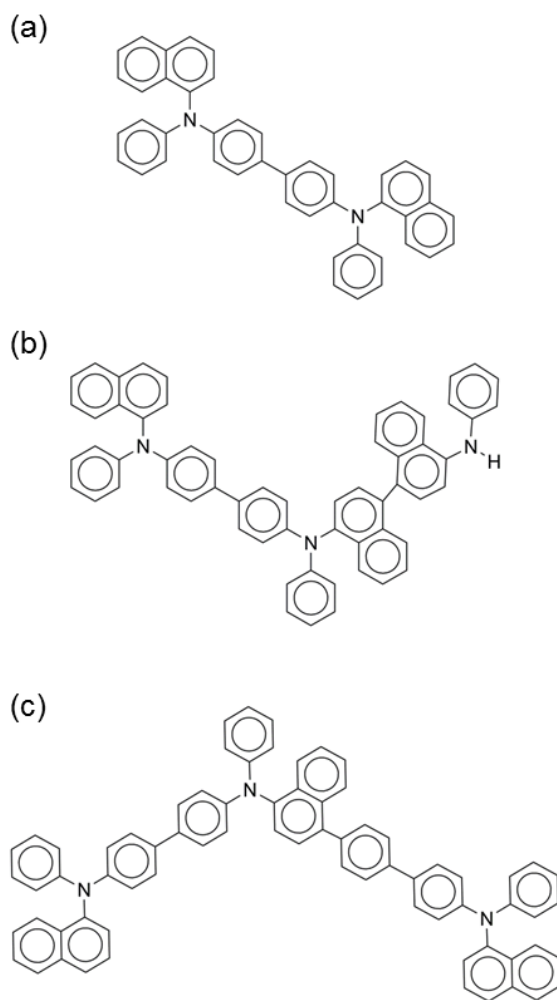


Figure 4.6: (a) Molecular structure for NPD and (b, c) Primary impurities.

77.5% pure NPD is used, the rate is within experimental error of that observed with the purer feed, although the resulting product was less pure.

Table 4.3: Purity of NPD before and after sublimation without a controlled temperature gradient. High purity was achieved even for impure starting material.

Material Source	Initial Purity	After Purification
Sigma-Aldrich	99.3%	99.9%
Dow	99.2%	99.9%
Dow	71%	99.0%

4.4.2. Impact of Temperature Gradient

For impurities that are similar in vapor pressure to the target material, careful control of the temperature gradient is required to achieve good separation. In this case, significant insight can be gained by considering the deposition model developed in Section 4.3. To illustrate this, a 1:1 by wt.% mixture of NPD and TCTA was sublimed. These materials were selected based on their relatively similar vapor pressures, previous experiments examining transport properties, and material availability. In these experiments, shown in Figure 4.7b, the total mass collected was weighed and analyzed as a function of position, so the masses of each component can be shown separately. As in the single component experiments, each of these species shows an abrupt rise and an exponential decay. The exponential decay for NPD sublimed from a mixture has a slope of $(-0.23 \pm 0.02 \text{ cm}^{-1})$, compared with $(-0.21 \pm 0.02 \text{ cm}^{-1})$ for the NPD alone in Figure 4.4b. These two values are within experimental error. Thus, the sublimation of a single component is largely independent of the presence of other components. In other words, the separation is accomplished by spatially separating the independent deposition profiles

of each independent component. These deposition profiles, predicted in Section 4.3, can be used to design the temperature gradient required to achieve a given separation.

In order to demonstrate this result, a shallower temperature gradient was applied to the deposition region in Figure 4.7c. The deposition profiles for

NPD and TCTA are separately visible, with minimal overlap between the two components. The temperature at the onset of deposition and the shape of the deposition profile remain constant. This provides a clear guideline for the separation of multiple components using this technique.

4.5. Scale-Up

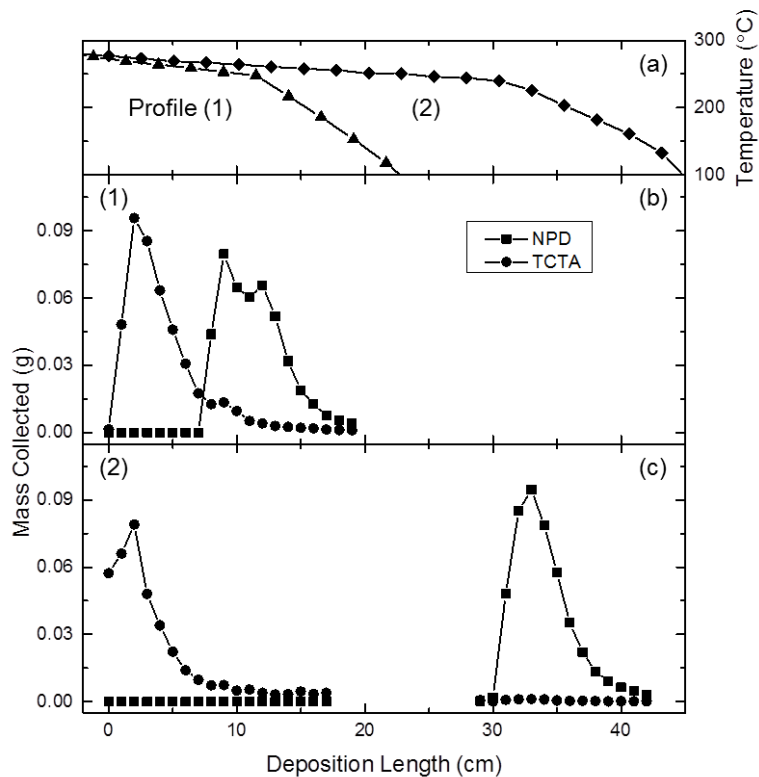


Figure 4.7: (a) Temperature profiles for the purification of NPD-TCTA mixtures. (b) NPD and TCTA deposition profile for a relatively steep temperature profile (1). Both compounds show an exponential decay, but significant overlap was present. (c) NPD and TCTA deposition profile for a relatively shallow temperature profile (2). Two clear exponential decays are present and significant amounts of each pure component were recovered.

As demand increases for organic electronic materials, significant scale-up of existing purification systems is desired. Using the vapor phase transport model, processes for increasing the productivity of small scale sublimation can be considered. This can be done by improving the existing batch process, or by switching to a more continuous operation. Both strategies will be considered.

4.5.1. Diffusion Based Scale-Up

To scale-up the existing process, consider increasing the temperature and the diameter of the collection tube. Increasing the temperature does not significantly increase the molecular velocity, but it exponentially increases the vapor pressure and so the sublimation flux. For example, an increase in temperature from 260 to 290°C increases the vapor pressure of NPD by a factor of ten, making the sublimation ten times more productive. Although it provides a sharply increased vapor pressure, higher temperature does risk degradation of the active material. While degradation was found to be minimal in these experiments, it could be more serious for other compounds and must be evaluated on a case by case basis. Increasing the diameter of the collection tube gives an increase that is proportional to the square of the tube radius. However, the tube diameter should not greatly exceed the tube length, because then larger amounts of impurities may be more difficult to remove. Reducing the tube length will not give large increases in sublimation rate, and will decrease separation flexibility.

In order to test these generalizations, data were obtained from an industrial sublimation unit operated by The Dow Chemical Company. Similar system geometry was used with a comparable organic material at a temperature such that its vapor pressure

was 100 times that of those in this study. The tube diameter was increased from 0.030 m to 0.30 m, so that the area increased by a factor of 100. The length was reduced from 0.46 m to 0.10 m, increasing the rate two times. This suggests an increase in sublimation rate 20,000 times larger than that of the system used for this study, from 0.067 g/hr. to over 1,000 g/hr. This estimate agrees with the data obtained from Dow.

4.5.2. Alternate Transport Regimes at Elevated Pressure

The most direct route to scale-up is to increase the sublimation temperature, and therefore increase the concentration of material traveling down the tube. However, increasing the concentration will not only increase the driving force, but will also increase the number of intermolecular interactions. This has the potential to alter the transport regime, changing the dominant transport mechanism. As shown in Table 4.1, any change in mechanism has significant impacts on process scale-up.

To illustrate the potential transition between transport regimes, we can develop a combined model for vapor transport. First, the harmonic average between the mean free path and the tube diameter can be used as the characteristic length l for diffusion in Equation 4.3. This accounts for both collisions with the wall predicted by Knudsen diffusion and intermolecular collisions predicted by intermolecular diffusion. The overall diffusive flux is

$$j_D = \left[\frac{u}{3} \frac{1}{d + \lambda} \right] \frac{(c_{10} - c_{1L})}{L} = \left[\frac{1}{3} \sqrt{\frac{8k_B T}{\pi m}} \left(\frac{1}{\frac{1}{d} + \frac{\sqrt{2}\pi\sigma^2 P}{k_B T}} \right) \right] \frac{(c_{10} - c_{1L})}{L} \quad (4.21)$$

Because flow and diffusion down the tube occur in parallel during the sublimation process, we assume that they can be added together to obtain the overall flux j :

$$j = j_F + j_D = \left[\frac{3Pd^2\sigma^2\pi^{3/2}}{64\sqrt{mk_B T}} + \frac{1}{3}\sqrt{\frac{8k_B T}{\pi m}} \left(\frac{1}{\frac{1}{d} + \frac{\sqrt{2}\pi\sigma^2 P}{k_B T}} \right) \right] \frac{(c_{10} - c_{1L})}{L} \quad (4.22)$$

This provides a unified expression for the flux down the length of the tube. Dividing the flux by the concentration drop yields

$$\frac{j}{c_{10} - c_{1L}} = \frac{1}{L} \left[\frac{3Pd^2\sigma^2\pi^{3/2}}{64\sqrt{mk_B T}} + \frac{1}{3}\sqrt{\frac{8k_B T}{\pi m}} \frac{1}{\frac{1}{d} + \frac{\sqrt{2}\pi\sigma^2 P}{k_B T}} \right] \quad (4.23)$$

This equation can be used to explore the impact of transport mechanism for any given set of experimental conditions. This is illustrated in Figure 4.8 where values calculated from the left hand side of

Equation 4.23 are plotted as a function of pressure for TCTA. This calculation assumes a tube diameter of 3 cm, a uniform temperature of 310 °C, a transport length of 45 cm, and a collision diameter of 1 nm based on typical experimental conditions. The Matlab program used to conduct this simulation is

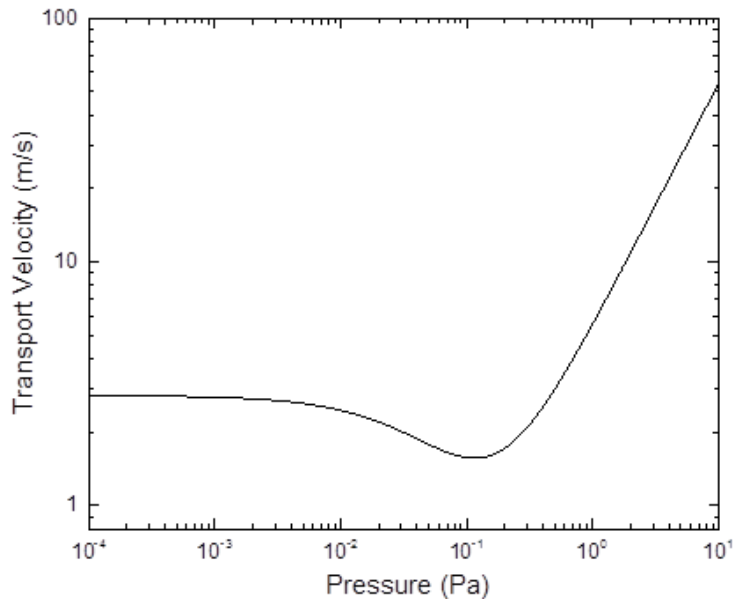


Figure 4.8: Transport velocity calculated as a function of pressure within the sublimation system for TCTA. At low pressure the transport is dominated by Knudsen diffusion and the velocity is independent of pressure. At high pressure the transport is dominated by flow and the velocity is proportional to pressure. At moderate pressure the transport is dominated by intermolecular diffusion and the velocity is inversely proportional to pressure.

available in Appendix D. Figure 4.8 shows that Knudsen diffusion is the dominant mechanism at low pressure, and laminar flow is dominant at high pressure. There is a minimum between the two extremes controlled by diffusion. The saturation vapor pressure of TCTA is 0.05-0.2 Pa for the operating temperatures of 250-310 °C, suggesting that diffusion dominates transport at the experimental conditions present within this work. Calculations for NPD yield similar results. These calculations are consistent with the experimental results shown in Sections 4.2 and 4.3.

Figure 4.8 suggests that increasing the pressure of TCTA only an order of magnitude from 0.1 to 1 Pa could change the dominant regime of transport from diffusion to flow. Under current conditions where diffusion dominates transport, the transport velocity is inversely proportional to the pressure and the sublimation rate is proportional to the tube diameter squared. However, if the pressure is increased by one order of magnitude such that laminar flow is the dominant mechanism, the transport velocity would increase with pressure and the sublimation rate would become proportional to d^4 . If this happens, a significant increase in sublimation rate would occur with only a small change in temperature. While some materials may show thermal instability, the significantly increased rate of production could merit losses from this instability. This tradeoff will be discussed in more detail in Chapter 7.

4.5.3. Continuous Processing

These experiments also suggest ways in which sublimation can be operated more continuously. The obvious way is to pump an inert carrier gas, such as nitrogen or argon, at higher pressures through a packed bed of small particles of the active material to

produce a vapor which is at least 30% saturated. This vapor is then cooled to form purified crystals. Such a process can easily use a convective velocity of 10 m/sec or greater, and so has the potential to have a rate of over a factor of ten greater than the batch processes described in this paper. Such a process is sometimes called “entrainer sublimation²¹” and is often used to grow large single crystals of organic molecules.⁵⁰ Reaching this potential will hinge on carefully designing the zone of the sublimator where the crystals are collected. Because the vapor is moving rapidly and may have slower mass transfer than in the low pressure gas used currently, this zone should be longer and probably offer more surface area.^{25,26} At the same time, it should still allow the crystals to be harvested easily. This may be difficult to achieve and may be less attractive than more conventional, large batch operations.

4.6. Model Scope and Conclusions

This work develops a simple theory that can be used to predict the transport behavior of organic electronic materials during purification by thermal gradient sublimation. While this theory shows qualitative agreement with the experimental results, it makes significant approximations in order to retain the simplicity of the model. The dominant transport mechanism under the conditions studied appears to be a form of diffusion. The experiments show a sublimation rate proportional to the tube diameter squared, inversely proportional to the distance from the source boat to the deposition region, and an exponentially decaying deposition profile. The deposition parameter likely reflects the integration of a vapor molecule at the crystal surface. These results and provide insight for improved separation and process scale up.

5. The Effect of Rapid Pressurization on the Solubility of Small Organic Molecules

The previous two chapters developed and validated a transport model for the thermal gradient purification of organic semiconductors. That work was motivated by the recent increase in demand for organic semiconducting materials. This chapter and the following one discuss crystallization, an essential process in the manufacture of pharmaceuticals, agrochemicals, and other specialty chemicals. These chapters introduce a novel crystallization technique, pressure-swing crystallization. In this technique, rapid changes in pressure, up to 10,000 psig, are used to control the solubility of small organic molecules in solution. This chapter develops the underlying thermodynamic theory which predicts the magnitude and direction of the change in solubility during these pressure swings. Chapter 6 describes potential applications for the technique.

Changes in solubility upon pressurization arise from two competing processes, heating due to adiabatic compression and altered solubility with pressure. These two effects, which often have opposite impacts on solubility, are frequently ignored at small scale and are not discussed in modern texts.^{21,70} These two effects, measured using the experimental equipment described in Chapter 2, are justified with simple theoretical models. Although developed here for pressure-swing crystallization, this model is also applicable to the broader high pressure crystallization field.⁷¹⁻⁷⁶

5.1. Temperature Changes Due to Pressurization

The adiabatic compression of a gas results in an increase of the gas temperature, but the effect is not often studied in liquids. Previous work has shown that this effect is typically small but measurable due to the comparatively incompressible nature of liquids under moderate pressure.^{77,78} At the high pressures employed during pressure-swing crystallization, the temperature increase due to compression becomes significant. In fact, this phenomena is often observed during the high pressure processing of food.^{79,80} During crystallization, adiabatic heating due to compression is especially important because even a small increase in solution temperature can lead to a dramatic increase in solubility.

5.1.1. Experimental Temperature Changes Due to Pressurization

To accurately measure this effect, a variety of pure solvents was compressed rapidly (<15 seconds) from 0-10,000 psig (689.5 barg). The temperature increase was measured as a function of pressure, as shown for methanol in Figure 5.1a. Depressurization experiments match the pressurization experiments within 0.2°C/10,000 psig, demonstrating reversibility outside of the heat transfer losses discussed below. Additionally, minimal changes in this effect were observed when the small concentration of solutes used for nucleation experiments was added to the pure solvent. Interestingly, the temperature increase is not linear with pressure, slowing at higher pressure for all of the solvents studied. This nonlinearity is attributed to two effects: heat transfer from the solvent to the reactor walls, and changes in the material properties as a function of pressure. The role of heat transfer was probed by rapidly increasing the solution temperature via pressurization and recording the temperature as a function of time while

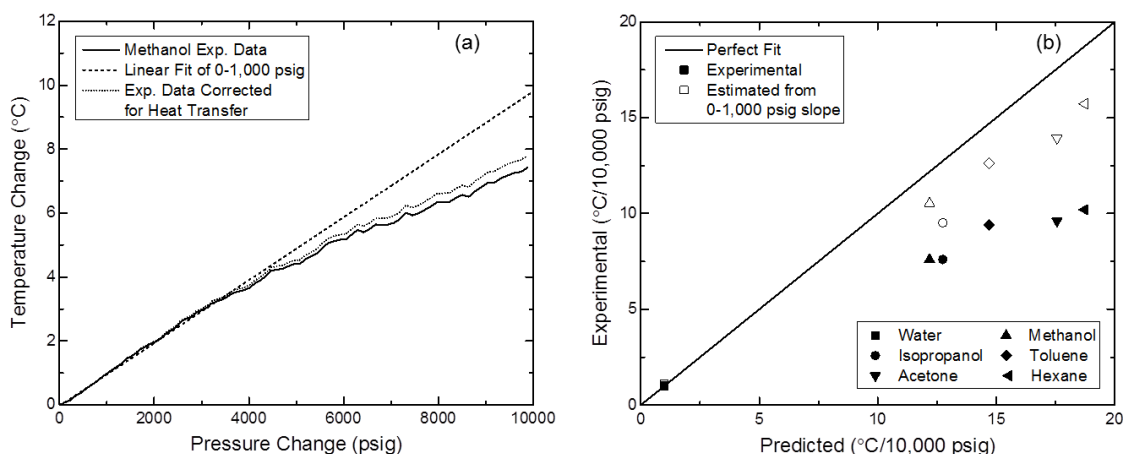


Figure 5.1: (a) Change in temperature as a function of pressure for methanol. The change in temperature is nonlinear due to heat transfer and changes in material properties with increased pressure. (b) The experimental increase in temperature upon compression to 10,000 psig compared to predictions from Equation 5.1 for a variety of solvents. Equation 5.1 overestimates the temperature due to heat transfer and varying material properties.

the solution cooled. Fitting these data assuming that the reactor wall acted as an infinite sink⁸¹ yields an overall heat transfer coefficient of $0.01 \text{ J cm}^2 \text{ K}^{-1}$ and allows the pressurization data to be corrected assuming that the process was adiabatic, as shown in Figure 5.1a for methanol. From this analysis, heat transfer is only responsible for about 20% of the curvature, with the remainder due to changes in material properties as a function of pressure. This result agrees with previous work.⁷⁸ Figure 5.1b shows this result for a variety of solvents, as discussed in more detail in the following section. This analysis depends strongly on experimental scale and equipment design; for example, small scale experiments like those in diamond anvil cells^{71,82} exhibit rapid heat loss when compared to industrial size cells.

5.1.2. Theoretical Temperature Changes Due to Pressurization

The solvent pressurization data clearly show a significant change in temperature with compression through a process that is reversible but not quite adiabatic. By ignoring

the heat transfer losses, the change in temperature with pressure can be derived from the definition of enthalpy and Maxwell's relations. Using the chain rule and substituting standard thermodynamic identities yields

$$\left(\frac{\partial T}{\partial P}\right)_S = \frac{T\alpha\bar{V}}{C_P} \quad (5.1)$$

where T is the temperature, P is the pressure, C_P is the specific heat capacity, \bar{V} is the molar volume, and α is the coefficient of thermal expansion. In general, Equation 5.1 suggests that this effect will be larger in more compressible organic solvents like alcohols and ethers than in less compressible solvents like water.

In order to test the theory developed in Equation 5.1, the temperature change upon compression was measured for a variety of solvents. Figure 5.1b shows the experimental results plotted against theoretical predictions from Equation 5.1 assuming constant material properties obtained from literature.⁸³ A detailed table of thermodynamic

Table 5.1: Thermodynamic quantities used for Equation 5.1.

Solvent	From Ref 83			Calc. from Eqn. 5.1		Experimental
	Thermal Expansion Coefficient α (K ⁻¹) × 10 ⁻³	Heat Capacity C_P (J g ⁻¹ K ⁻¹)	Specific Volume \bar{V} (m ³ g ⁻¹) × 10 ⁻⁶	$\Delta T/\Delta P$ (K Pa ⁻¹) × 10 ⁻⁷	$\Delta T/\Delta P$ (K/10,000 psi)	$\Delta T/\Delta P$ (K/10,000 psi)
Water	0.2070	4.190	1.004	0.145	1.0	1.0
Isopropanol	1.263	2.546	1.271	1.85	12.7	7.6
Methanol	1.199	2.503	1.259	1.77	12.2	7.6
Acetone	1.487	2.160	1.262	2.55	17.6	9.6
Toluene	1.064	1.685	1.151	2.13	14.7	9.4
Hexane	1.381	2.257	1.514	2.72	18.7	10.2
Acetonitrile	1.432	2.218	1.602	3.03	20.9	-
Tetrahydrofuran	1.217	1.702	1.130	2.37	16.3	-
Octanol	0.8822	2.079	1.217	1.51	10.4	-
Diethyl Ether	1.656	2.346	1.401	2.90	20.0	-
Dichloromethane	1.454	1.183	0.7532	2.71	18.7	-
Chloroform	1.255	0.9484	0.6702	2.60	17.9	-

quantities used for these calculations including other solvents not tested experimentally is provided in Table 5.1. The experimental results show less heating due to compression than predicted. The exception to this is water, which was by far the least compressible of the solvents tested and showed very little heating due to compression. Fitting the first 1,000 psig of data and extrapolating reduces the disagreement caused by heat transfer and changes in materials properties with pressure. Although not exact, the agreement is impressive considering the simple nature of the theory. As pressure increases further, this disagreement due to changing material properties will increase and the temperature increase due to any given change in pressure will decrease.

5.2. Determination of Solubility at Elevated Pressure

The effect of pressure on solubility is minor under the typical conditions for crystallization and is often ignored.^{21,70} However, at the high pressures employed during pressure-swing crystallization, this effect becomes more significant. This section employs a novel technique to measure the solubility at elevated pressure, necessitated due to the difficulty of taking measurements at high pressure. A simple model to justify the experimental results is also developed. In these studies, two model compounds, piracetam (2-(2-oxopyrrolidin-1-yl)acetamide), a nootropic drug, and paracetamol (N-(4-hydroxyphenyl)acetamide), a widely used analgesic, were used because of earlier studies in the high pressure literature.^{73,75,76}

5.2.1. Experimental Measurement of Solubility at Elevated Pressure

To measure the effect of pressure on solubility, measurements of solubility were conducted by comparing the nucleation temperature as a function of pressure for a

solution of constant initial concentration. This technique avoids the difficulties associated with taking accurate samples at high pressure for external measurement. In this technique, a solution of known concentration at ambient pressure was allowed to cool below saturation until nucleation was observed. The solubility at nucleation was determined by simply comparing the nucleation temperature to literature values for the solubility.^{84,85} The same nucleation experiment was then repeated as a function of pressure. Because solubility typically decreases with increased pressure, solutions under pressure normally undergo nucleation at higher temperatures.⁸⁶

This behavior can be clearly seen for a solution of paracetamol in water in Figure 5.2a. In this example, nucleation at high pressure was even observed above the saturation temperature at ambient pressure. Assuming that this change in nucleation temperature is entirely due to a change in solubility and ignoring any potential changes in nucleation behavior, the supersaturation at nucleation will be independent of pressure. Holding the initial concentration constant, the solubility at the nucleation temperature measured at elevated pressure is equal to the solubility determined from the nucleation temperature at ambient pressure. Each nucleation experiment thus provides an independent measure of solubility as a function of pressure.

At face value, this appears an inaccurate method for measuring solubility because of the inherent stochastic nature of nucleation. However, plotting the data for a variety of initial concentrations and pressures together according to ideal solution theory as shown in Figure 5.2b averages out the scatter within the data. The experimental slope can then be used to estimate the relative solubility at any pressure compared to the solubility

measured at ambient pressure. This technique is not meant to serve as a substitute for more accurate and well developed methods used to measure solubility, but simply to provide preliminary data in regimes where these are not otherwise easily obtained.

5.2.2. Theoretical Rationale

While intriguing, the results presented in the previous section are limited due to the inherent difficulties associated with operating at high pressure. These results are justified using a simple model for the solubility change expected at high pressure. The change in solubility with pressure was estimated by Hildebrand and colleagues in the 1950s using ideal solution theory, but has been largely ignored since.⁸⁶ The magnitude of this change expected from ideal solution theory is

$$\ln\left(\frac{x}{x_0}\right) = \frac{\bar{v}^S - \bar{v}^{Sol}}{RT\left(\frac{\partial \ln f}{\partial \ln x}\right)_P} \Delta P \quad (5.2)$$

where x is the solubility in mole fraction at high pressure, x_0 is the solubility at ambient pressure, R is the gas constant, T is the solution temperature, ΔP is the change in pressure,

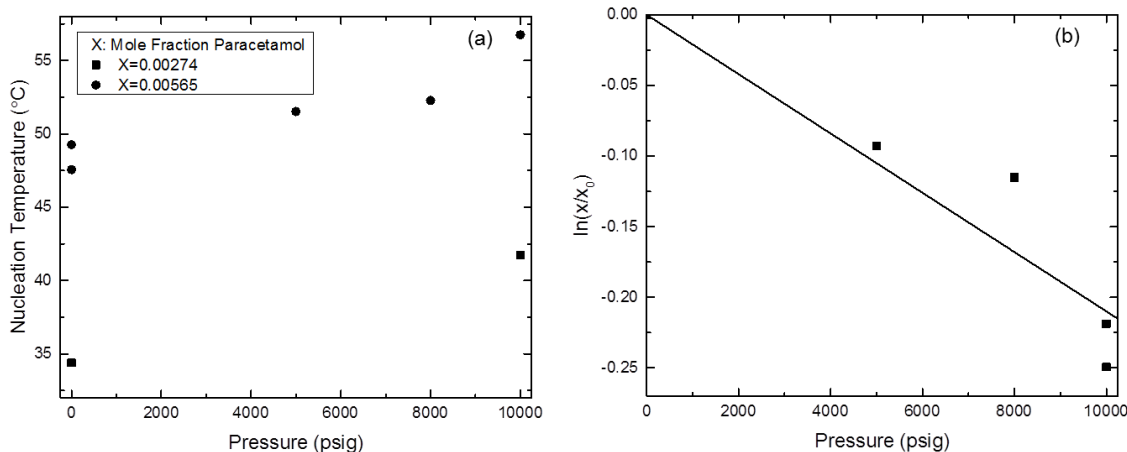


Figure 5.2: (a) The nucleation temperature increases as a function of pressure and mole fraction X for paracetamol in water. (b) Solubility decrease with pressure for paracetamol in water plotted according to Equation 5.3.

\bar{V}^S is the molar volume of the solid solute, \bar{V}^{Sol} is the partial molar volume of the solute in solution, and $\left(\frac{\partial \ln f}{\partial \ln x}\right)_P$ is the change in fugacity as a function of the solubility at constant pressure, equal to one if Henry's law holds. The partial molar volume of the solute in solution \bar{V}^{Sol} can be approximated as the molar volume of the subcooled solute in molten form \bar{V}^L at the solution temperature, implicitly assuming the mixing of solute and solution is additive. Together, these assumptions yield

$$\ln\left(\frac{x}{x_0}\right) = \frac{\bar{V}^S - \bar{V}^L}{RT} \Delta P \quad (5.3)$$

If the solute as a subcooled melt is less dense than the solid, Equation 5.3 predicts a decrease in solubility with increasing pressure that is independent of solvent choice. This is expected to be true for the majority of systems, with a notable exception being electrolytes such as calcium carbonate in seawater.⁸⁷

If the solid and subcooled melt densities of the solute are nearly temperature independent, the dependence of solubility on pressure can be estimated by combining Equation 5.3 with simple density measurements. The solid densities of paracetamol and piracetam at room temperature and pressure were obtained from the literature.^{88,89} The melt densities of paracetamol and piracetam were measured to be 1.13 ± 0.02 g/mL and 1.14 ± 0.01 g/mL, respectively, at their respective melting points, as described in Chapter 2. Together, these values were used to calculate the dependence of solubility on pressure as presented in Table 5.2. Equation 5.3 also provides a rationalization for the linear fit in Figure 5.2b where the slope of this line, equal to $\frac{\bar{V}^S - \bar{V}^L}{RT}$, is listed in Table 5.2.

This argument implicitly assumes that the difference in molar volume between the solid and melt is constant as a function of increasing pressure. If the melt is significantly more compressible than the solid, the change in

Table 5.2: Predicted values for the change in solubility with pressure from Equation 5.3 compared to experimental values obtained from nucleation temperature as shown in Figure 5.2b.

Solubility Change with Pressure (Slope from Equation 5.3)		
Solute	Predicted (psi⁻¹) × 10⁻⁵	Experimental (psi⁻¹) × 10⁻⁵
Paracetamol	-4.1±0.6	-2.1±0.2 (in Water)
Piracetam	-5.6±0.4	-2.5±0.1 (in Ethanol)

solubility for a given change in pressure is expected to decrease as a function of increasing pressure. The theory predicts a decrease in solubility with pressure that is about a factor of two larger than the experimentally measured value. This discrepancy is most likely due to the change in melt density measured at the melting temperature to the solution temperature and variations in these properties as a function of increasing pressure. Considering this, the agreement between the experimental and theoretical prediction is good and provides further validation of the experimental technique.

5.3. The Effect of Rapid Pressurization on Solubility

As a solution is pressurized, the solubility decreases according to Equation 5.3; however, the solubility also increases due to the increase in temperature from adiabatic compression predicted by Equation 5.1. The size of the two effects depends on different system properties, but tends to be similar in magnitude. The increase in temperature is largely dictated by solvent properties such as heat capacity and compressibility, while the decrease in solubility with pressure depends on the difference in molar volume between the solid and molten solute.

In order to illustrate the interplay between these effects, the solubilities of paracetamol in water and piracetam in ethanol under ambient pressure are re-plotted from literature in Figure 5.3.^{84,85} Solubility at 10,000 psig is plotted using the experimental

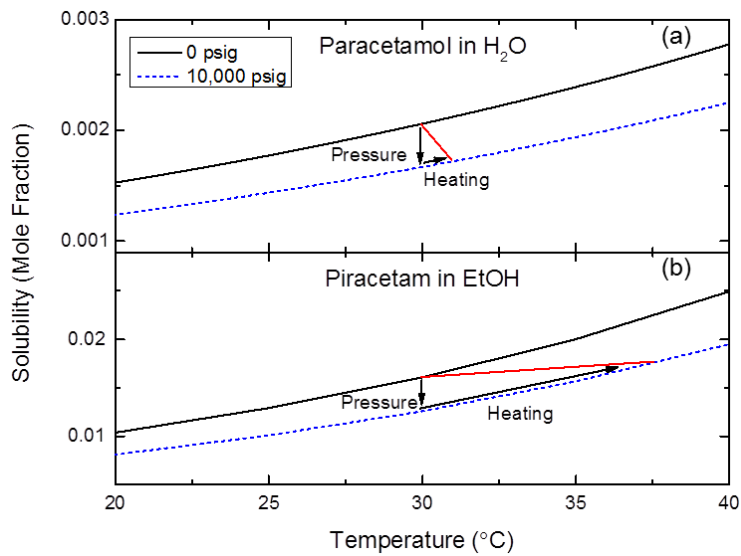


Figure 5.3: (a) Predicted decrease in solubility upon pressurization for paracetamol in water. (b) Predicted increase in solubility upon pressurization for piracetam in ethanol.

pressure dependences measured in Section 5.2 and listed in Table 5.2. The overall change in solubility upon pressurization can be read from Figure 5.3 using the temperature change due to adiabatic compression measured in Section 5.1. Interestingly, the observed solubility of paracetamol in water decreases as pressure increases, while the observed solubility of piracetam in ethanol increases. This result emphasizes the importance of incorporating these two opposing effects into experimental design. This may provide an interesting avenue for future exploration due to the ease of maintaining uniform pressure control.

5.4. Conclusions

Simple models were developed that estimate the change in solubility as a function of pressure and predict the temperature increase due to adiabatic compression. These

models were validated with crystallization experiments conducted under high pressure. Interestingly, the decrease in solubility with pressure is often balanced by an increase in solubility caused by the temperature increase due to adiabatic compression. This yields a solubility that can increase or decrease upon pressurization. The interplay between these two effects was discussed and a simple method to determine changes in solubility during pressurization was developed. These two properties have fundamentally different origins, and provide an interesting dimension to crystallization design. This will be discussed in detail for pressure-swing crystallization in Chapter 6.

6. Applications for Pressure-Swing Crystallization

Crystallization is a critical process throughout the chemical industry, particularly for high value, low volume, specialty chemicals. Traditionally, crystallization is conducted as a batch process followed by filtration to collect the final product. Crystal nucleation is either seeded or induced. Product specifications are varied, but typically include crystal size, shape, polymorphic form, and purity.^{21,70}

Process control is typically achieved by using temperature to adjust the solubility of the target material, but solvent composition is also sometimes adjusted as in anti-solvent crystallization. In either approach, the key variable which controls crystallization is the solubility of the target material in the solvent. Here, we present an alternative approach to control the solubility, pressure-swing. As the name states, pressure-swing crystallization utilizes changes in pressure to control the solubility during crystallization. Pressure-swing crystallization has a variety of potential applications, which are discussed in more detail below.

6.1. Advantages of Pressure-Swing Crystallization

The solubility data presented in Chapter 5 show that a rapid change in pressure can be used to modify the solubility of a target molecule in solution. Depending on the solvent and solute choice, the solubility may either increase or decrease upon pressurization. While the details are discussed in Chapter 5, for the purpose of this chapter, a simple rule of thumb is that in organic solvents, the solubility increases upon pressurization, and for aqueous solutions, the solubility decreases upon pressurization. Importantly, this change in solubility is reversible, such that a rapid decrease in pressure

yields a decrease in solubility for organic solutions and an increase in solubility for aqueous ones. Pressure-swing crystallization employs this change in solubility with pressure to achieve the same objectives as traditional temperature or solvent control.

Using pressure to change solubility in this way presents several advantages over traditional approaches. First, changes in pressure travel at the speed of sound throughout the solution. This translates to rapid and uniform changes in solubility throughout the solution, minimizing issues associated with temperature uniformity or cold-spots encountered using traditional temperature control. Second, it is often much faster to change the pressure of a solution than to change the temperature. For example, opening a release valve takes seconds, while cooling a 1000L reactor can take hours. Using this approach, rapid changes in solubility are achievable at the industrial scale. Finally, changes in hydraulic pressure are easily achieved for most solutions due to the limited compressibility of liquids.

The following sections describe how pressure-swings can be employed to control a variety of typical operations encountered during crystallization including nucleation, polymorphic control, and crystal digestion. We have found that although similar changes in solubility can be achieved, experiments using pressure-swing to replicate results achieved using traditional temperature control are not always successful. Significant additional research is needed before pressure-swing can be implemented at scale.

6.2. Nucleation Control

Despite the best efforts of many researchers, many fundamental aspects surrounding nucleation are unknown.²⁹ Industrially, nucleation is often practiced

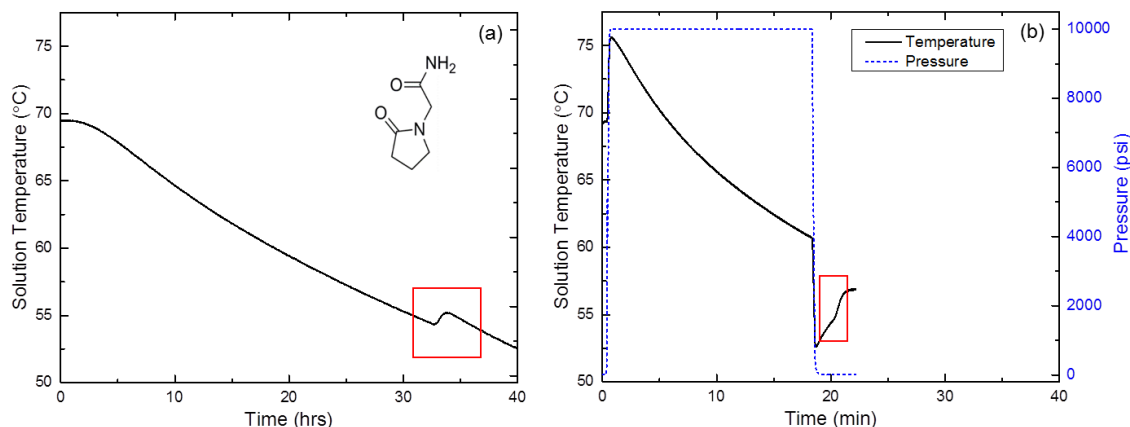


Figure 6.1: (a) Nucleation of piracetam in ethanol after slowly cooling in the pressure crystallizer. Inset shows piracetam molecular structure. (b) Nucleation of piracetam after a rapid drop in pressure.

qualitatively, and appropriate nucleation conditions are determined empirically. Sometimes, even inducing nucleation is difficult due to the inherent stochastic nature of nucleation. To avoid this issue, many processes utilize seed crystals to avoid nucleation altogether. Here, we demonstrate that pressure-swing can be used to induce nucleation, using piracetam in ethanol as a model system.

First, a solution of piracetam in ethanol was prepared in the pressure crystallization system described in Chapter 2. The solution was prepared such that it was saturated at 60°C. The solution was heated to 70°C and stirred until the piracetam was fully dissolved. The heater was then turned off and the solution was allowed to cool slowly. Figure 6.1a shows the temperature profile for this cooling. After approximately 33 minutes and at a temperature of approximately 54°C, a spike in temperature was observed, corresponding to the nucleation and growth of piracetam crystals. After the initial spike in temperature associated with the rapid crystal growth following nucleation, the solution continued to cool, further driving slow crystal growth. This represents a

traditional crystallization process, after which the piracetam crystals were filtered and collected.

In the pressure-swing case, shown in Figure 6.1b, an identical solution of piracetam was prepared and allowed to cool. However, as the cooling began, the solution was pressurized from ambient pressure to 10,000 psig. This pressurization resulted in approximately a 7°C increase in the solution temperature. Because this increase in temperature only occurred in the solution, and not the reactor walls, the solution cooled more rapidly than in the control case. After approximately 18 minutes and at a solution temperature of 61°C, the solution was rapidly depressurized to ambient pressure. This rapid decrease in pressure resulted in a 7°C decrease in temperature. Again, because only the solution changed temperature and not the reactor walls, the solution temperature immediately began to increase back to that of the reactor. Because this was an organic solution, the net impact of depressurization was a net decrease in solubility, such that the solution became supersaturated. This supersaturation induced piracetam nucleation, indicated by the sharp change slope in the temperature curve 20 minutes after the start of the experiment.

This was a clear demonstration that a rapid change in pressure could be used to induce crystal nucleation. Due to heat transfer effects, pressure-swing even resulted in a 40% reduction in the nucleation time. While not a large improvement in practice, this illustrates some of the appeal of the pressure-swing technique.

Although demonstrated here for an organic solution, this result has also been observed for other model systems, including aqueous ones. However, in the aqueous

case, an increase in pressure is used to induce nucleation, resulting at nucleation events above ambient pressure. Interestingly, nucleation at elevated pressure can impact the product polymorph and may be of interest for specific polymorph generation.

6.3. Polymorph Generation

Careful control of polymorphic form is important, especially in the pharmaceutical industry due to the varying processibility and bioavailability of different polymorphs. This has led to significant efforts to identify and manufacture more desirable polymorphic forms of known bioactive materials.^{22,90} In general, polymorphic control is straightforward when the most thermodynamically stable polymorph is desired. Over time, a mixture of polymorphs in solution will convert into a pure solution of the most stable polymorph due to a process known as solvent mediated phase transformation.²¹ Thermodynamically less stable forms are typically more soluble than stable ones, resulting in preferential dissolution of metastable polymorphs and growth of stable ones. This process eventually results in a pure solution of the most stable polymorphic form. In order to generate a less stable or kinetic polymorph, great care must be taken to ensure that a more stable polymorph does not nucleate within the solution. This is often quite difficult in practice, and has led to a variety of processing challenges.

6.3.1. Nucleation at High Static Pressure

Recent work has shown that crystallization under high pressure can produce polymorphic forms not available or difficult to obtain through standard crystallization techniques.^{71,72} For example, Fabbiani et al. observed a new polymorph of piracetam

predicted by computer simulation but inaccessible using traditional approaches.^{73,74,91} Crystallization at high pressure can also be used to generate novel solvates^{73,75} and co-crystals,⁷⁶ useful for a variety of applications.

In this technique, a high static pressure is maintained during nucleation and crystal growth. Because thermodynamic stability varies as a function of pressure, different polymorphic forms may be stable at high pressure compared to ambient pressure. This can result in the nucleation of unique or otherwise difficult to obtain polymorphic forms. Most high pressure crystallization is conducted in diamond anvil cells with sample volumes much less than 1 mL and at pressures 5-10 times larger than those encountered during pressure-swing crystallization. Currently, this technique is limited to polymorph discovery, but may be used to produce novel polymorphic forms in the future.

This approach is fundamentally different from pressure-swing. In pressure-swing, a change in pressure is used to change the solubility within the solution. This change in solubility can be used to achieve desired changes in crystallization. In high pressure crystallization, a static pressure is used to alter the fundamental thermodynamic stability between different crystal polymorphs. It is important to note that for some materials, this change in thermodynamic stability may be encountered at pressures relevant to pressure-swing.

6.3.2. Nucleation at High Induced Supersaturation

It is known that the product polymorph is often dictated by the thermodynamic driving force, or supersaturation at the time of nucleation.²¹ At high supersaturation,

kinetically-favored, metastable polymorphs are formed. During slow crystallization and at low supersaturation, more thermodynamically stable forms are favored. This behavior is sometimes referred to as Ostwald's rule of stages.⁹² Pressure-swing crystallization can potentially be used to control the product crystal polymorph by altering the supersaturation at the time of nucleation. In this case, a rapid change in pressure prior to nucleation could change the supersaturation such that the nucleation of a metastable polymorph is preferred. The following two sections describe the validation of an appropriate model system for polymorphic control and subsequent attempts to control the product polymorph using pressure-swing crystallization.

6.3.2.1. Supersaturation Control using Temperature

Two model systems were explored with respect to polymorphic control, piracetam in ethanol and paracetamol in water.

From previous literature, both compounds exhibit multiple polymorphs that can be selected based on the supersaturation at the time of nucleation.^{37,93} In order to demonstrate control over product polymorph, a simple

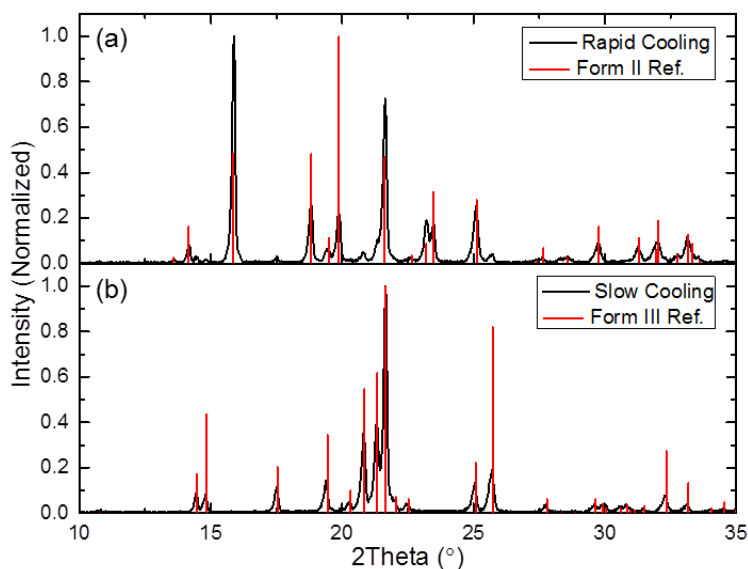


Figure 6.2: (a) Rapidly cooling piracetam induces nucleation at high supersaturation, yielding metastable Form II. (b) Slowly cooling piracetam induces nucleation at low supersaturation, yielding stable Form III.

experiment was conducted using piracetam in ethanol on the benchtop.

Piracetam has two primary polymorphs at room temperature: Form II is metastable and Form III is the stable form. In order to generate these two forms, the cooling rate of a solution of piracetam in ethanol was varied by placing the sample solution in either an ice bath or a slowly cooling metal block. Adjusting the cooling rate adjusts the temperature at the time of nucleation, and hence the supersaturation at the time of nucleation. The product crystals were collected via vacuum filtration and analyzed using powder XRD. Figure 6.2 clearly shows that when cooled rapidly, piracetam nucleates as the metastable Form II polymorph. When cooled slowly, it nucleates as the stable Form III polymorph. This result agrees with the literature and demonstrates our capability to control product polymorph using traditional approaches.³⁷

6.3.2.2. Supersaturation Control using Pressure-Swing

Attempts to replicate this control over product polymorph using pressure-swing crystallization were unsuccessful. In theory, a rapid change in pressure results in a rapid change in solubility, which can be used to induce nucleation of a metastable polymorph. Experimentally, this was accomplished by either rapidly pressurizing or depressurizing a solution immediately prior to a nucleation event. In this way, the supersaturation at the time of nucleation was increased. However, compared to the change in supersaturation generated in the previous section by simply placing the solution in an ice bath, the change in supersaturation generated by pressure-swing crystallization was minor. As a rule of thumb, a 10,000 psi change in pressure only results in a net change in solubility

equivalent to a 5°C change in temperature. The changes in temperature required here are on the order of 40°C, almost an order of magnitude larger.

This was tested by allowing solutions of paracetamol and piracetam to cool slowly and recording the nucleation temperature. The experiment was then repeated, but with a rapid pressure-swing added immediately before the solution was expected to nucleate. This pressure-swing rapidly increased the supersaturation and triggered nucleation, similar to the case shown in Figure 6.1. Unfortunately, for both of the cases studied, the supersaturation generated using pressure-swing was not large enough to generate the desired metastable polymorph. This is shown more clearly in Table 6.1 where supersaturation σ is defined as $\sigma = \ln(x/x_0)$, where x_0 is the equilibrium concentration and x is the actual concentration of the solute in solution. These results do not mean that pressure-swing crystallization cannot be used to control the product polymorph, but that it is only appropriate where small changes in solubility are required. A subsequent search of the literature did not yield any promising candidates for polymorphic control using this approach.

Table 6.1: The additional supersaturation generated using the pressure-swing technique is not large enough to induce nucleation of the metastable polymorph for piracetam or paracetamol.

Solute	Solvent	Required Supersaturation to Nucleate Metastable Polymorph (from Refs. 12, 13)	Maximum Supersaturation using Pressure-Swing
Piracetam	Ethanol	0.86	0.23
Paracetamol	Water	1.2	0.31

6.4. Purification via Crystal Digestion

Digestion is a common process used to increase the product purity in industrial crystallization.⁹⁴ During digestion, a portion of the product crystal mass is intentionally dissolved and allowed to regrow. Because impure crystals are typically less thermodynamically stable than pure crystals, they tend to dissolve more rapidly. Thus dissolution preferentially removes impure crystals, resulting in a more pure product. This process is especially effective when practiced shortly after nucleation, as nuclei typically have a broad purity distribution. Including a digestion step ensures that subsequent growth only occurs on the most pure nuclei.

Digestion is typically achieved by increasing the solution temperature, and hence the solubility, shortly after nucleation. The temperature is typically increased until the solution is just under the saturation temperature, such that the majority of the crystal mass is dissolved. The temperature is then allowed to slowly cool in order to promote pure crystal growth. This process is time consuming, often taking hours to heat and cool and industrial size crystallizer.⁹⁴ Pressure-swing crystallization has the potential to greatly reduce this processing time, using rapid changes in pressure instead of temperature swings to alter the solubility. The following two sections describe attempts to replicate this digestion process using pressure-swing crystallization. Section 6.4.1 describes the selection and validation of an appropriate model system and Section 6.4.2 describes the pressure-swing digestion experiments.

6.4.1. Digestion using Temperature Control

In order to test the ability of pressure-swing to improve crystal product purity via digestion, benchtop experiments were first employed to determine an appropriate model system. This process required screening multiple target materials and impurities for appropriate behavior. Water was chosen as the solvent because previous results found the largest changes in solubility upon pressurization in aqueous solutions. The following section describes this process employed for screening target systems using paracetamol doped with metacetamol as an impurity as a model system.

The first requirement for potential model systems was controllable incorporation of a known impurity into product crystals. This was tested by preparing solutions of the target molecule with varying amounts of an impurity molecule. The solutions were heated to dissolve all of the solute and then allowed to cool and crystallize. The product crystals were collected via vacuum filtration and then analyzed for purity. The results for this experiment

are shown in Figure 6.3a for paracetamol, using metacetamol as an impurity. These results show that the product purity

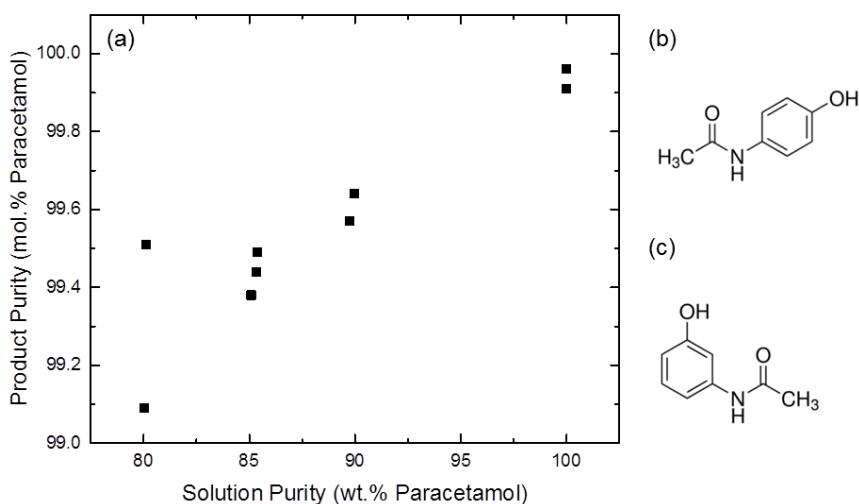


Figure 6.3: (a) Metacetamol is incorporated into paracetamol as an impurity. Two crystal phases exist below 85 wt. %. (b) Paracetamol molecular structure. (c) Metacetamol molecular structure.

was inversely proportional to the amount of impurity in solution, as expected for a well behaved model system. Interestingly, at concentrations above 15 wt.% in solution, two solid phases formed, resulting in undesirable product variability. This type of trend in purity was observed for many impurities, like metacetamol, which are similar in molecular structure to the target molecule

The second requirement for potential model systems was an improvement in purity when subjected to a traditional digestion process. As described previously, digestion involves dissolving a portion of the crystal mass by heating the solution and then allowing it to cool and regrow. This preferentially dissolves impure crystals, resulting in an increase in purity. Figure 6.4a shows a typical temperature profile for this process. The corresponding solubility of paracetamol in water is shown in Figure 6.4b along with the expected product crystal mass assuming that the starting solution is saturated at 40°C. This analysis ignores crystal growth kinetics, implicitly assuming that the amount of crystal mass is determined solely by solubility.

Experimentally, an 85/15 wt.% solution of paracetamol/metacetamol was digested

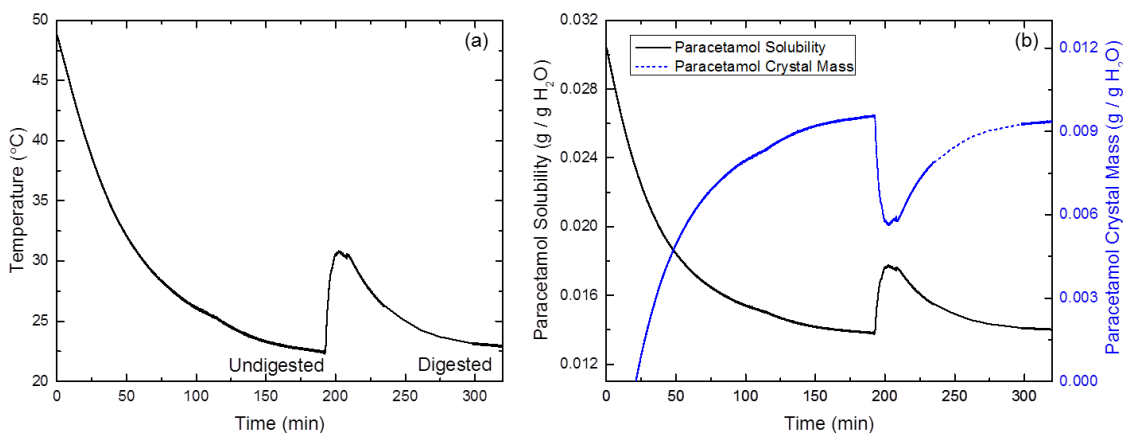


Figure 6.4: (a) Temperature profile during typical digestion experiment. (b) Solubility and crystal mass predicted from solubility, ignoring growth kinetics.

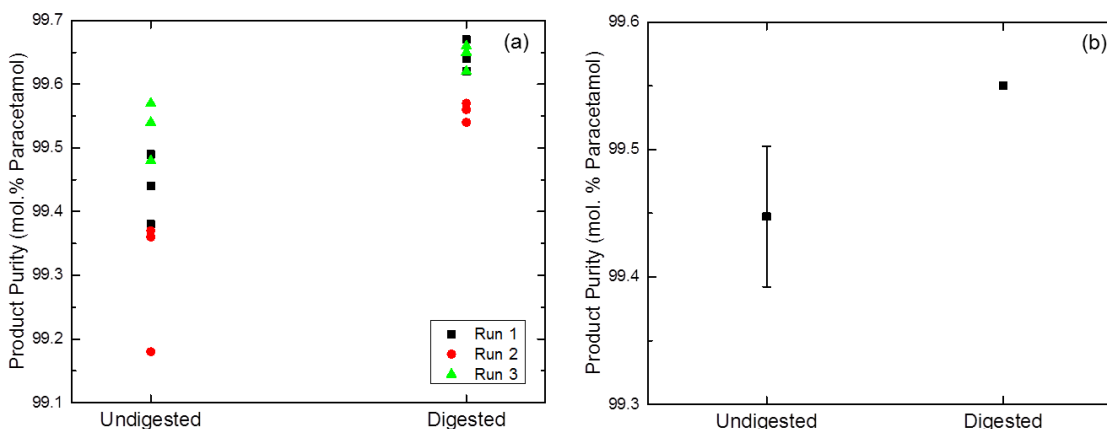


Figure 6.5: (a) Digestion experiments conducted on the benchtop show that digested crystals are more pure than undigested crystals. The run to run variation is due to fluctuations in the cooling rate. (b) Results from a similar experiment conducted in the pressure crystallization system using similar temperature control also show an increase in purity.

in order to determine whether paracetamol was a valid model system. The results from these experiments, shown in Figure 6.5a, show a clear increase in purity for digested crystals. It is important to note that significant run-to-run variation was observed, probably due to limited control of the cooling profile. This issue was minimized in the pressure crystallization system which used an active cooling approach. Interestingly, the addition of metacetamol increased the solubility of paracetamol slightly, such that the amount of crystal product was less than that predicted by Figure 6.4b. Finally, this experiment was repeated in the pressure crystallization apparatus in order to exclude any potential errors associated with the differences in equipment or experimental conditions. A similar increase in purity was observed in the pressure crystallization system, as shown in Figure 6.5b. Based on these results, an 85/15 wt.% solution of paracetamol/metacetamol was used to test the ability of pressure-swing crystallization to control digestion.

6.4.2. Digestion using Pressure-Swing

Pressure-swing digestion uses the same approach as traditional digestion. After nucleation, a change in pressure is used to increase the solubility, dissolving a portion of the crystal mass. An example experimental profile for pressure-swing digestion is shown in Figure 6.6a. Since the chosen target system is aqueous, the decrease in pressure corresponds to an increase in solubility. This is shown more clearly in Figure 6.6b, which displays paracetamol solubility and the predicted product crystal mass during the experiment. Again, this prediction assumes that the solution is pure paracetamol saturated at 40°C and ignores crystal growth kinetics. While this profile shows how digestion can be achieved using a pressure-swing, experimental results did not show a corresponding increase in purity.

The pressure-swing digestion process was tested experimentally using an 85/15 wt.% solution of paracetamol/metacetamol. The solution was heated until the solute dissolved and then allowed to cool until crystals formed. In the control case, the

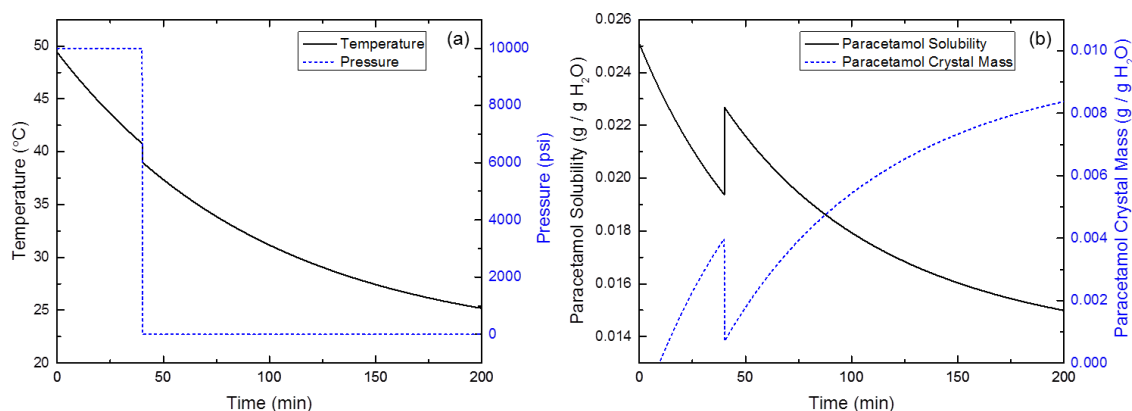


Figure 6.6: (a) Temperature and pressure profile for a typical pressure-swing digestion experiment. (b) Solubility and crystal mass predicted from solubility of pure paracetamol, ignoring growth kinetics.

experiment was conducted at ambient pressure. In the pressure-swing digestion case, the experiment followed the profile outlined in Figure 6.6a. The solution was first pressurized to 10,000 psig and then allowed to cool. After nucleation,

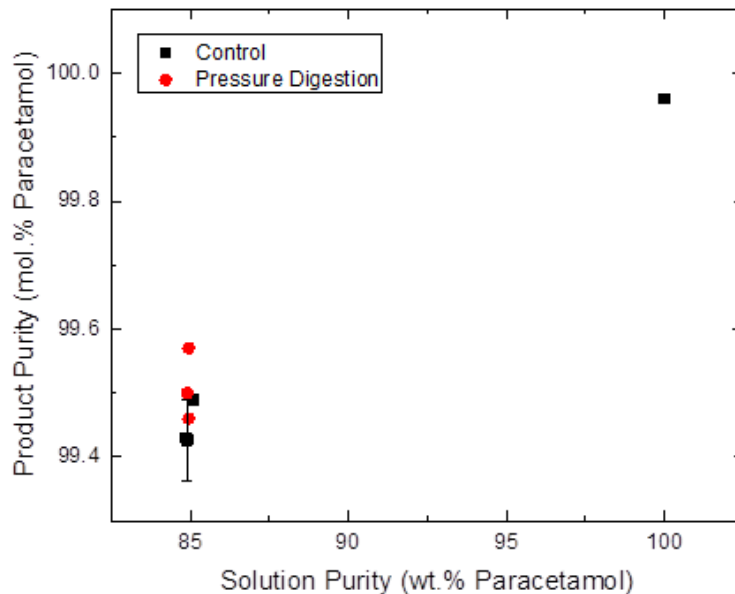


Figure 6.7: Purity does not noticeably increase for pressure-swing digestion.

the pressure was reduced to ambient in order to increase the overall solubility. This resulted in a significant digestion step, even visible by eye through the vessel's viewports. The product crystals were collected via vacuum filtration and analyzed for purity. Even though the digestion process was successful, no increase in product purity was observed, as seen in Figure 6.7.

Due to the impact of metacetamol on paracetamol solubility, the exact solubility profile for the target solution remains unknown. This resulted in some uncertainty for the appropriate conditions for digestion, especially as a function of pressure. In order to alleviate these concerns, pressure-swing digestions were conducted as a function of initial temperature. Experimentally, the location of the pressure change was varied along the cooling curve, as shown in Figure 6.8a. This resulted in the dissolution of a varying amount of the product crystal mass, essentially changing how aggressive the digestion

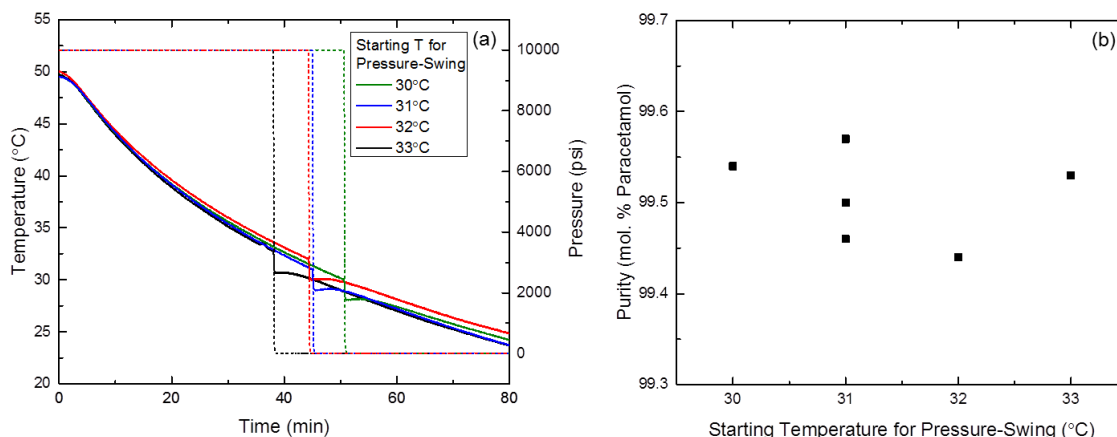


Figure 6.8: (a) Temperature and pressure profiles for pressure-swing experiments as a function of the starting temperature for the pressure-swing, effectively varying the percentage of crystal mass dissolved during the digestion step. (b) Purity of digested crystals is not a function of the percentage of crystal mass digested. When the pressure-swing was initiated at 33°C, the crystals were completely dissolved during the digestion step.

process was. In the extreme case, where the pressure change was initiated at 33°C, the crystal mass was completely dissolved, necessitating a second nucleation event prior to crystal growth. If an error in the solubility calculation were to blame for the lack of purity improvement, one might expect to see an increase in purity as a function of the amount of crystal mass digested. This is clearly not the case, as shown in Figure 6.8b.

Although the solubility profile was similar to that successfully used during traditional digestion, no increase in purity was observed for pressure-swing digestion. This could potentially arise due to differences in nucleation or crystal growth a function of pressure. However, we do not have the experimental capabilities, such as in-situ polymorph identification, required to explore these possibilities.

6.5. Conclusions

Pressure-swing crystallization is a novel alternative to traditional control of crystallization processes. It offers an additional dimension to crystallization design and

has several attractive properties compared to traditional approaches. Changes in pressure occur rapidly and uniformly throughout a solution, leading to rapid and uniform changes in solubility. Additionally, the change in solubility due to pressure is reversible, yielding interesting possibilities for process design.

However, we were unable to show how these potential process improvements could be realized. Experimentally, we demonstrated that pressure-swings can be used to control the solubility within crystallization processes. These changes were used successfully to induce crystal nucleation. However, attempts to control product polymorph and increase product purity via digestion were unsuccessful. Whether this failure is due to fundamental limitations with the process or poor model system choice is unknown.

7. Conclusions and Future Research

The purification of specialty chemicals is a key step in the production process for many of the world's materials. The previous chapters have described the results of our research efforts to improve two major purification techniques, thermal gradient sublimation and crystallization. These efforts were successful in part, but many questions remain. This chapter summarizes those results and presents a selection of the remaining research questions surrounding these techniques.

7.1. Thermal Gradient Sublimation

Thermal gradient sublimation is currently used to purify organic semiconducting materials at the industrial scale. Despite this, it is often practiced qualitatively and optimized empirically. Chapters 3 and 4 describe our efforts to develop a theoretical model which identifies the mechanism for the sublimation process and can be used for scale-up and process design. These efforts were in part successful, and are currently being implemented at The Dow Chemical Company. However, many key questions remain. Some are academic, and others are important for industry.

7.1.1. Sublimation Research Summary

The primary objective for the sublimation research was to develop a model which describes the process in order to guide scale-up and process design. The first step in this development was to determine the rate-limiting step within the sublimation process. Despite our initial intuition, we found that the rate-limiting step for thermal gradient sublimation was not in the solid-state, but was instead vapor transport and deposition. Chapter 3 describes this research in more detail.

Once the vapor phase was identified as rate-limiting, a series of experiments were designed in order to identify the specific mechanism for vapor transport. These experiments showed that diffusion was the dominant transport mechanism, as described in Chapter 4. Using basic diffusive theory, we were able to build a simple model which describes vapor transport and deposition within the sublimation process. This model matches the experimentally observed deposition behavior and trends in system geometry. We suggested guidelines for scale-up and process design based on this understanding. However, due to the simplicity of the model, it underestimated the rate of sublimation by a factor of four. This disagreement and other open questions are discussed in the following sections.

7.1.2. Impact of Material Bonding on Rate-Limiting Step

Perhaps the most surprising discovery from this research is that the sublimation process is limited by the vapor phase, not the solid phase. This result, which disagrees with previous sublimation research^{53,56,95,96} and was completely unexpected, was observed for both model systems used within this dissertation, and we have no reason to suspect that it will vary among similarly structured organic semiconducting materials.

This behavior might be explained by the weak Van der Waals bonding between organic semiconducting molecules. Compared to that of inorganic materials or ionically bonded organics, the bond dissociation energy for organic semiconductors is much lower.^{53,55,97} This results in a significantly lower energy barrier for an individual molecule to leave the solid phase in organic semiconductors compared to other materials. This difference in energy could contribute to the difference in sublimation mechanism.

Although speculative, this explanation could be experimentally validated. First, a series of materials with a variety of bonding types should be selected as model systems. The vapor pressure of each material should be measured as a function of temperature. Then, the rate-limiting step for sublimation could be determined using the experimental approach described in Chapter 3. If this hypothesis is valid, the solid phase should become less limiting with decreasing bond energy. This type of analysis would be useful for future sublimation process design.

7.1.3. Impact of Elevated Temperature on Sublimation

Chapter 3 showed that the rate-limiting step for thermal gradient sublimation is vapor transport. The driving force for this vapor transport is the vapor pressure of the target material at the sublimation temperature. As shown in Chapter 2, the vapor pressure increases exponentially with temperature, suggesting that the sublimation rate should also increase exponentially with temperature. In order to test this theory, the sublimation rate of TCTA was measured as a function of temperature, as shown in Figure 7.1a. The

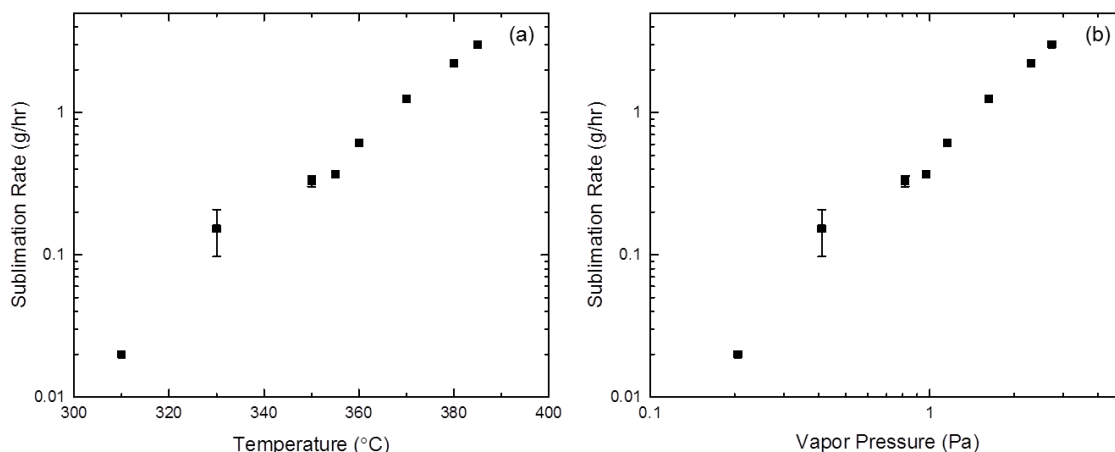


Figure 7.1: (a) TCTA sublimation rate increases exponentially with pressure. (b) TCTA sublimation rate appears to increase linearly with vapor pressure, but analysis is limited due to limited vapor pressure resolution.

sublimation rate is shown on a logarithmic scale, illustrating the clear exponential increase in sublimation rate. Experiments conducted at higher temperatures than those shown here resulted in sublimation rates too large to measure using our current experimental setup. Figure 7.1b shows this same sublimation data as a function of the TCTA vapor pressure measured in Chapter 2. While the sublimation rate appears to increase linearly with temperature, this agreement is highly dependent on the accuracy of the vapor pressure data. Due to the difficulty encountered when measuring the low vapor pressures encountered at low temperatures, this result should be regarded as preliminary.

Interestingly, measuring the sublimation rate as a function of vapor pressure provides an additional method to distinguish between vapor transport mechanisms. If diffusion or Knudsen diffusion dominates vapor transport, then the sublimation rate should be directly proportional to the vapor pressure or concentration. If laminar flow is the dominant vapor transport mechanism, then the sublimation rate should increase as a function of the vapor pressure squared. Based on the results presented in Section 4.5.2, an increase in vapor pressure by an order of magnitude should change the dominant transport mechanism from diffusion to laminar flow. We see no evidence of that here. This result is discussed in more detail in Section 7.1.5.

7.1.4. Trade-off between High Temperature and Degradation

The previous results suggest that the sublimation process should be operated at the highest possible temperature. While this will indeed achieve the largest possible sublimation rate, it does not take into account the purity of the product. As the temperature increases, intramolecular bonds can break, degrading the feed material. This

process can lead to decreased product yield and purity at high degradation rates. If the degradation products are significantly different in molecular weight and vapor pressure, they can be separated by the temperature gradient within the deposition zone, alleviating concerns about product purity. However, there is no way to recover the loss in product yield. In this sense, the ideal operating temperature is dictated by the economic balance between separation throughput and product yield. Because the thermal stability varies from molecule-to-molecule, this must be determined individually for each product.

7.1.5. Detailed Transport Mechanism

While the transport model developed within this dissertation fits the experimental results and is useful for process design, several key questions remain. This section provides a discussion of these questions, which are academically interesting but likely unimportant for industrial process design.

First, the agreement of the experimental data with a diffusion model does not mean that the sublimation mechanism involves intermolecular diffusion or even self-diffusion. In intermolecular diffusion, there are two solutes;²⁰ here, there is one. In self-diffusion, there is one solute, but a portion of this solute can be separately identified; here, no such identification is possible. Moreover, diffusion is normally measured relative to a reference velocity, most often a volume average velocity. In many experiments, this velocity is zero; here, this velocity is not zero. At the same time, the results here match diffusion equations, as do turbulent dispersion,⁶¹ “collisionless diffusion”,⁶⁰ and Taylor-Aris dispersion.^{68,69} This disagreement with the fundamental definition of diffusion does not invalidate the developed model, but suggests that an

alternate theoretical framework is needed to describe the fundamental transport mechanism.

We have made an attempt to describe this process using the theory of volume diffusion with some success.⁹⁶ However, this explanation is not complete and we have not reached a satisfying conclusion. This transitional transport regime between flow and Knudsen diffusion, first studied by Knudsen in 1909,³⁹ is still an area of ongoing research. While our initial experiments at low temperature clearly fall in this transitional transport regime, the higher temperature data presented in Section 7.3.1 do not. We expected to observe laminar flow in this regime as discussed in Section 4.5.2. This was not the case, although this conclusion relies on a limited data set.

This apparent lack of transition to laminar flow may be attributed the transition between transport regimes as material moves down the tube. The diffusion model predicts a linear decrease in pressure from the boat to the onset of deposition followed by an exponential decrease in the pressure in the deposition region. At some point during this process, the pressure will decrease such that there is likely a transition to another transport regime. This possibility is not accounted for in our simple model and may impact the overall sublimation rate.

The deposition process provides another possible explanation for this result. Laminar flow in a pipe typically exhibits a parabolic velocity profile, with vapor near the wall moving more slowly than vapor near the center of the tube. Because deposition only occurs at the wall, it may preferentially remove “slow” vapor, resulting in a velocity profile that is more uniform or “plug-like” than expected.⁹⁸⁻¹⁰⁰ This would alter the

geometrical dependences and yield an overall sublimation rate different than that predicted by laminar flow alone. These and other theories are currently being explored in more details using computational fluid dynamics simulations.

Finally, our predictions for the rate of sublimation are about a factor of four less than what we observe experimentally. This error is small, considering the simplicity of the model. However, there are several sources of error within our calculation could cause this, and that may be addressed. First, the vapor pressure data have significant scatter, resulting in significant uncertainty as discussed in Chapter 2, though a factor of four seems a larger uncertainty than expected. Additionally, our model assumes that large, organic semiconductors can be modeled as rigid spheres. This is not entirely accurate, and will alter the calculated diffusion coefficient. This seems unlikely, because a factor of four would require that these molecules behave as if they are a factor of two smaller than calculated, or 0.5 nm in diameter. Finally, our model assumes that the transport is diffusive throughout the entire tube. As discussed above, this may not be the case.

7.2. Crystallization

Crystallization is a ubiquitous process throughout the chemical industry. While well studied, many aspects surrounding crystallization are still unknown. In Chapter 5, we explored the impact of rapid pressurization on crystallization. This research not only provides a thermodynamic background for experiments conducted at elevated pressure, but also suggests an alternative method for controlling solubility during crystallization processes. This pressure-swing approach was explored in Chapter 6 with mixed results.

7.2.1. Research Summary

Our research in high pressure crystallization was motivated by the idea of controlling solubility with changes in pressure instead of changes in temperature. In order to explore this idea, we first needed to develop a model for the change in solubility as a function of pressure. Due to the difficulty of operating at elevated pressure, we resorted to a unique, nucleation-based method for solubility measurement. This resulted in not only useful thermodynamic data, but also provided an additional technique for collecting solubility data under challenging experimental conditions. These experiments, supported by a simple thermodynamic model, provided the necessary background for the pressure-swing crystallization project. Interestingly, they showed that an increase in pressure can result in either an increase or decrease in solubility, depending on the model system. These results are not only useful for the pressure-swing crystallization project, but are applicable to the broader high pressure crystallization community.

Although an intriguing approach, pressure-swing crystallization was not able to reliably reproduce the results achieved using traditional temperature controlled crystallization. While we were able to use a swing in pressure to induce nucleation, we were not able to dictate the product polymorph that nucleated. While rapid, the change in solubility due to pressure was limited due to the maximum operating pressure of our crystallizer. That is, a change in 10,000 psig is only equivalent to approximately a 5°C change in temperature. This change was not enough to dictate the product crystal polymorph during our experiments.

Additional experiments using a pressure-swing to improve product purity via crystal digestion were also unsuccessful. This result was more surprising, as the change

in solubility during the pressure-swing was comparable to that in the temperature case. Even though the crystals were successfully digested, the product purity did not increase. The reason for this failure is unclear, and discussed in more detail below.

7.2.2. Digestion Using Pressure-Swing Crystallization

Attempts to use pressure-swings to conduct purification via crystal digestion were unsuccessful. This result was unexpected and merits further investigation. This section provides a hypothesis for this failure, but experimental validation is not possible due to limited in-situ analytical capabilities.

Experimentally, nucleation and growth during pressure-swing digestion experiments occurred at elevated pressure. This is in contrast to the control cases, where nucleation occurred at ambient pressure. Due to the elevated pressure, different polymorphs could have been nucleated between the experiment and control case.⁷¹ Instead of digestion, the pressure-swing may have induced nucleation of the stable polymorph followed by solvent mediated phase transformation. This would have resulted in a similar product to the control case without digestion.

In order to test this theory, paracetamol crystals nucleated at both ambient and elevated pressure were analyzed using XRD. No difference between the two spectra was observed; suggesting that nucleation at elevated pressure produces the same polymorph as nucleation at ambient pressure. However, this result does not prove or disprove the previous theory. Because the filtration and collection process occurred at ambient pressure, crystals nucleated at elevated pressure were depressurized prior to collection, providing ample opportunity for solvent mediated phase transformation to the low

pressure polymorph. In order to test this theory properly, in-situ polymorph identification is required. This type of analytical capability is often practiced at small scale in diamond anvil experiments.^{73,101} However, this is not possible within the current experimental setup and would require significant modification.

7.2.3. Alternative Model Systems

The pressure-swing experiments presented here focus on small organic molecules in solution. This was primarily motivated by the project's focus on the purification of specialty chemicals. However, the pressure-swing technique has interesting possibilities for alternative model systems such as melts, polymers, or emulsions. In the first two cases, a rapid change in pressure would result in a rapid change in temperature as predicted in Chapter 5. This change in temperature could be used to alter crystallization behavior or materials properties. Previous work has shown that elevated pressure can be used to alter the crystallization behavior of polymers.¹⁰²⁻¹⁰⁴ Pressure-swings may be able to provide an additional dimension to this approach.

Emulsions provide an interesting model system for pressure-swing due to the multitude of potential variations in phase behavior as a function of pressure and temperature. For example, a solute may be more soluble in one phase at ambient pressure, but more soluble in another at elevated pressure. Pressure-swings may be used to drive a separation process in this way. Alternatively, pressure-swing could be used to induce the nucleation of a solute contained in droplets which are suspended in an emulsion. The use of droplets would radically alter the heat transfer within the system,

modifying the solubility behavior described in Chapter 5. While interesting, the exploration of these model systems is beyond the scope of this project.

7.3. Conclusions

This dissertation describes fundamental research in two areas of specialty chemicals purification: thermal gradient sublimation and crystallization. Sublimation experiments showed that the rate-limiting step for thermal gradient sublimation is vapor transport and deposition. A model describing this transport and deposition process was developed and compared to experiment. Agreement is good. This model was used to suggest guidelines for industrial scale-up and process design.

Crystallization experiments focused on the impact of rapid changes in pressure upon crystallization. The impact of these rapid changes in pressure on solubility was measured using a novel high pressure crystallizer. A simple thermodynamic model was developed to describe these changes, yielding insight for both traditional high pressure crystallization and the novel pressure-swing technique. Unfortunately, the decrease in solubility with pressure is often balanced by an increase in solubility caused by the temperature increase due to adiabatic compression. This yields a net change in solubility that is less than that expected from either process alone. Initial experiments using pressure-swing crystallization were only partially successful at replicating results obtained using traditional temperature control. A fundamental explanation for this failure is lacking, awaiting future research efforts.

8. References

- (1) Pollak, P. *Fine Chemicals: The Industry and the Business*; John Wiley & Sons, Inc.: Hoboken, NJ, 2007.
- (2) MarketLine. *Global Specialty Chemicals*; 2012.
- (3) Wang, C.; Dong, H.; Hu, W.; Liu, Y.; Zhu, D. *Chem. Rev.* **2012**, *112* (4), 2208–2267.
- (4) Dong, H.; Fu, X.; Liu, J.; Wang, Z.; Hu, W. *Adv. Mater.* **2013**, 1–25.
- (5) Sasabe, H.; Kido, J. *J. Mater. Chem. C* **2013**, *1* (9), 1699.
- (6) Tobjörk, D.; Österbacka, R. *Adv. Mater.* **2011**, *23* (17), 1935–1961.
- (7) Søndergaard, R. R.; Hösel, M.; Krebs, F. C. *J. Polym. Sci. Part B Polym. Phys.* **2013**, *51* (1), 16–34.
- (8) Mishra, A.; Bäuerle, P. *Angew. Chemie Int. Ed.* **2012**, *51* (9), 2020–2067.
- (9) Podzorov, V.; Sysoev, S. E.; Loginova, E.; Pudalov, V. M.; Gershenson, M. E. *Appl. Phys. Lett.* **2003**, *83* (17), 3504.
- (10) Lin, P.; Yan, F. *Adv. Mater.* **2012**, *24* (1), 34–51.
- (11) Pandey, R.; Holmes, R. J. *Adv. Mater.* **2010**, *22* (46), 5301–5305.
- (12) Lin, Y.; Li, Y.; Zhan, X. *Chem. Soc. Rev.* **2012**, *41* (11), 4245.
- (13) Erickson, N. C.; Holmes, R. J. *Appl. Phys. Lett.* **2010**, *97* (8), 083308.
- (14) Gather, M. C.; Köhnen, A.; Meerholz, K. *Adv. Mater.* **2011**, *23* (2), 233–248.
- (15) McGuire, J. L.; Hasskarl, H.; Bode, G.; Klingmann, I.; Zahn, M. In *Ullmann's Encyclopedia of Industrial Chemistry*; Wiley-VCH Verlag GmbH & Co. KGaA: Weinheim, Germany, 2007; pp 503–519.

- (16) Newman, D. J.; Cragg, G. M. *J. Nat. Prod.* **2012**, *75* (3), 311–335.
- (17) Tietze, M. L.; Leo, K.; Lüssem, B. *Org. Electron.* **2013**, *14* (9), 2348–2352.
- (18) Scholz, S.; Kondakov, D.; Lüssem, B.; Leo, K. *Chem. Rev.* **2015**, *115* (16), 8449–8503.
- (19) Pauli, G. F.; Chen, S.-N.; Simmler, C.; Lankin, D. C.; Gödecke, T.; Jaki, B. U.; Friesen, J. B.; McAlpine, J. B.; Napolitano, J. G. *J. Med. Chem.* **2014**, *57* (22), 9220–9231.
- (20) Cussler, E. L. *Diffusion: Mass Transfer in Fluid Systems*, 3rd ed.; Cambridge University Press, 2009.
- (21) Mullin, J. W. *Crystallization*, 4th ed.; Butterworth-Heinemann: Boston, 2001.
- (22) Morissette, S. *Adv. Drug Deliv. Rev.* **2004**, *56* (3), 275–300.
- (23) McGhie, A. R.; Garito, A. F.; Heeger, A. J. *J. Cryst. Growth* **1974**, *22* (4), 295–297.
- (24) Morgan, N. T.; Zhang, Y.; Molitor, E. J.; Bell, B. M.; Holmes, R. J.; Cussler, E. L. *AIChE J.* **2014**, *60* (4), 1347–1354.
- (25) Jeon, H.-G.; Inoue, M.; Hiramatsu, N.; Ichikawa, M.; Taniguchi, Y. *Org. Electron.* **2008**, *9* (5), 903–905.
- (26) Jeon, H.-G.; Kondo, Y.; Maki, S.; Matsumoto, E.; Taniguchi, Y.; Ichikawa, M. *Org. Electron.* **2010**, *11* (5), 794–800.
- (27) Morgan, N. T.; Zhang, Y.; Grandbois, M. L.; Bell, B. M.; Holmes, R. J.; Cussler, E. L. *Org. Electron. physics, Mater. Appl.* **2015**, *24*, 212–218.
- (28) Kuwabara, Y.; Ogawa, H.; Inada, H.; Noma, N.; Shirota, Y. *Adv. Mater.* **1994**, *6*

- (9), 677–679.
- (29) Davey, R. J.; Schroeder, S. L. M.; ter Horst, J. H. *Angew. Chem. Int. Ed. Engl.* **2013**, *52* (8), 2166–2179.
- (30) Mertz, J. *Introduction to Optical Microscopy*, 1st ed.; W. H. Freeman and Company, 2009.
- (31) Schneider, C. a; Rasband, W. S.; Eliceiri, K. W. *Nat. Methods* **2012**, *9* (7), 671–675.
- (32) Chen, S.; Guzei, I. A.; Yu, L. *J. Am. Chem. Soc.* **2005**, *127* (27), 9881–9885.
- (33) Ebbing, D. D. *General Chemistry*, 3rd ed.; Houghton Mifflin, 1990.
- (34) *ASTM E928-08(2014), Standard Test Method for Purity by Differential Scanning Calorimetry*; West Conshohocken, PA, 2014.
- (35) Meyer, V. R. *Practical High-Performance Liquid Chromatography*, 5th ed.; Wiley, 2010.
- (36) Bragg, W. H.; Bragg, W. L. *Proc. R. Soc. A Math. Phys. Eng. Sci.* **1913**, *88* (605), 428–438.
- (37) Barrett, M.; Hao, H.; Maher, A.; Hodnett, K.; Glennon, B.; Croker, D. *Org. Process Res. Dev.* **2011**, *15* (3), 681–687.
- (38) OECD. *OECD guidelines for the testing of chemicals 104: Vapor Pressure*; 2006.
- (39) Knudsen, M. *Kinetic Theory of Gases: Some Modern Aspects*, 3rd ed.; John Wiley & Sons, Inc.: New York, 1950.
- (40) Thejo Kalyani, N.; Dhoble, S. J. *Renew. Sustain. Energy Rev.* **2012**, *16* (5), 2696–2723.

- (41) Xiao, L.; Chen, Z.; Qu, B.; Luo, J.; Kong, S.; Gong, Q.; Kido, J. *Adv. Mater.* **2011**, *23* (8), 926–952.
- (42) Karl, N. *J. Cryst. Growth* **1990**, *99* (1-4), 1009–1016.
- (43) Kato, K.; Mori, T. *Mol. Cryst. Liq. Cryst.* **2007**, *471* (1), 53–60.
- (44) Karl, N. *Mol. Cryst. Liq. Cryst. Inc. Nonlinear Opt.* **1989**, *171* (1), 157–177.
- (45) Coropceanu, V.; Cornil, J.; da Silva Filho, D. A.; Olivier, Y.; Silbey, R.; Brédas, J.-L. *Chem. Rev.* **2007**, *107* (4), 926–952.
- (46) Jurchescu, O. D.; Baas, J.; Palstra, T. T. M. *Appl. Phys. Lett.* **2004**, *84* (16), 3061.
- (47) Warta, W.; Stehle, R.; Karl, N. *Appl. Phys. A Solids Surfaces* **1985**, *36* (3), 163–170.
- (48) Liu, S.-W.; Wen, J.-M.; Lee, C.-C.; Su, W.-C.; Wang, W.-L.; Chen, H.-C.; Lin, C.-F. *Thin Solid Films* **2013**, *534*, 640–644.
- (49) Roberson, L. B.; Kowalik, J.; Tolbert, L. M.; Kloc, C.; Zeis, R.; Chi, X.; Fleming, R.; Wilkins, C. *J. Am. Chem. Soc.* **2005**, *127* (9), 3069–3075.
- (50) Kloc, C.; Simpkins, P. G.; Siegrist, T.; Laudise, R. A. *J. Cryst. Growth* **1997**, *182* (3-4), 416–427.
- (51) Zeis, R.; Siegrist, T.; Kloc, C. *Appl. Phys. Lett.* **2005**, *86* (2), 022103.
- (52) Yamao, T.; Ota, S.; Miki, T.; Hotta, S.; Azumi, R. *Thin Solid Films* **2008**, *516* (9), 2527–2531.
- (53) Chaiken, R. F.; Sibbett, D. J.; Sutherland, J. E.; Van de Mark, D. K.; Wheeler, A. *J. Chem. Phys.* **1962**, *37* (10), 2311–2318.
- (54) Schultz, R. D.; Dekker, A. O. *J. Phys. Chem.* **1956**, *60*, 1095–1100.

- (55) Langmuir, I. *Phys. Rev.* **1918**, *12*, 368–370.
- (56) Readey, D. W.; Kuczynski, G. C. *J. Am. Ceram. Soc.* **1966**, *49* (1), 26–29.
- (57) Atkins, P.; de Paula, J. *Physical Chemistry*, 7th ed.; W. H. Freeman and Company: New York, 2003.
- (58) Monchick, L.; Mason, E. A. *J. Chem. Phys.* **1961**, *35* (5), 1676.
- (59) Monchick, L.; Yun, K. S.; Mason, E. A. *J. Chem. Phys.* **1963**, *39* (3), 654.
- (60) Narasimha, R. *J. Fluid Mech.* **1962**, *12* (02), 294.
- (61) Bird, R. B.; Stewart, W. E.; Lightfoot, E. N. *Transport Phenomena*, 2nd ed.; John Wiley & Sons, Inc., 2001.
- (62) Prud'Homme, R. K.; Chapman, T. W.; Bowen, J. R. *Appl. Sci. Res.* **1986**, *43* (1), 67–74.
- (63) Edwards, R. H. In *Rarefied Gas Dynamics*; Potter, J. L., Ed.; American Institute of Aeronautics and Astronautics: New York, 1977; pp 199–223.
- (64) Arkilic, E. B.; Schmidt, M. A.; Breuer, K. S. *J. Microelectromechanical Syst.* **1997**, *6*, 167–178.
- (65) Cunningham, R. E.; Williams, R. J. J. *Diffusion in Gases and Porous Media*; Plenum Press: New York, 1980.
- (66) Connolly, M. L. *J. Am. Chem. Soc.* **1985**, *107* (5), 1118–1124.
- (67) Connolly, M. L. *J. Mol. Graph.* **1993**, *11* (2), 139–141.
- (68) Taylor, G. *Proc. R. Soc. A Math. Phys. Eng. Sci.* **1953**, *219* (1137), 186–203.
- (69) Aris, R. *Proc. R. Soc. A Math. Phys. Eng. Sci.* **1956**, *235* (1200), 67–77.
- (70) *Handbook of Industrial Crystallization*, 2nd ed.; Myerson, A. S., Ed.; Butterworth-

Heinemann: Boston, 2002.

- (71) Fabbiani, F. P. A.; Pulham, C. R. *Chem. Soc. Rev.* **2006**, 35 (10), 932–942.
- (72) Neumann, M. a.; van de Streek, J.; Fabbiani, F. P. a.; Hidber, P.; Grassmann, O. *Nat. Commun.* **2015**, 6 (May), 7793.
- (73) Fabbiani, F. P. A.; Allan, D. R.; Parsons, S.; Pulham, C. R. *CrystEngComm* **2005**, 7 (29), 179.
- (74) Nowell, H.; Price, S. L. *Acta Crystallogr. Sect. B Struct. Sci.* **2005**, 61 (5), 558–568.
- (75) Fabbiani, F. P. A.; Allan, D. R.; Dawson, A.; David, W. I. F.; McGregor, P. A.; Oswald, I. D. H.; Parsons, S.; Pulham, C. R. *Chem. Commun.* **2003**, No. 24, 3004.
- (76) Oswald, I. D. H.; Pulham, C. R. *CrystEngComm* **2008**, 10 (9), 1114.
- (77) Joule, J. P. *Philos. Trans. R. Soc. London* **1859**, 149 (January), 133–136.
- (78) Boehler, R.; Kennedy, G. C. *J. Appl. Phys.* **1977**, 48 (10), 4183.
- (79) Rastogi, N. K.; Raghavarao, K. S. M. S.; Balasubramaniam, V. M.; Niranjana, K.; Knorr, D. *Crit. Rev. Food Sci. Nutr.* **2007**, 47 (1), 69–112.
- (80) Garriga, M.; Aymerich, T. *Safety of Meat and Processed Meat*; Toldrá, F., Ed.; Springer New York: New York, NY, 2009.
- (81) Incropera, F. P.; Dewitt, D. P.; Bergman, T. L.; Lavine, A. S. *Fundamentals of Heat and Mass Transfer*, 6th ed.; John Wiley & Sons: Hoboken, NJ, 2007.
- (82) Miletich, R.; Allan, D. R.; Kuhs, W. F. *Rev. Mineral. Geochemistry* **2000**, 41 (1), 445–519.
- (83) *Perry's chemical engineers' handbook*, 8th ed.; Green, D. W., Ed.; McGraw-Hill

Book Company: New York, 2008.

- (84) Granberg, R. A.; Rasmuson, Å. C. *J. Chem. Eng. Data* **1999**, *44* (6), 1391–1395.
- (85) Maher, A.; Croker, D.; Rasmuson, Å. C.; Hodnett, B. K. *J. Chem. Eng. Data* **2010**, *55*, 5314–5318.
- (86) Hildebrand, J. H.; Scott, R. L. *The Solubility of Nonelectrolytes*, 3rd ed.; Reinhold Publishing Corporation: New York, 1950.
- (87) Pytkowicz, R. M.; Connors, D. N. *Science* (80-.). **1964**, *144* (3620), 840–841.
- (88) Fessi, H.; Marty, J. P.; Puisieux, F.; Carstensen, J. T. *J. Pharm. Sci.* **1982**, *71* (7), 749–752.
- (89) Horstman, E. M.; Goyal, S.; Pawate, A.; Lee, G.; Zhang, G. G. Z.; Gong, Y.; Kenis, P. J. A. *Cryst. Growth Des.* **2015**, *15* (3), 1201–1209.
- (90) Blagden, N.; de Matas, M.; Gavan, P. T.; York, P. *Adv. Drug Deliv. Rev.* **2007**, *59* (7), 617–630.
- (91) Pertsin, A. J.; Kitaigorodskii, A. I. *The atom-atom potential method : applications to organic molecular solids*; Springer-Verlag: Berlin, 1987.
- (92) Nývlt, J. *Cryst. Res. Technol.* **1995**, *30* (4), 443–449.
- (93) Sudha, C.; Srinivasan, K. *CrystEngComm* **2013**, *15* (10), 1914.
- (94) Harner, R. S.; Ressler, R. J.; Briggs, R. L.; Hitt, J. E.; Larsen, P. A.; Frank, T. C. *Org. Process Res. Dev.* **2009**, *13*, 114–124.
- (95) Kaldis, E. *J. Cryst. Growth* **1969**, *5*, 376–390.
- (96) Qian, G.; Morgan, N. T.; Holmes, R. J.; Cussler, E. L.; Blaylock, D. W.; Froese, R. D. J. *AIChE J.* **2016**, *62* (3), 861–867.

- (97) Margenau, H.; Kestner, N. R. *Theory of Intermolecular Forces*, 2nd ed.; Pergamon Press: Oxford, 1971.
- (98) Berman, A. S. *J. Appl. Phys.* **1953**, *24* (9), 1232.
- (99) Yuan, S. W.; Finkelstein, A. *Laminar pipe flow with injection and suction through a porous wall*; Princeton, N. J., 1955.
- (100) Yuan, S. W. *J. Appl. Phys.* **1956**, *27* (3), 267.
- (101) Takano, K. J.; Shino, K.; Izawa, A.; Miyahara, M.; Wakatsuki, M. *Jpn. J. Appl. Phys.* **1993**, *32* (Part 1, No. 3A), 1268–1274.
- (102) Hasch, B. M.; Meilchen, M. A.; Lee, S.-H.; McHugh, M. A. *J. Polym. Sci. Part B Polym. Phys.* **1992**, *30* (12), 1365–1373.
- (103) Hutchison, I. B.; Delori, A.; Wang, X.; Kamenev, K. V.; Urquhart, A. J.; Oswald, I. D. H. *CrystEngComm* **2015**, *17* (8), 1778–1782.
- (104) Xiong, Y.; Kiran, E. *Rev. Sci. Instrum.* **1998**, *69* (3), 1463.

9. Appendices

A. NPD Synthesis Details

Two different grades of NPD were synthesized for this project. The “high purity” grade was used for all sublimation experiments except where explicitly mentioned. The “low purity” grade was used to assess the applicability of thermal gradient sublimation to very impure feeds.

A.1. High Purity NPD Synthetic Protocol

To a 2-L cylindrical jacketed glass reactor equipped with an overhead mechanical stirrer, heating/cooling bath, water condenser, and bottom drain was added tris(dibenzylideneacetone)dipalladium(0) (Sigma-Aldrich Lot 72896APV, 0.534 g, 0.58mmol), 2-dicyclohexylphosphino-2',4',6'-triisopropylbiphenyl (Sigma-Aldrich Lot H14U026, 1.252 g, 2.59 mmol), 4,4'-dibromobiphenyl (Sigma-Aldrich Lot MKBH5745V, 41.03 g, 131.5 mmol), *N*-phenyl-1-naphthylamine (Sigma-Aldrich Lot MKBV1722V, 60.53 g, 276 mmol), and sodium *tert*-butoxide (Sigma-Aldrich Lot SHBB0144V, 37.8 g, 393.4 mmol). The headspace was flushed with nitrogen. Toluene (Fisher HPLC grade Lot 117121, 820 mL) was sparged with nitrogen for 30 minutes and added to the reactor and the agitation was started at 300 rpm. The reaction mixture was heated to 80-95 °C (target of 95 °C) for 5.5 hours. The heating was turned off and the mixture was cooled to room temperature overnight as stirred. The mixture was filtered through a coarse glass sintered filter funnel. The reactor was rinsed with methanol (320.5 g) and this was used to reslurry and wash the filter cake. Additional methanol (323.5 g) was used to chromatographically wash the filter cake. The cake was partially dried on the

filter to yield 129.6 g of wet cake which was placed in the glass drying dish and dried under vacuum (80 °C and 10 mmHg) for 4 hours to yield 70.09 g (90.6% yield) of yellow powder that was identified as NPD; ¹H NMR; 400MHz, CDCl₃: δ = 7.94 (*d*, J = 8.0, 2H), 7.88 (*d*, J = 8.0, 2H), 7.76 (*d*, J = 8.0, 2H), 7.45 (*m*, 4H), 7.35 (*m*, 8H), 7.21 (*dd*, J = 8.0, 8.0, 4H), 7.04 (*m*, 8H), 6.93 (*dd*, J = 8.0, 8.0, 2H). Subsequent syntheses prepared 69.08 g (89.3% yield) and 69.10 g (89.3% yield) of NPD, respectively. These batches were combined to give 206 g of NPD that was analyzed by HPLC to be 99.2% pure.

A.2. Low Purity NPD Synthetic Protocol

To a 3-neck 1 L round bottom flask equipped with an overhead mechanical stirrer, heating mantle, thermoprobe, condenser, and nitrogen bubbler was added [1,1'-bis(diphenylphosphino)ferrocene]dichloropalladium(II) (Sigma-Aldrich Lot SHBB5758V, 1.08 g, 1.48 mmol), 4,4'-dibromobiphenyl (Sigma-Aldrich Lot MKBH5745V, 20.01 g, 64.1 mmol), *N*-phenyl-naphthylamine (Sigma-Aldrich Lot MKBH1722V, 29.54 g, 134.7 mmol), and sodium *tert*-butoxide (Sigma-Aldrich Lot 14396BPV, 18.92 g, 196.9 mmol). The flask was inerted with nitrogen. Toluene (Fisher HPLC grade lot 111565, 400 mL) was degassed by passing a stream of nitrogen through it for 5 minutes and then added to the reaction. The reaction was heated to 95 °C for 4 hours. In-process reaction samples (100 mL diluted with 5 mL THF and 1 mL injection) were analyzed at 4 hours. The reaction mixture was cooled to 25 °C and THF (100 mL) was added. The reaction mixture was passed through a bed of silica gel (139 g, 60 Å, 70-230 mesh) and the silica gel was eluted with toluene:THF (4:1, 500 mL). The effluent was combined and evaporated with a rotovap and the residue placed in a drying dish and

dried in a vacuum oven (80 °C and 10 mmHg) for 4 hours yielding 37 g of product that was identified as 77.5% NPD by HPLC.

B. Control Software for Pressure Crystallization System

The LabVIEW program used to control the pressure crystallization system consists of three main components, pressure control, pressure data acquisition, and temperature data acquisition. Pressure control and data acquisition is accomplished using a Teledyne ISCO D-Series Pump Controller attached to a PC using a serial-to-USB converter. Temperature data acquisition is accomplished using an Omega TC-08 8 channel thermocouple USB data acquisition module. The LabVIEW program has a graphical interface that provides realtime readings of temperature and pressure, along with control options for modifying the pressure or automatically applying varying pressure cycles. A screenshot of this interface is shown in Figure B.1.

This program was written in house using the LabVIEW software package except for the communication drivers for the controllers, which were written by Teledyne ISCO

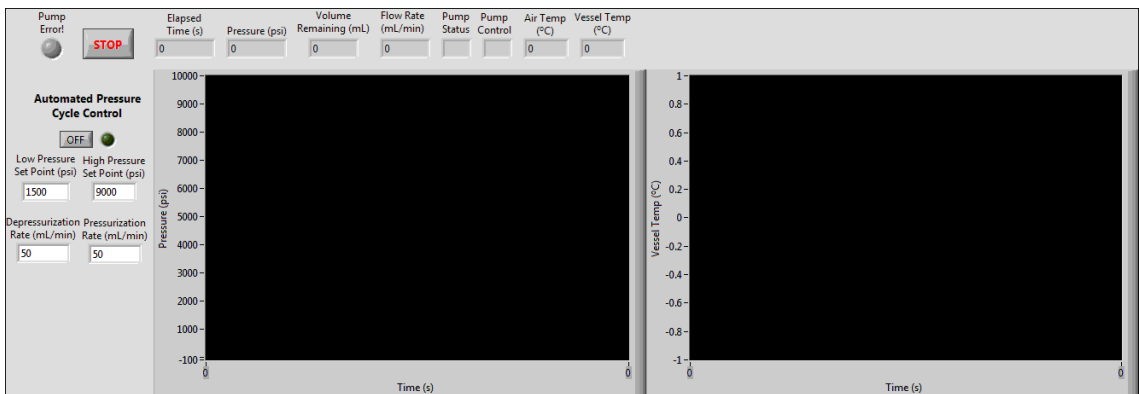


Figure B.1: Graphical interface for control of the pressure crystallization system.

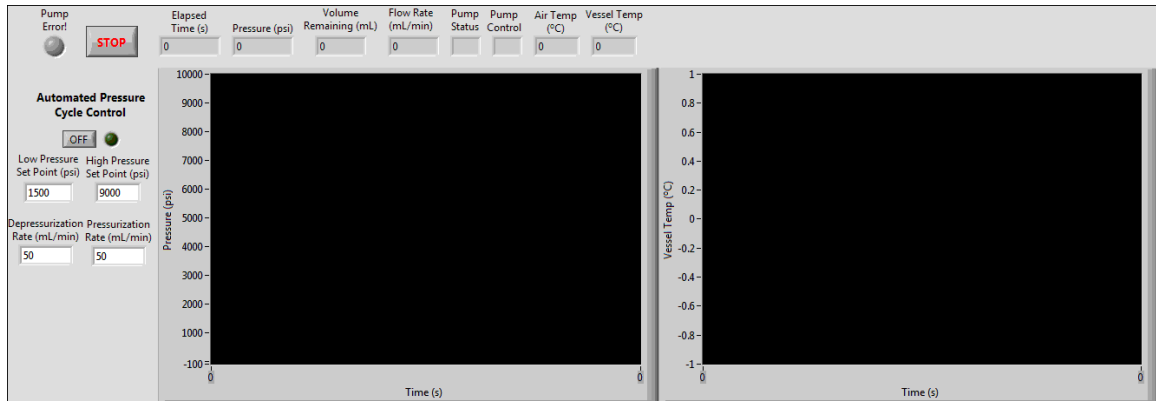
and Omega, respectively. A printout of this code is included below.

PPProgram2.0.vi

Connector Pane



Front Panel



Controls and Indicators



Low Pressure Set Point (psi)



High Pressure Set Point (psi)



Depressurization Rate (mL/min)



Pressurization Rate (mL/min)



Waveform Chart



Pressure (psi)



Elapsed Time (s)



Volume Remaining (mL)




Flow Rate (mL/min)



Pump Status

 **Pump Control**

 **Pump Error!**

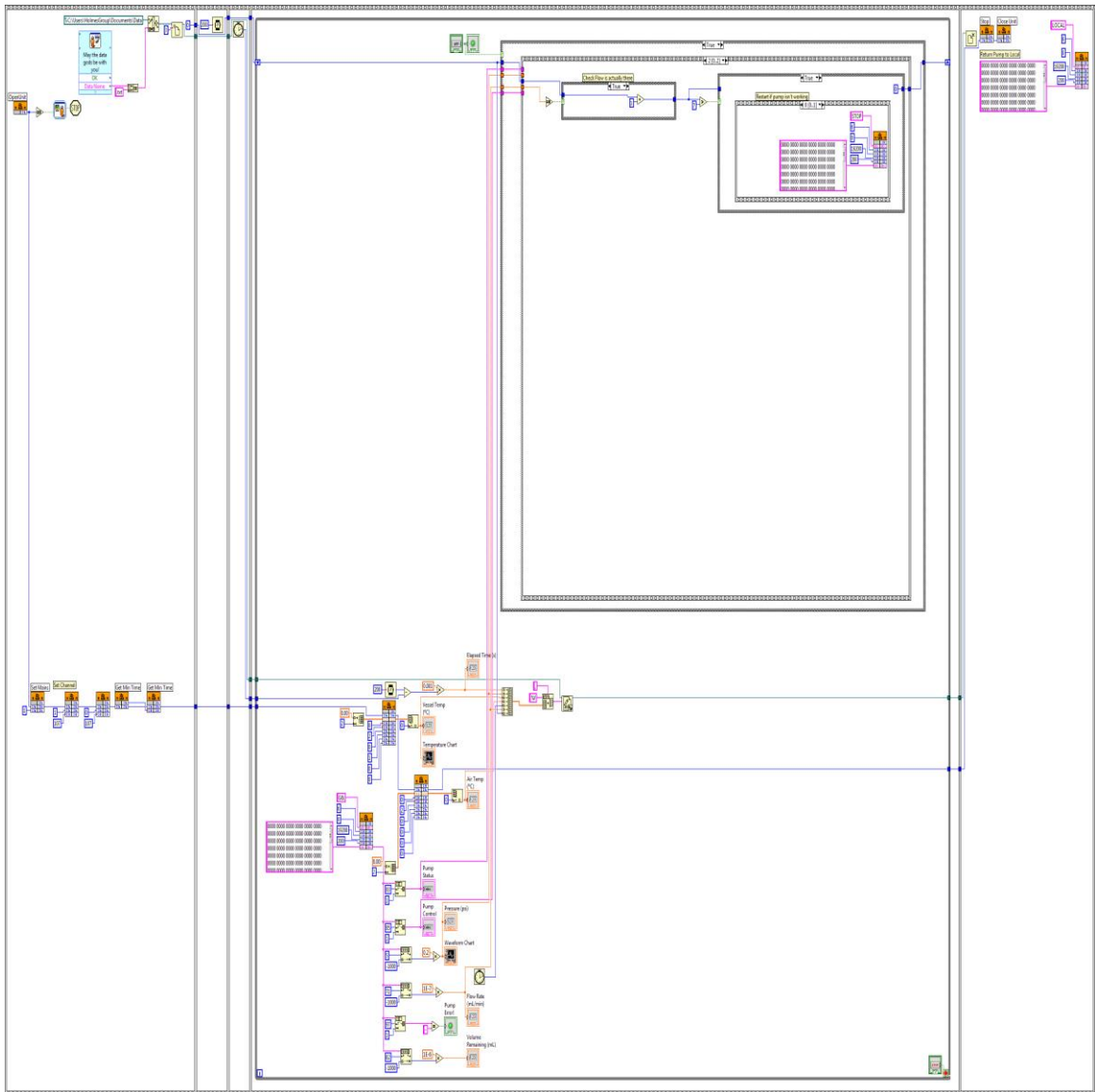


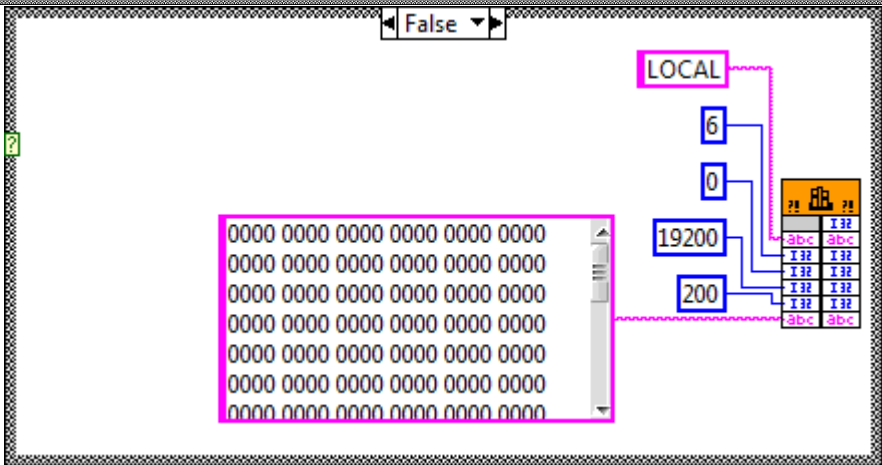
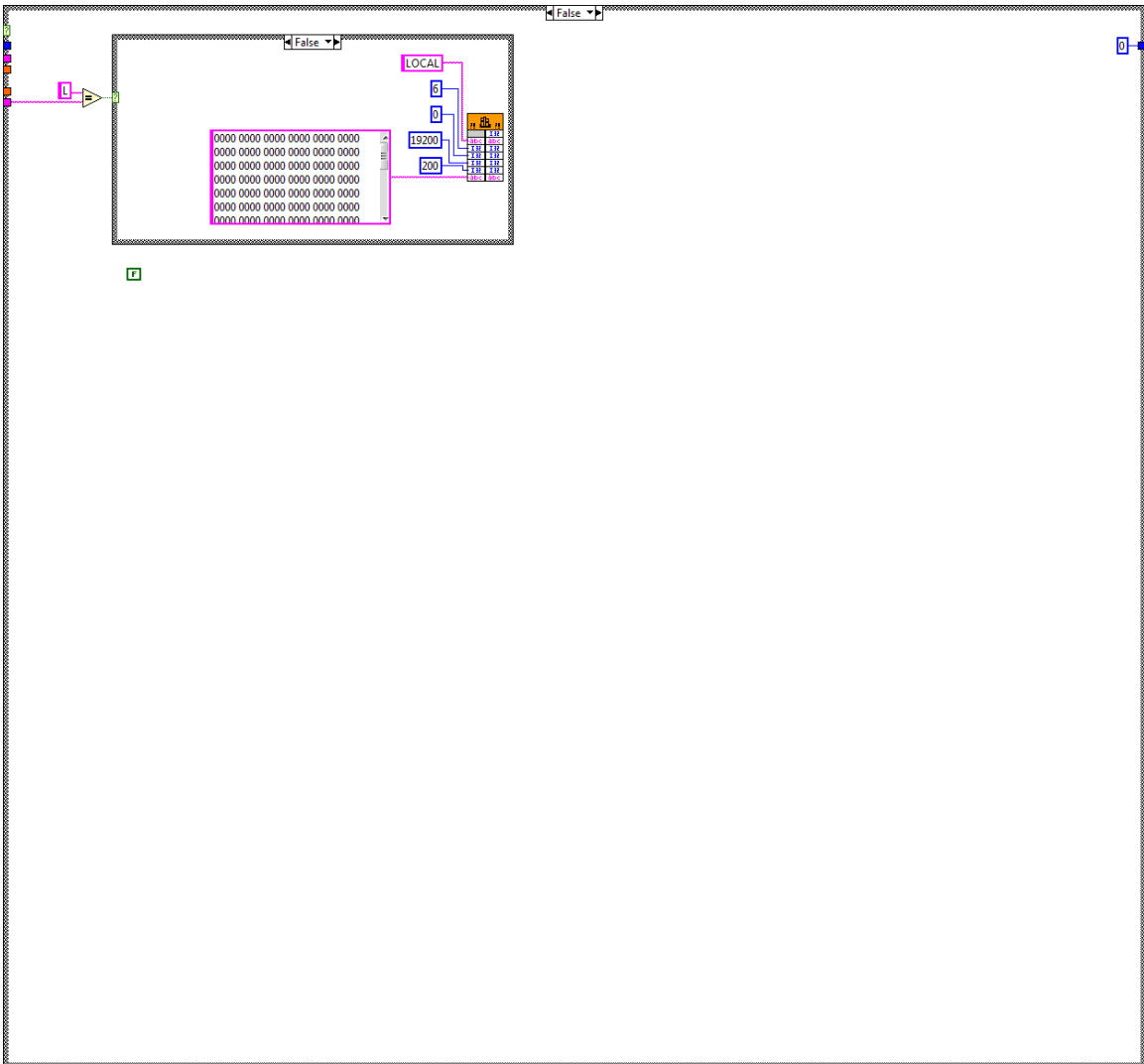
 **Temperature Chart**

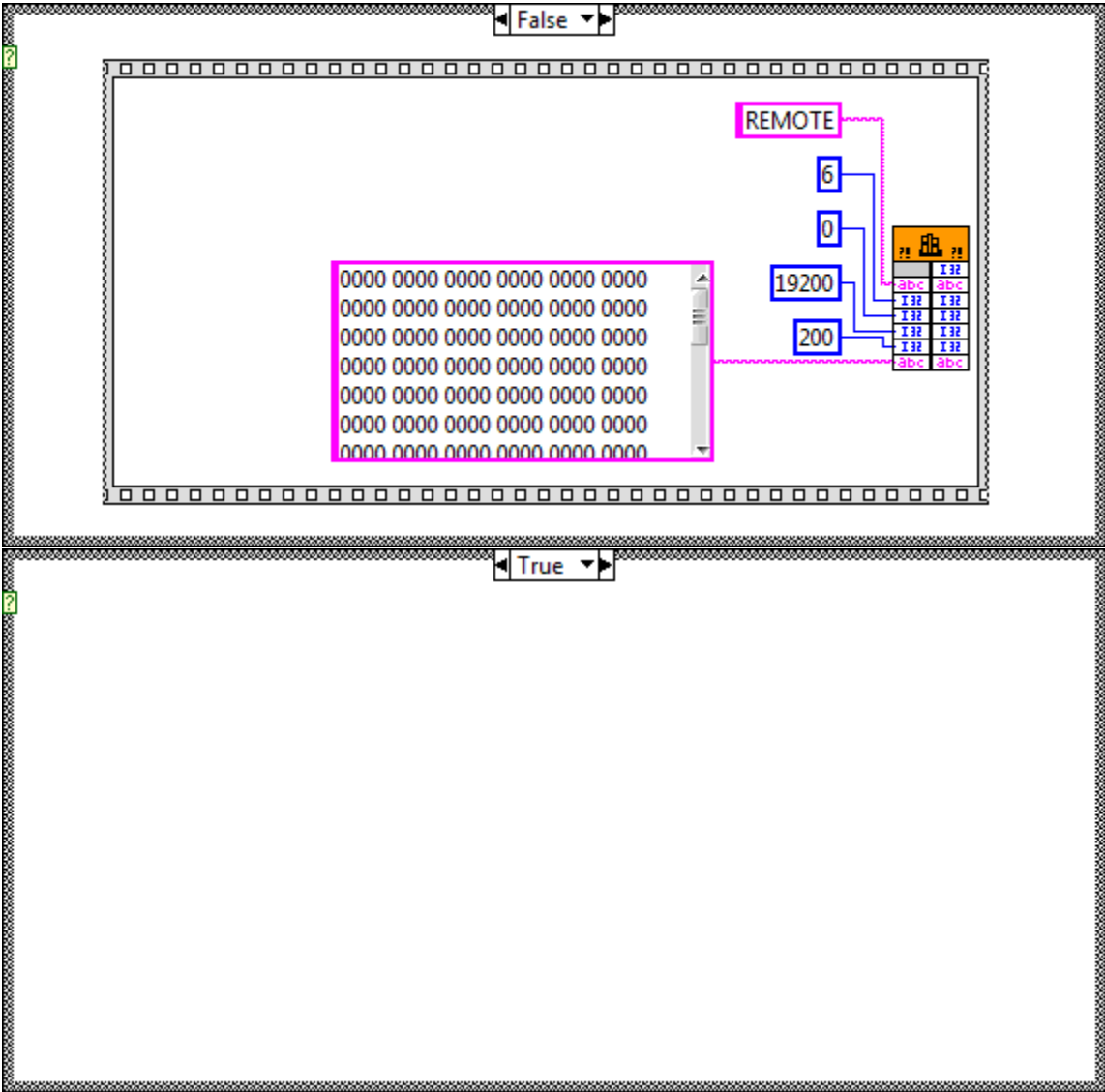
 **Air Temp (°C)**

 **Vessel Temp (°C)**

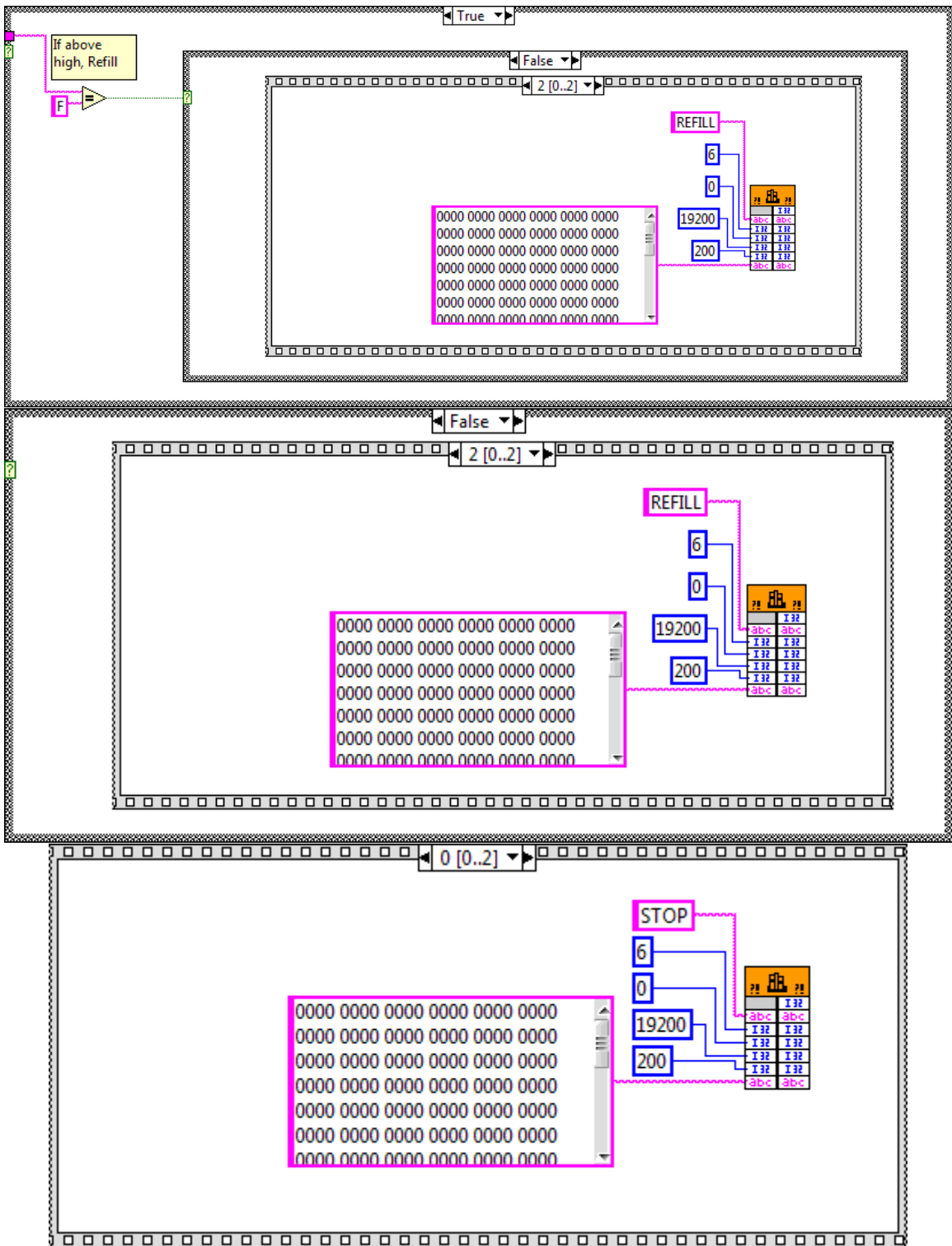
Block Diagram

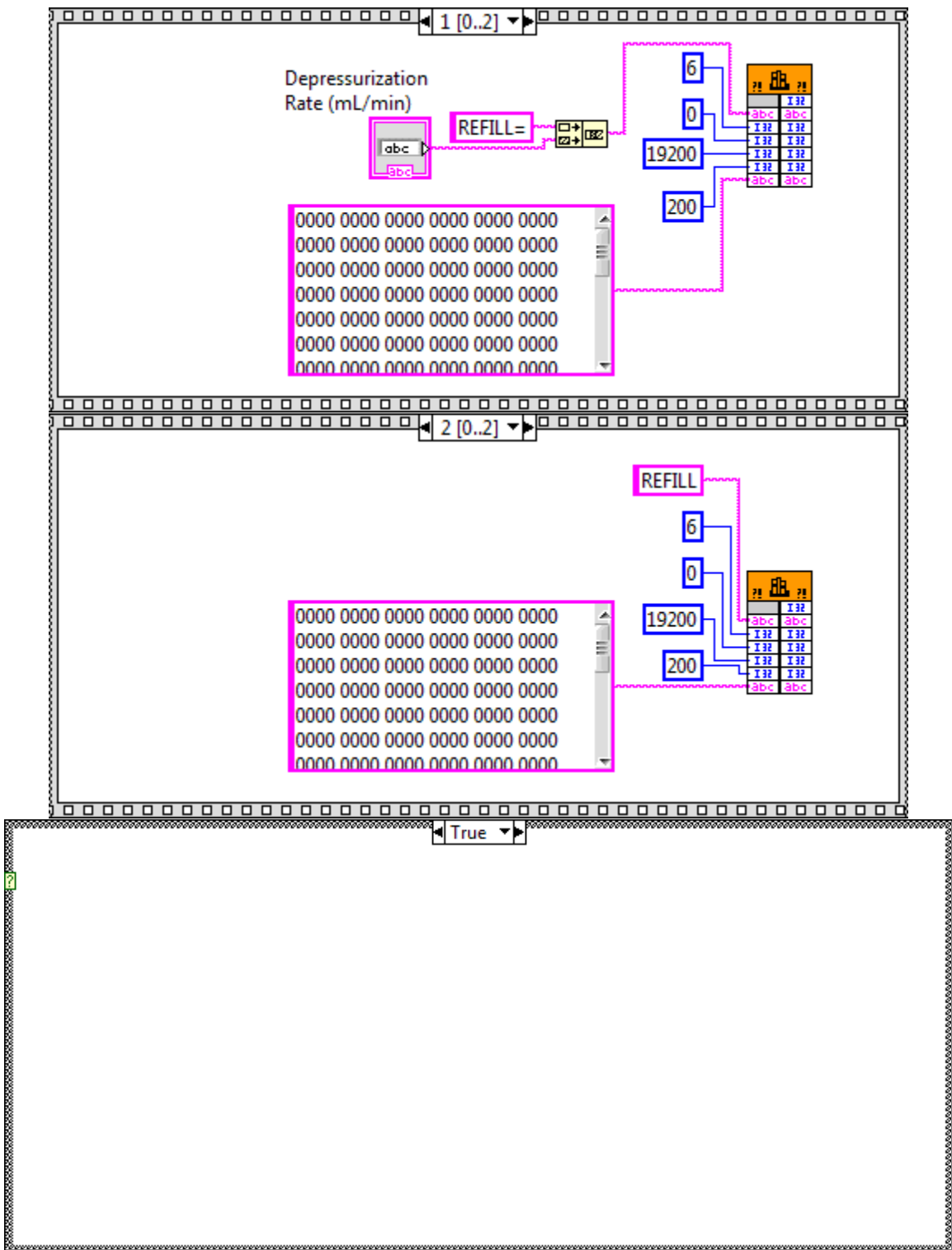


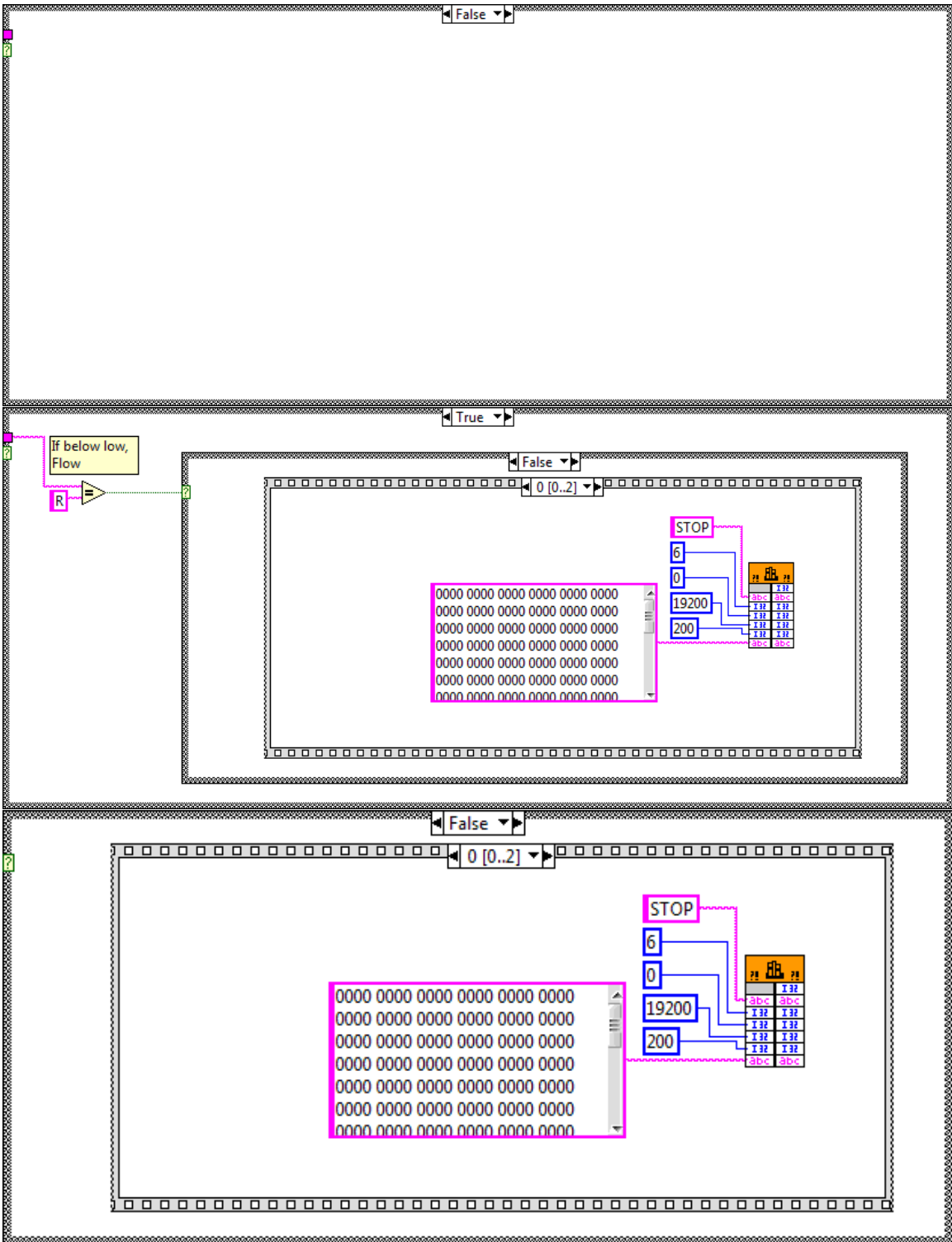


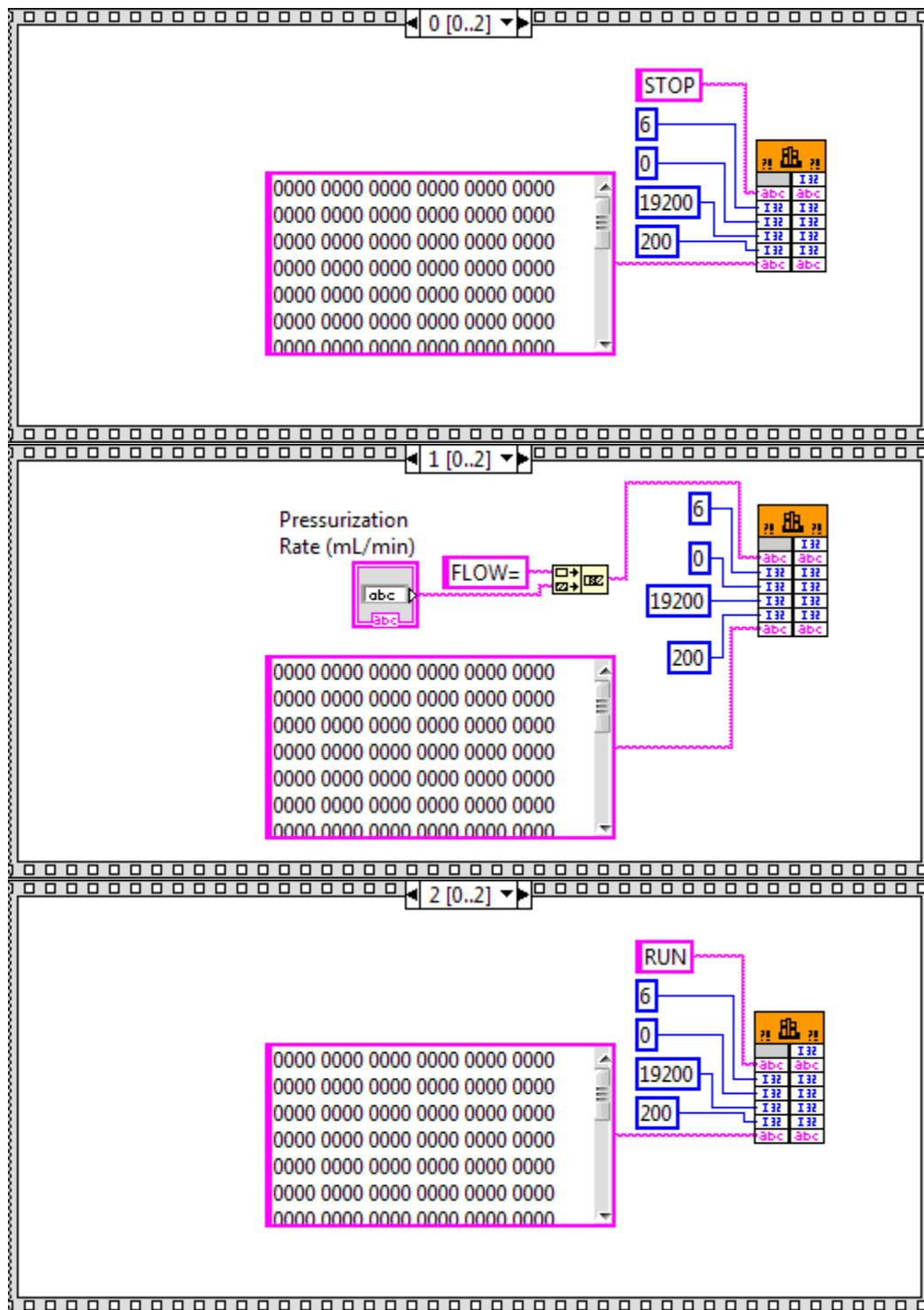


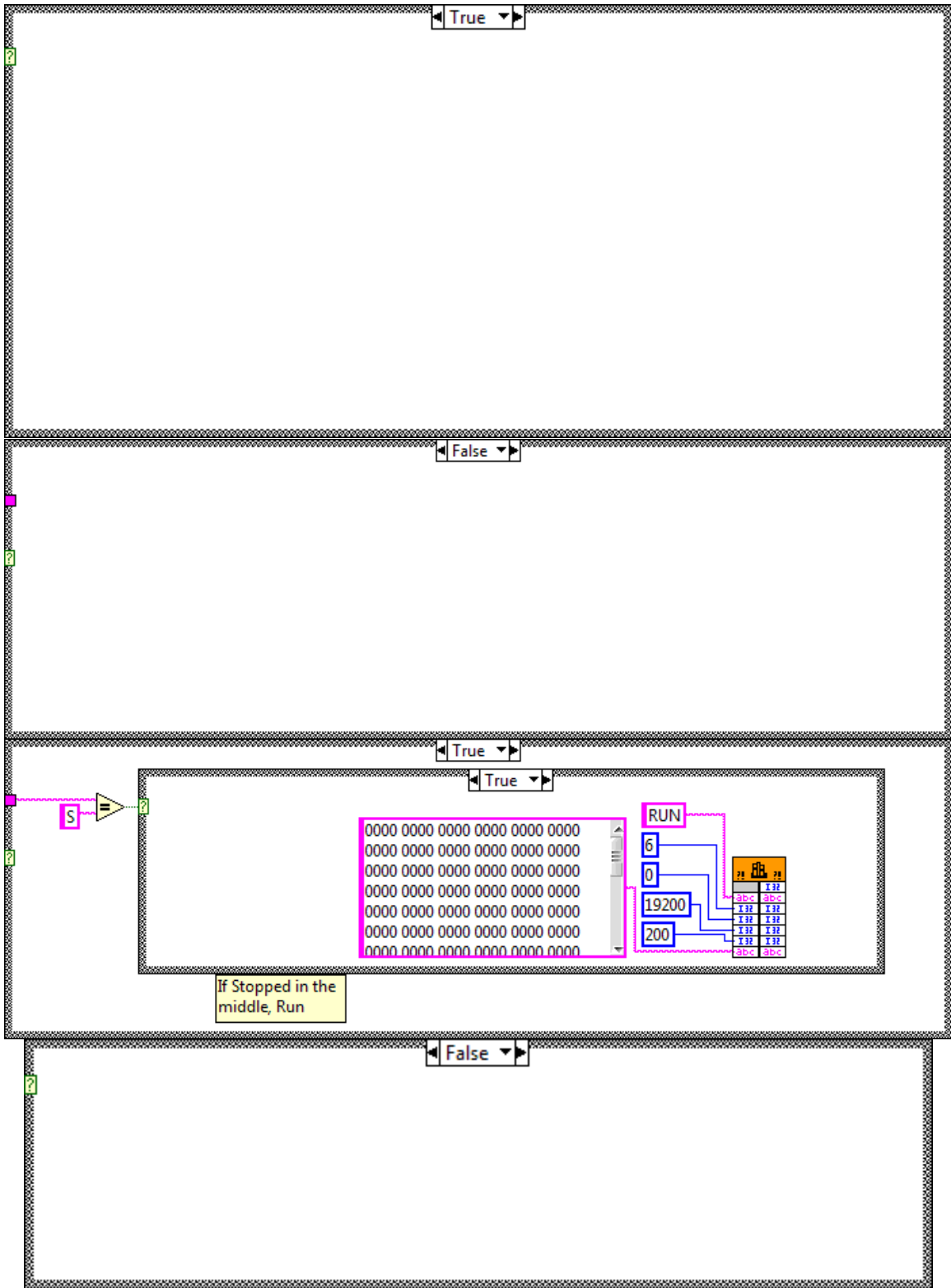


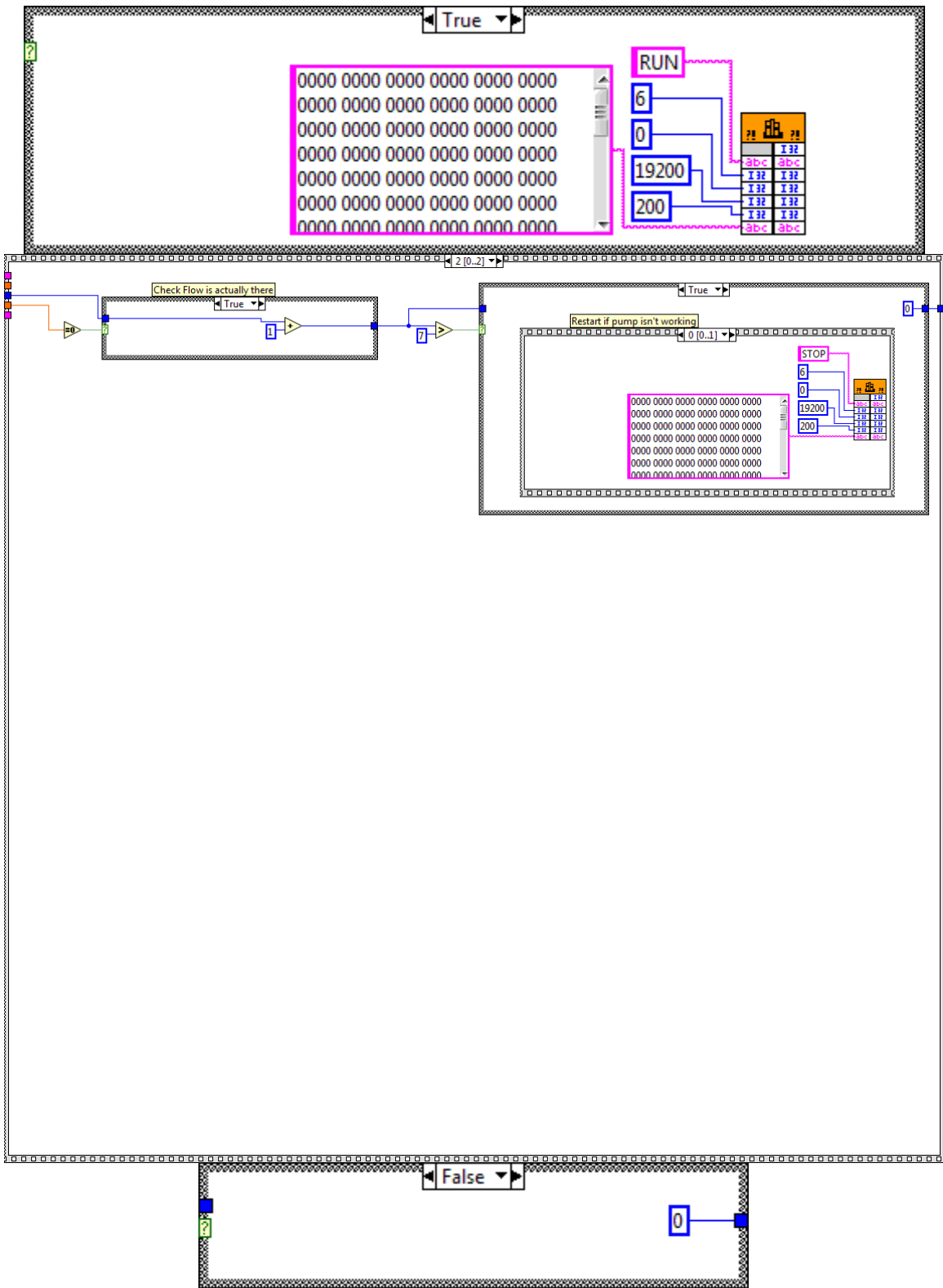


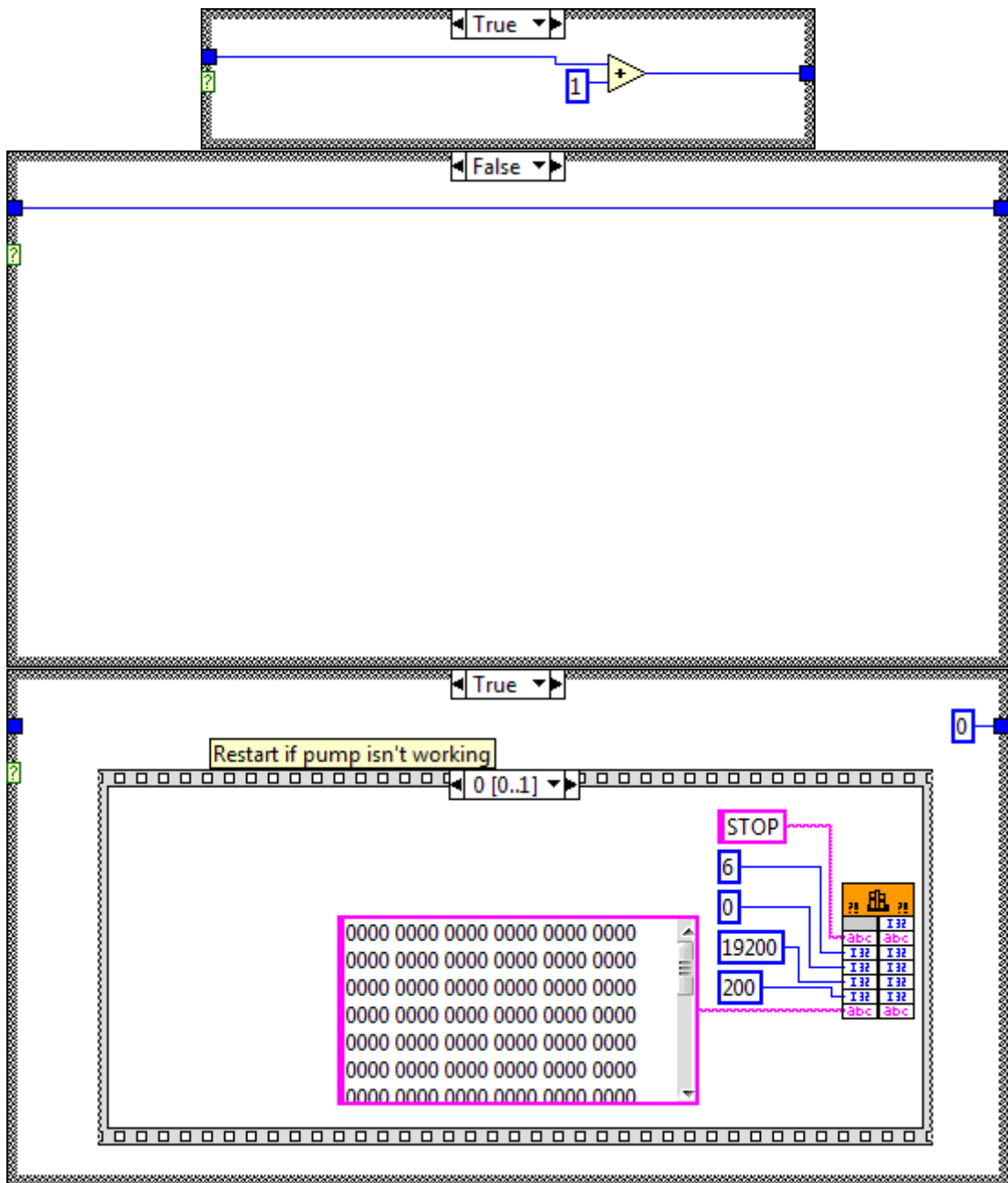


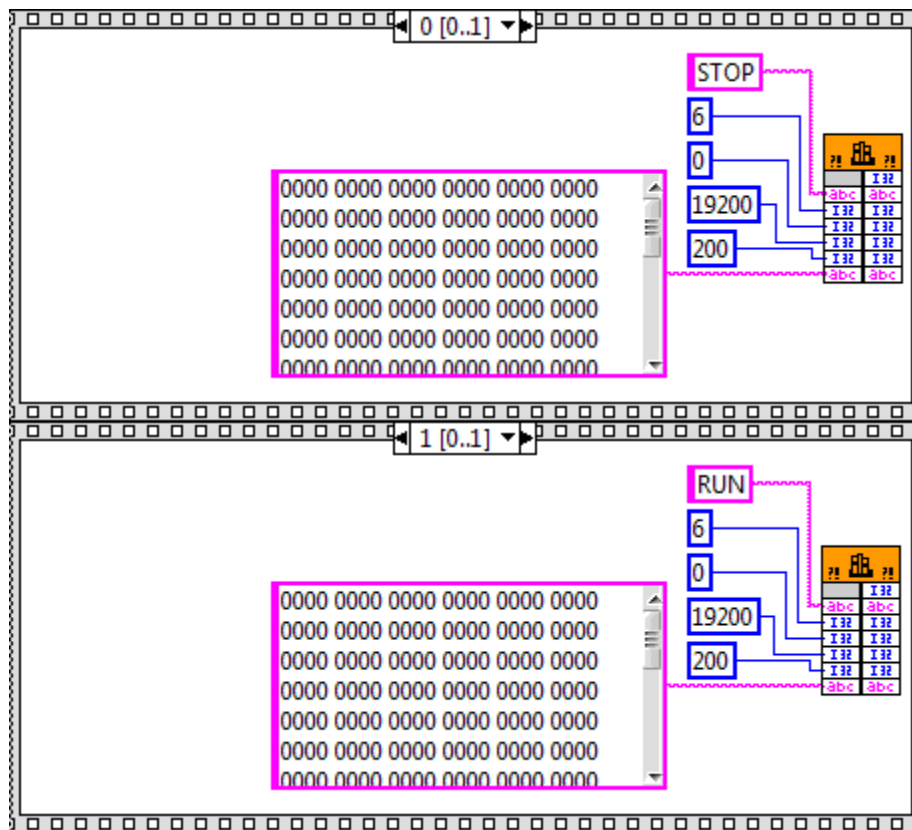












List of SubVIs and Express VIs with Configuration Information



Display Message to User

Display Message to User

Displays a standard dialog box that contains an alert or a message for users.

This Express VI is configured as follows:

Message: The unit failed to open correctly, disconnect the USB cable, reconnected the USB cable and attempt to run the program again



May the data gods be with you!

Prompt User for Input

Displays a standard dialog box that prompts users to enter information, such as a user name and password.

This Express VI is configured as follows:

Message to Display to the User:What would you like to name your data?

The inputs are:

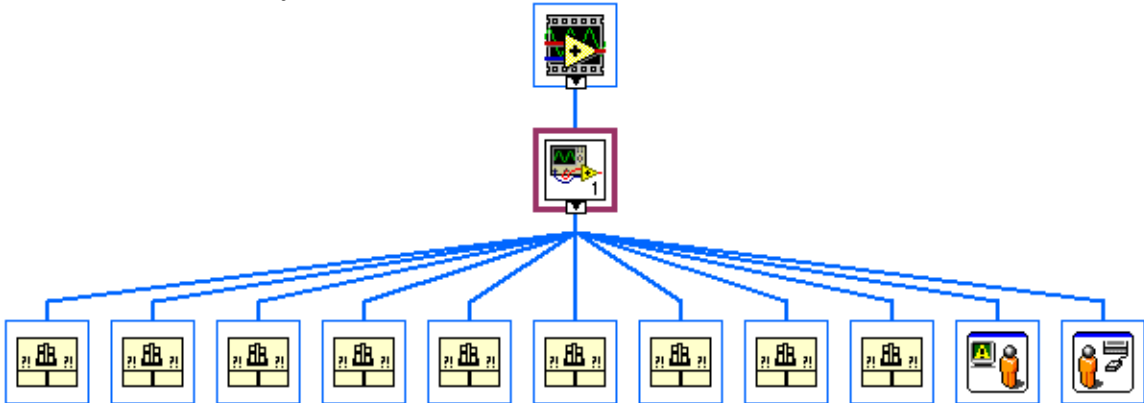
Text Entry Box: Data Name

VI Revision History

"PProgram2.0.vi History"

Current Revision: 117

Position in Hierarchy



Iconified Cluster Constants

C. Mass Spectrometry Data for NPD Impurities

Chemical analysis to determine sample purity was conducted by The Dow Chemical Company. The specific analytical protocol used to determine the structure of the major impurities within NPD is described below.

C.1. Analytical Procedure

NPD samples were prepared as 2 mg/mL solutions in tetrahydrofuran. Three microliter aliquots of solutions were injected onto an Agilent 1200SL binary gradient liquid chromatograph coupled to an Agilent 6520 QToF, quadrupole-time of flight mass spectroscopy (MS) system via a dual spray electrospray (ES) interface operating in the positive ion (PI) mode. The liquid chromatography (LC) conditions included: column, Zorbax SB-C8, 3.5 μ m, 4.6x150mm. Mobile phase: water/0.1 v% formic acid (88%): THF. Gradient programming: 0 min, 55%B; 15min, 75%B; 20min, 75%B. Flow rate: 1.0mL/min. Oven temperature: 40°C. Detection wavelength: 210 to 600nm summed. The ES source conditions included: Gas Temp- 365°C, Gas Flow – 11ml/min, Capillary- 3.5 kV, Nebulizer – 45PSI, Fragmentor -145V. The time of flight (TOF) mass spectrometer was scanned from 50 to 1700 amu at a rate of 3 scans per second and alternating between the MS and MS/MS modes. Collision gas of nitrogen and collisions energies of 65V were employed in the MS/MS modes. Purity of the materials was determined by area percent assay of the summed UV response from 210 to 600 nm.

C.2. Mass Spectroscopy Data for Molecular Structures in Figure 4.5

A) (M+H)⁺ : 589.2651(C₄₄H₃₃N₂); MS/MS – 217.0874 (C₁₆H₁₁N), 369.1496 (C₂₈H₁₉N),
293.1187 (C₂₂H₁₅N), 461.2003 (C₃₄H₂₅N₂), 511.2160 (C₃₈H₂₇N₂)

- B) (M+H)⁺ : 806.3531(C₆₀H₄₄N₃); MS/MS – 218.0948 (C₁₆H₁₂N), 345.1491 (C₂₆H₁₉N),
714.2987 (C₅₄H₃₈N₂), 461.1984 (C₃₄H₂₅N₂), 588.2525 (C₄₄H₃₂N₂), 166.0634 (C₁₂H₈N)
- C) (M+H)⁺ : 958.4142 (C₇₂H₅₂N₃); MS/MS – 218.0962 (C₁₆H₁₂N), 497.2126 (C₃₈H₂₇N),
866.3621 (C₆₆H₄₆N₂), 740.3158 (C₅₆H₄₀N₂), 333.1375 (C₂₄H₁₇N₂)

D. Transport Velocity Simulation Code

This Matlab program was written to simulate the transport velocity as a function of pressure, as shown in Figure 4.7. In Figure 4.7, the transport velocity is shown for TCTA under similar conditions to those used in our experiments: 3cm tube diameter, 0.45m tube length, and 1 nm collision diameter. However, this code was designed such that it can calculate the transport velocity as a function of any of these parameters, potentially useful for process design. Comparison of these curves does not yield any theoretical insight, as the general shape of the curve remains constant over realistic parameter values.

D.1. Matlab Code

```
clear

% Set Constants

MW = .74089;           % Molecular Weight (kg/mol)
NA = 6.022*10^23;     % Avagadro's Number (molecules/mol)
m = MW / NA;         % Mass per Molecule (kg)
kb = 1.3806*10^-23;   % Boltzmann's Cosntant (m^2*kg/s^2*K)
T = 310+273.15;      % Assume Constant Temperature (K)
L = .4572;           Tube Length (m)

% Set Diameter Iteration Parameters

k=6;
```

```
d=[3*10^-2 3*10^-2 3*10^-2 3*10^-2 3*10^-2 3*10^-2 ];           % Tube Diameter (m)
```

```
% Set Tube Length Iteration Parameters
```

```
L = [0.01 0.05 0.1 0.5 1 10];                                     % Tube Length (m)
```

```
% Set Collision Diameter Parameters
```

```
sig=[1.026*10^-9 1.026*10^-9 1.026*10^-9 1.026*10^-9 1.026*10^-9 1.026*10^-9 ];
```

```
% Collision Diameter (m)
```

```
% Set Pressure Iteration Parameters
```

```
Pmin = 0.0001;                                                   % Minimum Pressure (Pa)
```

```
Pmax = 1000;                                                     % Maximum Pressure (Pa)
```

```
n = 1000;                                                         % Number of iterations
```

```
i=2;
```

```
logPmin = log(Pmin);                                             % Space points equally on log scale
```

```
logPmax = log(Pmax);
```

```
logPstep = (logPmax - logPmin)/n;
```

```
logP(1,1)=logPmin;                                              % Intial Pressure (Pa)
```

```
P(1,1)=Pmin;
```

```
for i=2:n
```

```

logP(i,1)=logP(i-1,1)+logPstep;           % Calculate Pressure (Pa)

P(i,1)=exp(logP(i,1));

i=i+1;

end

j=1;

for j=1:k
    i=1;

    for i = 1:n
        mu(i,j) = (2/3)*(sqrt(m*kb*T))/(sig(j)^2*pi()^(3/2));
        % Viscosity ( kg / m*s)

        mfp(i,j) = kb*T/(sqrt(2)*pi()*sig(j)^2*P(i,1));
        % Mean Free Path (m)

        u(i,j) = sqrt(8*kb*T/(pi()*m));
        % Kinetic Velocity (m/s)

        jf(i,j)= P(i,1)*d(j)^2/(32*mu(i,j)*L(j));
        % Normalized Flow Flux (m/s)

        jd(i,j)= (u(i,j)/3)*(1/(L(j)/mfp(i,j) +L(j)/d(j)));
        % Normalized Diffusive Flux (m/s)

        J(i,j)= jf(i,j) + jd(i,j);
    end
end

```

```
% Total Normalized Flux (m/s)
```

```
i = i+1;
```

```
% Iterate
```

```
end
```

```
ParameterList=['d=' num2str(d(j)) ' m, sigma=' num2str(sig(j)) ' m, L='  
num2str(L(j)) ' m'];
```

```
comlist(j)={ParameterList};
```

```
j=j+1;
```

```
end
```

```
loglog(P,J)
```

```
xlabel('Pressure (Pa)');
```

```
ylabel('Reduced Flux (m/s)');
```

```
filename='JvsP.txt';
```

```
Names(1)={'Pressure'};
```

```
Units(1)={'Pa'};
```

```
Com(1)={'X'};
```

```
data(:,1)=P(:,1);
```

```
i=2;
```

```
n=k+1;
```

```

for i=2:n

    data(:,i)=J(:,i-1);

    Names(i)={'Reduced Flux'};

    Units(i)={'m/s'};

    Com(i)=comlist(i-1);

    i=i+1;

end

hdr=sprintf('%s\t',Names{:});
hdr(end)='';

unit=sprintf('%s\t',Units{:});
unit(end)='';

comments=sprintf('%s\t',Com{:});
comments(end)='';

dlmwrite(filename,hdr,'');

dlmwrite(filename,unit,'-append','delimiter','');

dlmwrite(filename,comments,'-append','delimiter','');

dlmwrite(filename,data,'-append','delimiter','\t');

```

E. List of Publications

1. Morgan NT, Zhang Y, Molitor EJ, Bell BM, Holmes RJ, Cussler EL. Understanding Rate-Limiting Processes for the Sublimation of Small Molecule Organic Semiconductors. *AICHE J.* 2014. DOI: 10.1002/aic.14357
2. Morgan NT, Zhang Y, Grandbois ML, Bell BM, Holmes RJ, Cussler EL. Mechanism for the Separation of Organic Semiconductors via Thermal Gradient Sublimation. *Org Electron.* 2015. DOI: 10.1016/j.orgel.2015.05.029
3. Qian G, Morgan NT, Blaylock DW, Froese RD, Holmes RJ, Cussler EL. Sublimation as a Function of Diffusion. *AICHE J.* 2015. DOI: 10.1002/aic.15119
4. Morgan NT, Frank TC, Holmes RJ, Cussler EL. The Effect of Rapid Pressurization on the Solubility of Small Organic Molecules. *Cryst. Growth Des.* 2016. DOI: 10.1021/acs.cgd.5b01510

F. List of Presentations

1. Morgan NT, Zhang Y, Holmes RJ, Cussler EL. Sublimation Mechanism for Small Molecule Organic Semiconductors. IPRIME Annual Meeting. Minneapolis, MN. May 28-30, 2013.
2. Morgan NT, Zhang Y, Molitor EJ, Bell BM, Holmes RJ, Cussler EL. Understanding the Rate-Limiting Processes for the Purification of Small Molecule Organic Semiconductors. Materials Research Society Fall Meeting. Boston, MA. December 1-6, 2013.
3. Morgan NT, Zhang Y, Molitor EJ, Bell BM, Holmes RJ, Cussler EL. Understanding the Rate-limiting Processes for the Purification of Small Molecule Organic Semiconductors. IPRIME Annual Meeting. Minneapolis, MN. May 27-29, 2014.
4. Morgan NT, Zhang Y, Grandbois ML, Bell BM, Holmes RJ, Cussler EL. Using Mass Transport to Guide the Purification of Organic Semiconductors via Sublimation. American Physical Society March Meeting. San Antonio, TX. March 2-6, 2015.
5. Morgan NT, Zhang Y, Grandbois ML, Bell BM, Holmes RJ, Cussler EL. Understanding Mass Transport during the Purification of Organic Semiconductors via Sublimation. IPRIME Annual Meeting. Minneapolis, MN. May 26-28, 2015.
6. Morgan NT, Zhang Y, Grandbois ML, Bell BM, Holmes RJ, Cussler EL. Improving the Separation of Organic Small Molecules Purified via Sublimation. American Institute of Chemical Engineers Annual Meeting. Salt Lake City, UT. November 8-13, 2015.
7. Morgan NT, Frank TC, Holmes RJ, Cussler EL. Effect of Rapid Pressurization on the Solubility of Small Organic Molecules. American Chemical Society National Meeting. San Diego, CA. March 13-17, 2016.
8. Morgan NT, Qian G, Blaylock DW, Bell BM, Holmes RJ, Cussler EL. Alternative Purification Strategies for High Value Organic Molecules. IPRIME Annual Meeting. Minneapolis, MN. May 31-June 2, 2016.

G. List of Patents

1. Cussler EL, Grandbois ML, Holmes RJ, Morgan NT, Zhang Y. Method for Separation of a Molecular Species by Sublimation. U.S. Patent Application 62093045. December 17, 2014.

H. Copyright Permissions

Chapter 3: All or portions of Chapter 4 were reproduced or adapted with permission from “Morgan NT, Zhang Y, Molitor EJ, Bell BM, Holmes RJ, Cussler EL. Understanding Rate-Limiting Processes for the Sublimation of Small Molecule Organic Semiconductors. *AIChE J.* 2014. DOI: 10.1002/aic.14357.” Copyright 2014 John Wiley and Sons.

All or portions of Chapter 4 were reproduced or adapted with permission from “Morgan NT, Zhang Y, Grandbois ML, Bell BM, Holmes RJ, Cussler EL. Mechanism for the Separation of Organic Semiconductors via Thermal Gradient Sublimation. *Org Electron.* 2015. DOI: 10.1016/j.orgel.2015.05.029.” Copyright 2015 Elsevier.

Chapter 4: All or portions of Chapter 4 were reproduced or adapted with permission from “Morgan NT, Zhang Y, Molitor EJ, Bell BM, Holmes RJ, Cussler EL. Understanding Rate-Limiting Processes for the Sublimation of Small Molecule Organic Semiconductors. *AIChE J.* 2014. DOI: 10.1002/aic.14357.” Copyright 2014 John Wiley and Sons.

All or portions of Chapter 4 were reproduced or adapted with permission from “Morgan NT, Zhang Y, Grandbois ML, Bell BM, Holmes RJ, Cussler EL. Mechanism for the Separation of Organic Semiconductors via Thermal Gradient Sublimation. *Org Electron.* 2015. DOI: 10.1016/j.orgel.2015.05.029.” Copyright 2015 Elsevier.

Chapter 5: All or portions of Chapter 5 were reproduced or adapted with permission from “Morgan NT, Frank TC, Holmes RJ, Cussler EL. The Effect of Rapid Pressurization on the Solubility of Small Organic Molecules. *Cryst. Growth Des.* 2016. DOI: 10.1021/acs.cgd.5b01510.” Copyright 2016 American Chemical Society.

Chapter 7: All or portions of Chapter 7 were reproduced or adapted with permission from “Qian G, Morgan NT, Blaylock DW, Froese RD, Holmes RJ, Cussler EL. Sublimation as a Function of Diffusion. *AIChE J.* 2015. DOI: 10.1002/aic.15119.” Copyright 2015 John Wiley and Sons.